Fully compressible Direct Numerical Simulations of carbon dioxide close to the vapour-liquid critical point

Sengupta, Uttiya

DOI
10.4233/uuid:513e5fa7-aef5-47e8-a7f9-d99a06c8981d

Publication date
2019

Document Version
Final published version

Citation (APA)
Sengupta, U. (2019). *Fully compressible Direct Numerical Simulations of carbon dioxide close to the vapour-liquid critical point*. [Dissertation (TU Delft), Delft University of Technology].
https://doi.org/10.4233/uuid:513e5fa7-aef5-47e8-a7f9-d99a06c8981d

Fully Compressible Direct Numerical Simulations of carbon dioxide close to the vapour-liquid critical point

Dissertation

for the purpose of obtaining the degree of doctor
at Delft University of Technology,
by the authority of the Rector Magnificus prof. dr. ir. T.H.J.J. van der Hagen,
Chair of the Board of Doctorates,
to be defended publicly on
Monday 25 February 2019 at 3:00 clock
by

Uttiya SENGUPTA

Master of Engineering in Chemical Engineering, Indian Institute of Science, Bangalore, India
born in Calcutta, India

This dissertation has been approved by the promotors:

Prof. dr. ir. B. J. Boersma
Dr. R. Pecnik

Composition of the doctoral committee:

Rector Magnificus,	Chairperson
Prof. dr. ir. B.J. Boersma	Delft University of Technology, promotor
Dr. R. Pecnik	Delft University of Technology, promotor

Independent Members:

Prof. dr. S. Hickel	Delft University of Technology
Prof. dr. ir. R.W.C.P. Verstappen	University of Groningen
Prof. dr. A. Soldati	University of Udine, Italy
Prof. dr. ir. J. van Oijen	Eindhoven University of Technology
Prof.dr. D.J.E.M. Roekaerts	Delft University of Technology
Prof. dr. ir. C. Poelma	Delft University of Technology

This research is supported by a research grant given by Shell for the PhD program Computational Science in Energy Research in partnership with NWO.

ISBN

[1] Author e-mail address: sumeetsengupta@gmail.com

Dedicated

to

my mother Sanchayita,

my brother Uddipta,

and to all my friends who have made my stay here a joyous experience.

Contents

Summary

The challenge of global warming caused by the emission of greenhouse gases has led to the desire for mitigating climate change by exploring the use of alternative sources of energy to reduce the use of traditional fossil fuels. In this context, supercritical fluids play an important role due to their use in various technologies and processes that promote sustainable development. These fluids possess a unique combination of gas-like and liquid-like properties enabling their usage in supercritical power cycles, which are more efficient compared to other methods of energy conversion.

In this thesis, we investigate turbulent flows of supercritical CO_2 near the vapour-liquid critical point in a channel geometry by solving the fully compressible Navier Stokes equations. The purpose of the investigation is to gain a better understanding of the physics of turbulent supercritical fluid flows near the critical point by taking the compressibility effects into account.

In the last part of the thesis, the influence of bulk viscosity on shock structure for supercritical CO_2 flows near the critical point is investigated.

Our investigations reveal some fascinating conclusions. Significant levels of compressibility effects are seen to exist close to the walls only if the trans-critical transition is located very close to a wall. For all the other cases, significant compressibility effects are not observed. The traditional scaling analysis utilizing the van Driest and the extended van Driest scaling reveals that most of the changes in velocity fluctuations, kinetic energy and mean velocity profile can be explained by the changes in mean density and mean viscosity. The nature of the density fluctuations is also influenced by the location of the critical temperature near the cold wall or near the center of the channel. The turbulent heat flux profiles also reveal a strong influence of the location of the point of trans-critical transition. A quadrant analysis of the turbulent heat fluxes near the cold and hot walls reveals that mixing near the cold and hot walls occurs mainly by the injection of hot and cold fluids from the walls towards the center of the channel. An investigation of the real gas effects at low Mach number conditions indicates that the pressure fluctuations can be considered as a balance between the ideal, repulsive and attractive components of the temperature and density fluctuations.

An analysis of the shock structures for supercritical CO_2 flows under supercritical conditions is performed. For the same pre-shock conditions, the ratio of bulk viscosity to shear viscosity is gradually increased. The results indicate that the shock thickness is increased by the same order of magnitude as the rate of increase in bulk viscosity. In reality, the bulk viscosity of supercritical CO_2 is around 1000 times the magnitude of shear viscosity at room temperature. Thus, bulk viscosity plays a very significant role in determining the characteristics of the shock structure of supercritical CO_2 flows and cannot be ignored in this analysis. However, bulk viscosity is not a significant factor in turbulent flows of supercritical CO_2 at lower Mach numbers. This is due to the fact that the terms involving bulk viscosity in the Navier Stokes equations involve multiplying the bulk viscosity to the dilatation, which is not significant at lower Mach numbers.

Samenvatting

De opwarming van de aarde door het uitstoten van broeikasgassen heeft de wens gecreerd deze uitstoot te beperken door het gebruik van alternatieve bronnen van energie. Vanuit dit oogpunt kunnen superkritische vloeistoffen mogelijk een belangrijke rol spelen vanwege hun toepassing in duurzame technologieen en processen. Deze vloeistoffen hebben een unieke combinatie van gas- en vloeistofachtige eigenschappen die gebruikt kunnen worden in zogenaamde superkritische thermodynamische kringprocessen welke efficienter zijn dan andere methoden van energie omzetting.

In dit thesis onderzoeken wij een turbulente kanaalstroming van superkritisch CO_2 dichtbij het kritieke punt, door het oplossen van de volledig comprimeerbare Navier-Stokes vergelijkingen. Het doel van dit onderzoek is om een beter begrip te krijgen van de fysica in turbulente superkritische stromingen dichtbij het kritieke punt, waar mogelijke compressie-effecten kunnen optreden.

Ons onderzoek heeft tot enkele interessante conclusies geleid. Alleen als de trans-kritieke overgang zich dichtbij de wand bevindt worden er significante compressie-effecten waargenomen. In alle andere gevallen treden deze niet op. De traditionele schaal analyse, met behulp van de van Driest schaling en de uitgebreide van Driest schaling, laat zien dat de meest veranderingen van snelheidsfluctuaties, kinetische energie en gemiddeld snelheidsprofiel, verklaard kunnen worden door de veranderingen in gemiddelde dichtheid en temperatuur. De locatie van de kritieke temperatuur, bij de koude wand of dichtbij het midden van het kanaal, is bepalend voor de aard van de dichtheidfluctuaties. Een kwadrant analyse van de turbulente warmte stroming dichtbij de koude en warme wanden laat zien dat menging op deze plekken voornamelijk gebeurt door de verplaatsing van warme of koude vloeistofgebieden vanuit de wanden richting het midden. Een onderzoek naar de echte-gas-effecten bij lage Mach nummers, laat zien dat drukfluctuaties gezien kunnen worden als een balans tussen de ideale, afstotende en aantrekkende componenten van de temperatuur- en dichtheidsfluctuaties.

Voor de analyse van de schok-structuren van superkritische CO_2 stromingen, is er een onderzoek gedaan waarbij voor dezelfde pre-schok condities, de verhouding van bulkviscositeit en afschuifviscositeit gelijkmatig is verhoogd. De resultaten van dit onderzoek laten zien dat de schokdikte toeneemt met dezelfde mate als de verandering van bulkviscositeit. In werkelijk is de bulkviscositeit van superkritisch CO_2 bij kamertemperatuur, circa 1000 keer zo groot als de afschuifviscositeit. Hierdoor speelt bulkviscositeit een belangrijke rol in het bepalen van de karakteristieken van de schokstructuren van superkritische CO_2 stromingen en kan niet worden verwaarloosd in de analyse. Daarentegen, bulk-viscositeit is geen belangrijke factor in turbulente stromingen van superkritisch CO_2 bij lage Mach nummers. Dit word duidelijk door een analyse van de Navier-Stokes vergelijkingen, de termen waar bulkviscositeit in voorkomen worden vermenigvuldigt met de dilatatie, welke niet significant is bij lage Mach nummers.

1 Introduction

1.1 Sustainable development and renewable energy

Progressive industrialization, population growth and urbanization has led to an increase in energy demand across the world, specially amongst the large developing economies, such as India and China. The over reliance on fossil fuels like coal and petroleum to meet our energy needs has led to a tremendous increase in the emission of carbon dioxide and other greenhouse gases. The reports published by the Intergovernmental Panel on Climate Change (IPCC), such as Stocker (2014); Pachauri *et al.* (2014) estimate several adverse consequences in the near term due to anthropogenic global warming and climate change. These include increase in mean surface air temperatures, shrinking of the Arctic sea ice cover, an increase in the frequency and intensity of heavy precipitation and deterioration of air quality due to a rise in the concentration of greenhouse gases and other particulate matter in the air. The committee of nations in the world jointly acknowledged this as an existential problem and this led to the formation of the United Nations Framework Convention on Climate Change (UNFCCC) (French, 1998). The Kyoto Protocol of 1994 led to firm commitments from various countries to make the necessary technological changes in order to tackle the menace of climate change (Oberthür & Ott, 1999). The Paris Agreement of 2016 is the latest effort to build a global response to climate change and aims to restrict global temperature rise in this century to below 2°Celsius compared to pre industrial levels. This requires a progressive decline of carbon emissions intensity, which can be achieved only by replacing fossil fuels by renewable energy.

1.2 Supercritical fluids and their relevance in sustainable development

The achievement of the international objectives on climate change requires a drastic reduction in our reliance on fossil fuels and a move towards more efficient alternative energies like solar, wind, etc. Supercritical fluids are used, in this context to increase the efficiency of power cycles in internal combustion engines, in gas turbines or in rocket engines, where the fuel or the oxidant are injected into the chamber under supercritical conditions. Such technological applications of supercritical CO_2 are given in Brunner (2010) The critical properties of various fluids, such as the critical pressure (P_c), the critical temperature (T_c) and the critical density (ρ_c) are shown in Table 1.2. Along with an increase in the efficiency of these processes which consume energy and emit greenhouse gases, it is also necessary to restrict further emissions of CO_2 into the atmosphere till the requisite technological changes come into use at a larger scale. Carbon Capture and Storage (CCS) relates to the capture of CO_2 during the pre or post combustion phase of industrial processes, transporting it through pipelines and finally storing it deep underground aquifers, in depleted oil and gas fields or in unmineable coal seams. The CO_2 is normally stored in the supercritical state due to the prevailing conditions in the storage reservoirs. These kinds of technologies are being used to entrap CO_2 and prevent it from going into the atmosphere. The combined effect of the increase

in efficiency by using supercritical fluids along with the entrapment of CO_2 generated from these processes under supercritical conditions help to increase the viability of these technologies.

Presently, electricity generation is responsible for around 29% of the CO_2 emissions in the world. Thus, processes such as the Integrated Gasification Combined Cycle (IGCC) and the Coal-fired Ultra Supercritical Steam Cycles (USCSC) use carbon capture and storage in combination with electricity generation in order to minimize the emissions of CO_2. Very often, the storage of CO_2 is combined with Enhanced Oil Recovery (EOR), Enhanced Gas Recovery (EGR) and enhanced coalbed methane recovery (ECBM) in order to recover the costs for transportation and storage for CO_2. However, the reduction of carbon emissions from existing modes of transportation and electricity generation are not sufficient for meeting the target of limiting global temperature rise to 2°Celsius as envisaged in the Paris Agreement. In this context, the Supercritical Carbon Dioxide Power Cycles, as mentioned in Dostal *et al.* (2006), which use supercritical CO_2 as a working fluid can play a major role in terms of reductions in emissions and cost savings. This technology, which uses a Brayton-Joule cycle has a very high efficiency of around 50% and a footprint of around 1% of that of turbomachinery of similar power output due to a high density of the working fluid. This process produces CO_2 ready for sequestration and can be integrated with other activities like Enhanced Oil Recovery and Concentrating Solar Power, etc. The Sandia National Laboratories in collaboration with the Department of Energy in the USA have done pioneering work in developing a supercritical CO_2 Brayton cycle technology involving areas such as hardware development, performance improvement, modeling and commercialization of supercritical CO_2 power systems. A summary of this research has been described in Wright *et al.* (2011).

CO_2 above its vapour-liquid critical point is known as supercritical CO_2. CO_2 is unique among supercritical fluids in the aspect that it can exist as a supercritical fluid at room temperature. CO_2 behaves like a gas at standard temperature and pressure (STP) and it behaves like a solid called dry ice when it is frozen. But, when both the temperature and pressure are above the critical point, then fluid can neither be called a liquid nor a gas and has a unique mixture of gas-like and liquid-like properties. Above the vapour-liquid critical point, the heat capacity of supercritical CO_2 at constant pressure (C_p) shows a maximum value at a certain temperature, known as the pseudo-critical temperature (T_{pc}). This point is called the pseudo-critical point. The line joining the pseudo-critical points for a range of pressures above the critical point is called the pseudo-critical line. Below the critical point, the fluid exists as a mixture of liquid and vapour in the two phase region. The line separating the supercritical fluid from the two phase region consists of the saturation liquid and the saturation vapour lines. Very near to the critical point, it has density similar to that of a liquid, viscosity akin to that of a gas and diffusivity intermediate to that between liquids and gases. The area bounded by the critical isobar and the critical isotherm represents supercritical fluids and that bounded by the saturation liquid and the saturation vapour line represents the two-phase region. The region in between the saturation vapour line and below the critical isobar represents the fluid as a gas. These details are represented in Figure 1.1 by

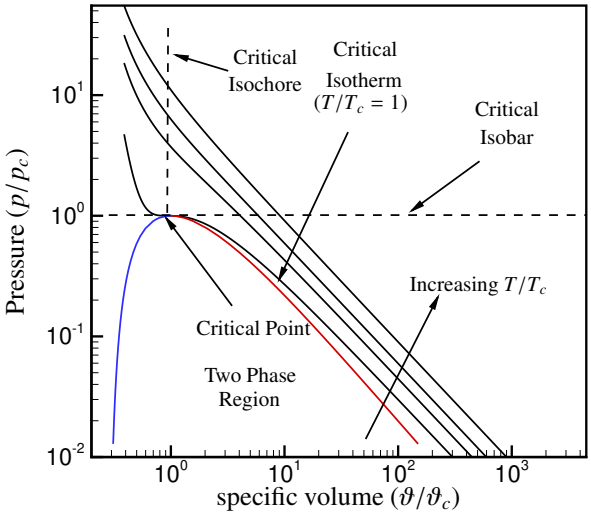

Figure 1.1: Pressure as a function of specific volume normalized by their critical values at constant temperatures for CO_2; (———) T/T_c = 1.0;T/T_c=1.5, T/T_c=2.0, T/Tc=3.0; (———) Saturation liquid line; (———) Saturation vapour line.

plotting the pressure as a function of specific volume at constant temperatures above and below the critical point. The pressure and specific volume are normalized by the critical pressure (P_c) and the critical volume (ϑ_c) of CO_2, respectively. In this case, the pressures and specific volumes have been derived in accordance with the Peng Robinson equation of state which is used to derive the thermodynamic properties in our simulations.

Along any isobar above the critical point, on crossing the pseudo-critical point, all the thermodynamic and transport properties like density, isobaric heat capacity, viscosity and thermal conductivity etc., exhibit sharp gradients for small changes in temperature. This phenomenon is called trans-critical transition. These unique of supercritical CO_2 mentioned above, which include a mixture of gas-like and liquid-like behaviour and the phenomenon of trans-critical transition make it useful for various industrial applications related to sustainable development and energy efficiency. The sharp variation in the properties of CO_2 at 80 bar as a function of temperature is shown in Figure 1.2. These properties have been normalized by the corresponding properties of CO_2 at 80 bar and 300K. The thermodynamic properties, such as, density (ρ) and heat capacity at constant pressure (C_p) are evaluated according to the Peng Robinson equation of state. The transport properties, such as, viscosity (μ) and thermal conductivity (κ) are tabulated in accordance with the models given in Lemmon *et al.* (2010). The reference properties with respect to which the properties in Figure 1.2 are normalized are given in Table 5.1.

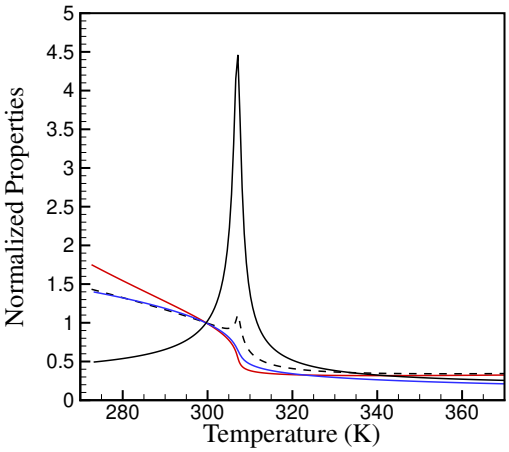

Figure 1.2: Thermodynamic and transport properties of CO_2 as a function of temperature at a constant pressure of 80 bar normalized by their values under the reference conditions of 80 bar and 300 K. (———) Heat Capacity (C_p/C_{p0}); (———) Density (ρ/ρ_0); (———) Viscosity (μ/μ_0); (– – –) Thermal Conductivity (κ/κ_0)

Table 1.1: Density (ρ_0), Heat capacity (C_{p0}), viscosity (μ_0) and thermal conductivity (κ_0) for supercritical CO_2 under the reference conditions of 80 bar and 300 K

ρ_0	C_{p0}	μ_0	κ_0
689.46 kg/m^3	4.98 kJ/kgK	6.093×10^{-5} Pa.s	8.246×10^{-2} W/mK

Table 1.2: Critical properties of various substances (Lemmon *et al.*, 2002).

substance	P_c (bar)	T_c (K)	ρ_c (kg/m^3)
CO_2	73.77	304.13	466.6
H_2O	220.65	647.01	322.4
CH_4	45.99	190.57	161.4
NH_3	113.33	405.40	193.7
O_2	50.43	154.58	460.6
H_2	12.97	33.15	29.6

1.3 Literature review

1.3.1 Experimental studies

A wide range of experimental research has been conducted previously on topics, such as deterioration and enhancement of heat transfer, effects of buoyancy and heat transfer correlations in supercritical fluids. According to Shitsman (1963), heat transfer deterioration occurs in wall-bounded supercritical water flows under a high heat flux environment when the wall temperature is above the critical temperature and the bulk temperature is below the critical temperature. As the fluid is heated, the temperature near the wall increases and the fluid changes from liquid-like to gas-like behaviour. This situation, which resembles that of a phase change is responsible for heat transfer deterioration. The opposite behaviour, i.e., heat transfer enhancement occurs in cooled supercritical fluid flows. This has been reported by previous authors, such as, Shitsman (1963); Hiroaki *et al.* (1971); Krasnoshchekov *et al.* (1969). The enhancement of heat transfer in a cooled supercritical fluid is attributed to the formation of a liquid-like layer with high thermal conductivity. The converse is true in a heated fluid where a gas-like layer with low thermal conductivity is formed.

Previous researchers have also performed experiments with upward and downward flows of supercritical fluids in heated vertical tubes in order to investigate the effects of buoyancy. Based on these experiments, correlations were propounded by authors, such as Hall & Jackson (1969); Petukhov & Polyakov (1974); Adebiyi & Hall (1976) for determining the significance of the buoyancy effects based on the Reynolds number, Prandtl number and Grashof number. Correlations for heating and cooling in supercritical fluid flows were also developed by investigating the Nusselt number from experimental data. Petukhov *et al.* (1961); Krasnoshchekov & Protopopov (1966); Yamagata *et al.* (1972); Ghajar & Asadi (1986) proposed correlations for the Nusselt number in terms of the Reynolds and Prandtl numbers. These correlations developed for supercritical fluids were found to be qualitatively similar to the correlations for single-phase fluids.

1.3.2 Numerical studies

Experimental studies are usually very expensive to conduct and have the limitations of reproducibility and accuracy of measurements. Various simulation techniques were used in order to reproduce the experimental observations without actually conducting the experiments. The most effective among these simulation techniques is Direct Numerical Simulations (DNS), which resolves all the scales of turbulence and thereby, gives a better understanding of turbulent flows. Compared to DNS, other methods, such as Reynolds averaged Navier-Stokes (RANS) or Large Eddy Simulations (LES) are computationally less intensive but suffer from the necessity of taking restrictive modeling assumptions. DNS of fully developed ideal gas flows in a channel geometry were first performed by Kim *et al.* (1987). This work compares the mean and turbulent statistics in such flows with the experimental results obtained by previous authors. These

simulations were performed using the incompressible Navier-Stokes equations. Fully compressible Navier-Stokes equations were used to investigate the turbulent flows of ideal gases at higher Mach numbers with isothermal wall boundary conditions by Coleman *et al.* (1995). Velocity scaling using the van Driest transformation was investigated for turbulent flows at high Mach numbers by Huang *et al.* (1995). Morinishi *et al.* (2004) simulated fully developed and compressible ideal gas flows in a channel geometry at higher Mach numbers using isothermal boundary condition at one wall and adiabatic boundary condition at the other wall. Van Driest scaling and compressibility effects analyzed by investigating the pressure strain correlation were performed by Foysi *et al.* (2004).

In case of turbulent flows of supercritical fluids, it is found that the sharp property variations alter the conventional behaviour of gas dynamics and turbulence. This behaviour cannot be properly represented by the ideal gas equation of state. Therefore, real gas equations are used to represent the thermodynamic behaviour of supercritical fluids, such as, cubic equations or the more recent multi-parameter equations of state. Direct Numerical Simulations for upward annular flows of supercritical CO_2 with constant heat-flux wall boundary conditions was conducted by Bae *et al.* (2005, 2008). It was found that the most singular phenomenon is observed at supercritical pressures when there is trans-critical transition in the flow. This leads to some peculiar characteristics in the turbulent flow field, such as heat transfer deterioration causing the weakening of the velocity streaks near the point of the maxima of temperature fluctuation and also, the weakening of ejection and sweep motions near the wall. Large Eddy Simulation (LES) of a turbulent jet of nitrogen under supercritical pressure was performed by Schmitt *et al.* (2010). It compares low pressure LES simulations and real gas thermodynamics with data extracted from experiments. This approach has indicated that the high density gradients and non-linear thermodynamics has a limited impact on the jet spreading rate and the pseudo-similarity behaviour for jets.

A review of the turbulent flows of supercritical fluids was conducted by Yoo (2013) in order to study various effects like buoyancy, flow acceleration and heat transfer deterioration in supercritical fluid flows. Direct Numerical Simulations of a coaxial jet of supercritical fluids using a van der Waals gas and the low-Mach number approximation Navier- Stokes equations was performed by Battista *et al.* (2014). A numerical method has however been provided by Kawai *et al.* (2015) for conducting high fidelity simulations for supercritical fluids involving trans-critical transition. Nemati *et al.* (2015) has investigated developing turbulent flows of supercritical CO_2 in a pipe geometry involving forced and mixed convection. Large eddy simulations of cryogenic nitrogen injection have been performed by Müller *et al.* (2016) using Peng Robinson equation of state at supercritical pressures. In this paper, various subgrid-scale (SGS) models have been compared and the influence of the density gradients on the growth of instability have been investigated. One dimensional rarefaction properties in compression shocks have been investigated recently by Alferez & Touber (2017) for non-ideal gases close to the vapour-liquid critical point. This paper discusses the redistribution of energy supplied to the flow into the entropy, acoustic and vortical modes for one dimensional compressible turbulent flows. Peeters *et al.* (2017) also investigates

the heat transfer characteristics in fully developed turbulent flows of CO_2 in an annular geometry by simulating the low-Mach number approximation Navier-Stokes equations. Dense gas flows of supercritical fluids near the vapour-liquid critical point at higher Mach numbers has been investigated previously by Sciacovelli *et al.* (2017) and have been found to be qualitatively similar to incompressible flows when the effects of semi-local scaling and extended van Driest scaling are taken into account. From this study, it has also been concluded that the effects of bulk viscosity on the flow are negligible.

In many previous works, such as Bae *et al.* (2008), Yoo (2013), Nemati *et al.* (2016) and Peeters *et al.* (2017), Navier-Stokes equations have been solved using the low-Mach number approximation which takes into account changes in density due to changes in temperature but ignores the effect of density changes due to the pressure variations. In order to further improve our understanding of the thermodynamics of supercritical fluids and also to capture the compressibility effects, a fully compressible Navier-Stokes solver has been developed, which can include the effects of density changes due to the variation of both pressure and temperature.

1.4 Aspects of investigation

The main aspects that have been investigated are the various equations of state, the validity of the different kinds of scaling in supercritical CO_2 flows, the effects of variable transport properties near the vapour-liquid critical point, the compressible effects at higher Mach numbers and the energy transfers measured by the turbulent heat flux budget equations. These have been mentioned in more details in the following sections.

1.4.1 Equations of state

The sharp gradients in the properties of fluids near the vapour-liquid critical point cannot be captured using the ideal gas equation of state. Hence, a real gas equation has to be used in our simulations, which is suitable for representing the thermodynamics of supercritical CO_2. In the development of real gas cubic equations of state, one of the first steps was taken by Van der Waals (1873) who developed the van der Waals equation of state. This equation took into account the volume occupied by the molecules and the intermolecular forces of attraction and repulsion in real gases, which are not captured in the ideal gas equation of state. The virial equation of state Onnes (1901) is not a cubic equation of state but was developed out of statistical mechanics. This equation takes into account the intermolecular forces not only between two molecules but also between triplets and higher order interactions, where more than three molecules exert forces of attraction or repulsion on each other. In the case of real gases, the volume available for the motion of the gas molecules is less than the volume of the container. This is due to the fact that the volume occupied by the individual gas molecules has to be taken into account. Improvements to the van der Waals equation were progressively made by Redlich & Kwong (1949) and also by Soave (1972) who modified the existing Redlich

Kwong equation of state. These provide substantially better results in predicting the properties of real gases and also the properties of supercritical CO_2 near the vapour-liquid critical point compared to the van der Waals equation of state. The Peng Robinson equation of state was developed by Peng & Robinson (1976) in order to overcome some of the shortcomings in the Redlich Kwong and the Soave Redlich Kwong equation of state, especially for larger hydrocarbons near their respective critical points.

In more recent times, the multiparameter equations of state, such as those developed by Span & Wagner (1996) and also by Kunz *et al.* (2007); Kunz & Wagner (2012) have been used to predict the thermodynamic properties of real gases. These differ from the cubic equations of state in the aspects that these rely on predictions from optimized values detected in experiments. The fundamental variable in these equations is the Helmholtz free energy. The equations also have separate forms for polar and non-polar molecules. These equations have been found to be extremely accurate in predicting the properties of supercritical fluids near the critical point. The equation of state developed by Kunz & Wagner (2012) is used in the Refprop library (Lemmon *et al.* (2010)) for supercritical fluids.

Extremely close to the critical point, the scaling law equation of state, described in Levelt (1970); Sengers *et al.* (1983) can provide very accurate predictions but the scope of the validity of these equations is very limited. In our simulations, it is not required to go so near to the critical point as to necessitate the use of the scaling laws. Thus, the scaling law equation of state is not taken into consideration.

The choice has to be made between the cubic equations of state, such as, van der waals, Redlich Kwong, Peng Robinson and also the more recently developed multiparameter equations of state, such as Span & Wagner (1996) and Kunz & Wagner (2012). The cubic equations of state are fairly simple to implement directly in the Navier-Stokes solver. But, the multiparameter equations of state are more complicated and thus, the thermodynamic properties have to be stored in a lookup table. Several factors have been taken into consideration whilst making this choice, such as, accuracy, consistency and computational efficiency. The Peng Robinson equation of state is chosen as the preferred equation after a careful analysis of all the above factors. The reasons for choosing the Peng Robinson equation for the simulations are mentioned in more details in the subsequent chapters.

1.4.2 Scaling Analysis

In turbulent flows, the outer scaling has been used by previous authors, such as Kim *et al.* (1987); Coleman *et al.* (1995) to collapse the turbulent statistics. However, this scaling has not been found to be useful for collapsing the turbulent statistics in compressible turbulent flows for ideal gases. For compressible flows, the inner scaling or the semi-local scaling has been used by previous authors, such as, Coleman *et al.* (1995); Huang *et al.* (1995) to collapse the turbulence statistics to that of incompressible flows. The validity of these scaling methodologies has been examined for fully compressible and turbulent flows of supercritical CO_2. This scaling analysis also validates the

Morkovin hypothesis which states that turbulence is only determined by the mean density gradients and density fluctuations have a minimal role in influencing the turbulence structures in compressible turbulent flows. Previously, the van Driest transformation has been used by various authors to scale the velocity profile in wall-bounded turbulent flows. More recently, the velocity transformation developed by Patel *et al.* (2016); Trettel & Larsson (2016) has been proved to be better than the van Driest transformation for scaling the velocity profile in turbulent flows. The validity of these velocity transformations has also been tested for the simulations in supercritical CO_2. The influence of the semi-local scaled Reynolds number on turbulence statistics, such as anisotropy has also been examined.

1.4.3 Effect of variable transport properties

The transport properties of supercritical CO_2, such as, viscosity and thermal conductivity exhibit sharp gradients due to trans-critical transition near the vapour-liquid critical point. The effect of variable transport properties on turbulence has been previously investigated by Zonta *et al.* (2012) for incompressible turbulent flows and by Morinishi *et al.* (2004) for compressible turbulent flows of ideal gases. These investigations have revealed that for incompressible turbulent flows with variable viscosity and isothermal walls at different temperatures, the change of viscosity results in an increase in the production and a decrease in the dissipation of turbulent kinetic energy near the cold wall. The reverse behaviour is observed near the hot wall. In our simulations, we investigate the effects of variable transport properties by comparing mean and turbulent statistics from constant and variable transport property cases at the same Reynolds number and Mach number and also having the same set of isothermal wall boundary conditions. The same effects detected by Zonta *et al.* (2012) for incompressible flows is also observed in our turbulent compressible flow simulations of supercritical CO_2 with variable transport properties. However, the semi-local scaled budget terms for turbulent kinetic energy near both the hot and cold walls of the channel are found to collapse on top of each other. This proves that the changes in the turbulent kinetic energy budgets near the hot and cold walls can be accounted for entirely by considering the effects of the variations in mean density and mean viscosity. This also establishes that the effects of the turbulent fluctuations in density and viscosity on the budget terms is negligible.

1.4.4 Compressiblity effects

Previous authors, such as Nemati *et al.* (2015, 2016) and Peeters *et al.* (2017) have performed the DNS of supercritical fluids using the low-Mach number approximation Navier-Stokes equations. This can take into account the variations in density due to the change of temperature but ignores the variations in density due to the change in pressure. The bulk pressure is assumed to be constant in the Navier-Stokes equations that use the low-Mach number approximation. In our simulations, however, we have used the fully compressible Navier-Stokes equations that take into account the variations in density due

to the changes in temperature as well as the changes in pressure. Thus, we also take into account intrinsic compressibility in contrast to the low-Mach number approximation Navier-Stokes equations. Compressibility effects have been evaluated by previous authors, such as, Coleman *et al.* (1995); Morinishi *et al.* (2004); Wei & Pollard (2011) using the terms for compressibility effects in the budget equation for turbulent kinetic energy. Compressibility effects for high Mach number flows have been evaluated by Foysi *et al.* (2004) by studying the pressure strain correlation and comparing it to that of incompressible flows. The compressibility effects in the flow field have been evaluated by authors, such as, Sinha & Candler (2003); Kreuzinger *et al.* (2006) by comparing the solenoidal dissipation to the total dissipation. In addition, the velocity field can be decomposed into its solenoidal and dilatational components. These represent the incompressible and the compressible parts of the velocity field, respectively. This is referred to as Helmholtz decomposition. This has been done previously by Sarkar (1995) for shear flows and a general explanation of it's application is provided by Joseph (2006) for any smooth velocity field. From our simulations, the contribution of the solenoidal and the dilatational components in the terms, such as production, diffusion and dissipation represented in the budget of turbulent kinetic energy, have been evaluated.

1.4.5 Energy transfers

The mechanisms for the exchange of energy from the mean internal energy to the turbulent kinetic energy and mean kinetic energy are studied by using the budget equation given by Lele (1994). A budget equation has also been developed to study the transport of turbulent heat flux in the wall normal direction. This has also been done by previous authors, such as, Nemati *et al.* (2016) for developing turbulent flows of supercritical CO_2 in a pipe geometry and also by Peeters *et al.* (2017) for fully developed flows of supercritical CO_2 in an annulus. But, both of these investigations used the low-Mach number approximation Navier-Stokes equations and used an energy equation based on enthalpy. In our simulations, the fully compressible Navier-Stokes equations are used and this ensures the contribution of the viscous heating terms in the budget equation. Also, in our equations, the conservative variable is the total energy which is the sum of the internal energy (e) and the kinetic energy. The enthalpy (h) is related to the internal energy as $h = e + P/\rho$, where P is the pressure and ρ is the density. The turbulent heat flux in the wall normal direction is thus defined as the transport of the Favre averaged fluctuating enthalpy ($\rho h''$) by the Favre averaged fluctuating component of the wall normal velocity (v''). Thus, the turbulent heat flux in the wall normal direction is defined as $\overline{\rho h'' v''}$. The budget terms, such as the production, diffusion and the dissipation of the turbulent heat flux indicate the increase or decrease in turbulence in the internal energy at different points in the flow field.

1.5 Motivation

The applicability of supercritical CO_2 in increasing more efficient power cycles and thereby promoting sustainable practices has made it essential to have a better understanding of the physics of turbulent flows of CO_2 near the vapour-liquid critical point. Our simulations also simulate fully developed turbulent flows at higher Mach numbers thereby providing the opportunity to analyze compressibility effects. Experiments are usually very expensive to set up and conduct, are not easy to replicate and suffer from the lack of accuracy of taking measurements. RANS or LES simulations involve restrictive modeling assumptions and do not provide the complete picture in understanding turbulent flows near the critical point. Direct Numerical Simulations are not restricted by the necessity of taking restrictive modeling assumptions and are capable of analyzing all the scales of turbulent motion. The use of fully compressible Navier-Stokes equations helps us to study separately the effects such as differing locations of trans-critical transition, variable transport properties and higher Mach numbers on turbulence in the flow.

1.6 Thesis Outline

The thesis has been divided into the following chapters.

In Chapter 2, the details of the fully compressible non-dimensionalized Navier-Stokes equations are mentioned. The tools used in the parallelization of the code, such as 2DECOMP&FFT library with 2D pencil decomposition have also been described. The numerical details, such as, the RK3 method used in temporal discretization, the compact finite difference schemes used in spatial discretization and the skew symmetric method used to nullify aliasing errors have been given in detail.

In Chapter 3, the rationale for choosing Peng Robinson as our preferred equation of state is mentioned. This includes a comparison of the different factors, such as, accuracy and consistency that have been taken into account in making this choice. In this context, the thermodynamic properties like heat capacity at constant pressure (C_p), density, speed of sound, isothermal compressibility, etc predicted by the different cubic equations of state have been compared to that predicted by the Refprop library near the vapour-liquid critical point of CO_2. Finally, the implementation of the transport properties, such as, viscosity and thermal conductivity, using lookup tables have been described.

In Chapter 4, the details of the cases of supercritical CO_2 simulated are given. Next, the results derived from the simulations including the mean and turbulent statistics, the scaling analysis, effects of variable transport properties, compressibility effects and energy transport are given in succession.

In Chapter 5, a van der Waals model has been used to develop the equations used for calculating shock structure in real gases. The influence of bulk viscosity for shock structure in case of carbon dioxide near the vapour-liqiuid critical point has been investigated.

In Chapter 6, the results of the simulations mentioned in the previous chapters are summarized and the main conclusions drawn from the results are mentioned.

2

Governing equations and computational details

2.1 Introduction

Near the vapour-liquid critical point of CO_2, the fully compressible Navier-Stokes equations are coupled with real gas equations of state in order to get an accurate picture of both compressibility effects as well as real gas thermodynamics. The simulations performed relate to the fully developed turbulent flows of supercritical CO_2 in a channel near the vapour-liquid critical point of CO_2. The equations that are used to perform the simulations of carbon dioxide near the vapour-liquid critical point include the fully compressible Navier-Stokes equations, an appropriate thermodynamic equation of state and the transport models which are used to calculate the viscosity and thermal conductivity. The low-Mach number approximation Navier-Stokes equations which was used by previous authors, such as, Nemati *et al.* (2015); Peeters *et al.* (2017) capture the variation in density only due to the change of temperature but ignore the effect of changes in pressure. This limitation has been overcome by using the fully compressible Navier-Stokes equations as they can capture the variations in density due to the changes in both temperature and pressure. The Peng Robinson equation has been chosen as the preferred equation of state after careful consideration. The reasons for this choice have been explained clearly in Chapter 3. The transport properties are evaluated using transport models which are tabulated in the Refprop library Lemmon *et al.* (2010).

2.2 Governing equations

2.2.1 Fully compressible Navier-Stokes Equations

An in-house code has been developed to solve the compressible Navier-Stokes equations in Cartesian coordinates for fully developed turbulent flow in a channel. The continuity, momentum and energy equations are solved for the density (ρ), the components of momentum in three directions (ρu_i) and the total energy (ρe_0), respectively. The total energy is expressed as $\rho e_0 = \rho e + 1/2\rho u_i^2$, where e is the internal energy and $1/2\rho u_i^2$ is the kinetic energy. The non-dimensional Navier-Stokes equations are given as follows.

$$\frac{\partial \rho}{\partial t} + \frac{\partial \rho u_j}{\partial x_j} = 0, \tag{2.1}$$

$$\frac{\partial \rho u_i}{\partial t} + \frac{\partial \left(\rho u_i u_j + P\delta_{ij} - \Gamma_{ij}\right)}{\partial x_j} = \rho f_i, \tag{2.2}$$

$$\frac{\partial \rho e_0}{\partial t} + \frac{\partial \left(u_j \rho e_0 + u_j P + q_j - u_i \Gamma_{ij}\right)}{\partial x_j} = \rho u_j f_j, \tag{2.3}$$

where μ is the viscosity, P denotes the pressure, κ is the thermal conductivity and f_i is the applied forcing term in streamwise direction for the keeping the mass flux at the desired value. The applied forcing term is analogous to $(-1/\rho)\,\partial P/\partial x$ for pressure driven flows

and is calculated in a way such the quantity $\int_y \rho U dy$ is conserved. The non-dimensionalization is performed as follows

$$x_i = \frac{x_i^\star}{H^\star}, \quad t = \frac{t^\star U_0^\star}{H^\star}, \quad e_0 = \frac{e_0^\star}{U_0^{\star 2}}, \quad u_i = \frac{u_i^\star}{U_0^\star},$$

where $U_0^\star$ is the bulk velocity.

The non-dimensionalization for the pressure, temperature and density is performed as follows

$$P = \frac{P^\star}{\rho_0^\star U_0^{\star 2}}, \quad \rho = \frac{\rho^\star}{\rho_0^\star}, \quad T = \frac{T^\star}{T_0^\star}. \tag{2.4}$$

The non dimensional transport properties, such as the viscosity μ and the thermal conductivity κ are given by $\kappa = \kappa^\star/\kappa_0^\star, \mu = \mu^\star/\mu_0^\star$. The non-dimensional numbers, namely, the Reynolds number, Prandtl number and Mach number are defined as

$$Re = \frac{\rho_0^\star U_0^\star H^\star}{\mu_0^\star}, \quad Pr = \frac{\mu_0^\star C_{p0}^\star}{\kappa_0^\star}, \quad M = \frac{U_0^\star}{C_0^\star}, \tag{2.5}$$

where $C_0^\star$ is the speed of sound under the reference conditions of 80 bar and 300 K. The bulk velocity $U_0^\star$ is determined by the Mach number M and the speed of sound under the reference conditions $C_0^\star$, calculated using a cubic equation of state, discussed in chapter 3. The subscript 0 is used to denote properties at the reference conditions mentioned above in all future symbol notations. The Eckert number, which is referred to here as the pseudo Mach number is used to non-dimensionalize the heat conduction term. It is given as follows

$$M_{ps}^2 = \frac{U_0^{\star 2}}{C_{p0}^\star T_0^\star}. \tag{2.6}$$

The viscous stress Γ_{ij} and q_j the heat flux defined as

$$\Gamma_{ij} = \frac{\mu}{Re}\left[\left(\frac{\partial u_i}{\partial x_j} + \frac{\partial u_j}{\partial x_i}\right) - \frac{2}{3}\delta_{ij}\frac{\partial u_k}{\partial x_k}\right], \tag{2.7}$$

$$q_j = -\frac{\kappa}{RePrM_{ps}^2}\frac{\partial T}{\partial x_j}. \tag{2.8}$$

2.2.2 Models for transport properties

The Refprop library calculates transport properties, such as viscosity and thermal conductivity using the transport models developed by previous authors Fenghour *et al.* (1998); Vesovic *et al.* (1990). These models state that the total viscosity $\mu(\rho, T)$ and thermal conductivity $\kappa(\rho, T)$ as a function of the density ρ and temperature T can be

expressed as a sum of three independent contributions. Representing either property as $X(\rho, T)$, we get

$$X(\rho, T) = X^0(T) + \Delta X(\rho, T) + \Delta X_c(\rho, T), \tag{2.9}$$

where $X^0(T)$ represents the contribution to the transport property in the limit of zero density. This includes the effect of only two body molecular interactions. The term $\Delta X(\rho, T)$ is called the excess property and it represents the contributions of all other effects on the transport properties at higher densities, such as many body collisions, molecular velocity correlations and collisional transfer. The term $\Delta X_c(\rho, T)$ represents the critical enhancement which is caused by the long range fluctuations near the critical point that are responsible for causing divergences in the viscosity and thermal conductivity. The terms $X^0(T)$ and $\Delta X_c(\rho, T)$ are treated theoretically but, there is no proper theoretical explanation for the term $\Delta X(\rho, T)$ and experimental measurements are used in order to determine this contribution. After conducting the relevant experiments over different ranges of temperatures, it was found that the temperature dependence of the term $\Delta X(\rho, T)$ is negligible. So, it was represented as a function of only density as $\Delta X(\rho)$. For both viscosity and thermal conductivity, the values of this excess contribution was determined by experiments and it is represented by fitting a polynomial equation to the experimental values. This is given by the following equation.

$$\Delta X(\rho) = \sum_{i=1}^{4} c_i \rho^i, \tag{2.10}$$

where c_i is the optimized coefficient of the i^{th} exponent of the density ρ. The other terms can be determined analytically as mentioned in Vesovic *et al.* (1990). The viscosity and thermal conductivity as evaluated by these models are tabulated in the Refprop library (Lemmon *et al.* (2010)). These are shown in Figure 2.1 for supercritical CO_2 at constant pressure as a function of temperature.

2.3 Implementation of the transport properties

The Refprop library calculates transport properties, such as viscosity and thermal conductivity using the transport models developed by previous authors Fenghour *et al.* (1998); Vesovic *et al.* (1990). Instead of directly calling Refprop, the transport properties are tabulated within a relevant range for temperature and pressure and are then stored in a lookup table. For any point inside the flow domain, transport properties like viscosity and thermal conductivity are uniquely determined at each point by calculating the indices in the lookup table and using a 2^{nd} order bilinear interpolation method to interpolate between the closest points. The lookup table approach for calculating the transport properties is not computationally expensive as it involves a cartesian table in temperature and pressure, which are previously calculated using the Peng Robinson equation of state. As temperature and pressure are both known inputs to the table, the indices can be calculated directly without employing a search algorithm.

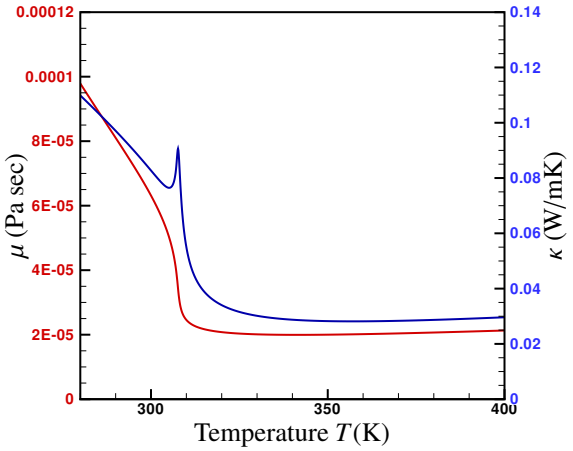

Figure 2.1: Viscosity (μ) and thermal conductivity (κ) for supercritical CO_2 at 80 bar as a function of temperature (T). (——) Viscosity (μ); (——) Thermal Conductivity (κ)

2.4 Spatial discretization schemes

A fully collocated mesh is used to solve the Navier-Stokes equations. This means that all the variables in the Navier-Stokes equations are defined at the center of the cell. In the wall-normal direction, a finite difference scheme is used in which the derivatives for the advective and the diffusive terms are obtained by interpolating the quantities to the cell faces and then differentiating to obtain the values of the derivatives at the cell center. The interpolation and differentiation near the center of the channel are performed in accordance with the 6$^{\text{th}}$ order compact finite difference method developed by Lele (1992) for collocated meshes.

2.4.1 Compact finite difference interpolation scheme

The interpolated values of the variables $\widehat{f_i}$ at the i$^{\text{th}}$ location on the cell faces are derived from the values at the cell center according to the following scheme

$$\beta\widehat{f_{i-2}} + \alpha\widehat{f_{i-1}} + \widehat{f_i} + \alpha\widehat{f_{i+1}} + \beta\widehat{f_{i+2}} = \frac{c}{2}\left(f_{i+5/2} + f_{i-5/2}\right) + \frac{b}{2}\left(f_{i+3/2} + f_{i-3/2}\right) + \frac{a}{2}\left(f_{i+1/2} + f_{i-1/2}\right). \quad (2.11)$$

The values at the cell center are denoted by the fractional subscripts and the interpolated values at the cell faces are denoted by the integral subscripts. The constraints equations for the parameters α,β,a, b and c are determined by performing a Taylor expansion and matching the values up to the 6$^{\text{th}}$ order terms. The relationships between the parameters

are as follows

$$a = \frac{75 + 70\alpha - 42\beta}{64}, b = \frac{270\beta + 126\alpha - 25}{128}, c = \frac{70\beta - 10\alpha + 3}{128}. \tag{2.12}$$

The constraint equations are closed by setting $\beta = c = 0$, which leads to a 6^{th} order tridiagonal system with

$$\alpha = \frac{3}{10},\ a = \frac{3}{2},\ \text{and}\ b = \frac{1}{10}. \tag{2.13}$$

2.4.2 Compact finite difference derivative scheme

The formulation for the 6^{th} order compact finite difference derivative scheme for collocated meshes is as follows.

$$\beta f'_{i-5/2} + \alpha f'_{i-3/2} + f'_{i-1/2} + \alpha f'_{i+1/2} + \beta f'_{i+3/2} = c\frac{f_{i+2} - f_{i-3}}{5h} + b\frac{f_{i+1} - f_{i-2}}{3h} + a\frac{f_i - f_{i-1}}{h}, \tag{2.14}$$

where the variables f_j s are defined at the half height $h/2$ in between two cell faces at the locations $(i - 5/2)$, $(i - 3/2)$, $(i - 1/2)$, $(i + 1/2)$, $(i + 3/2)$ and $(i + 5/2)$. The first derivatives of the variable f'_j are calculated at the collocated locations or the cell center which are given by the fractional indices. The constraints on the coefficients are derived by expanding the terms on the right hand side in accordance with the Taylor series and by matching the terms up to the 6^{th} power. This produces a 6^{th} order accurate method. The constraint equations for the variables are given as

$$a = \frac{225 - 206\alpha - 254\beta}{192}, b = \frac{414\alpha - 114\beta - 25}{128}, c = \frac{9 - 62\alpha + 1618\beta}{384}. \tag{2.15}$$

A tridiagonal matrix is generated by setting $\beta = c = 0$. Substituting the values of β and c into the above equation, we get $\alpha = 9/62$, $b = 17/62$ and $a = 63/62$.

A non-uniform mesh is used in order to have a smaller mesh spacing near the walls and coarser near the center of the channel. For this reason, a hyperbolic tangent function relates the mesh coordinate y with the mesh index i. Therefore, the first derivative in the wall normal direction for any quantity X is implemented as follows,

$$\frac{\partial X}{\partial y} = \frac{\partial i}{\partial y}\frac{\partial X}{\partial i} = \frac{1}{y'}\frac{\partial X}{\partial i}. \tag{2.16}$$

The partial derivative of the wall normal coordinate y with respect to the index i, denoted by y' is called the stretching parameter. This is an analytical function and can be precisely evaluated.

2.4.3 Boundary conditions

In the simulations performed for the flow of supercritical CO_2 through the channel, there is a Dirichlet boundary condition for the velocity at the wall due to the no slip boundary condition. At both the walls, isothermal boundary conditions are imposed due to which a Dirichlet boundary condition has also to be implemented for temperature at the wall. On interpolating the values to the cell faces, the velocities are set to zero at the wall. Boundary conditions are not required in the advective terms for density and total energy as all the advective terms involving density and total energy at the wall are multiplied by the velocity at the wall making the values of these terms equal to zero.

The viscous terms involving the velocities in the momentum equation and the conductivity terms involving the temperature in the energy equation require calculating the first derivative at the cell faces and then, using the derivatives at the faces to calculate the second derivatives at the cell center. The calculation of the first derivatives at the cell faces has been described in Boersma (2011) and is done in the following manner.

$$f'_0 + 15f'_1 = \frac{16}{15}q + 15f_{1/2} - \frac{50}{3}f_{3/2} + 3/5f_{5/2} + O\left(h^4\right), \tag{2.17}$$

$$f'_n + 15f'_{n-1} = \frac{16}{15}q + 15f_{n-1/2} - \frac{50}{3}f_{n-3/2} + 3/5f_{n-5/2} + O\left(h^4\right), \tag{2.18}$$

where the value of the variable at the boundary is set as q and n is the size of the mesh in that particular direction.

2.4.4 Minimization of aliasing errors: Skew symmetric formulation

In the periodic directions, the domain is parallelized using 2DECOMP&FFT library with 2D pencil decomposition as shown in Figure 2.2. Forward Fast Fourier Transform is used to transform the variables in the Fourier space. The derivatives are calculated in the Fourier space and thereafter, the backward transform is used to bring the variables back to the physical space. As the derivatives are calculated in the Fourier space, they are affected by the quadratic and cubic non-linearities present in the fully compressible Navier-Stokes equations. This creates aliasing errors due to the presence of spurious modes as explained by previous authors, such as Blaisdell *et al.* (1996). This can be resolved by traditional methods, such as clipping the modes as mentioned in Canuto *et al.* (2012) in order to eliminate the impact of spurious modes. But, clipping the modes necessitates the use of a bigger mesh in the periodic directions in order to capture the required number of scales in the energy cascade, thus making it computationally inefficient. This difficulty can be overcome by using the pseudo skew symmetric method which was used by previous authors, such as Morinishi (2010). This method is explained as follows. In this method, the advective term for a variable ϕ in the Navier-Stokes equation is given as $\partial\left(\rho u_j \phi\right)/\partial x_j$. This can be written as

$$\frac{\partial \rho u_j \phi}{\partial x_j} = \alpha \frac{\partial \rho u_j \phi}{\partial x_j} + (1-\alpha)\left(\rho u_j \frac{\partial \phi}{\partial x_j} + \phi \frac{\partial \rho u_j}{\partial x_j}\right), \tag{2.19}$$

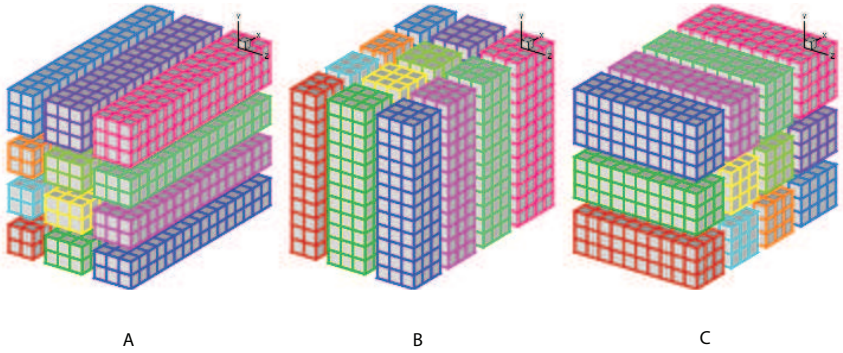

Figure 2.2: 2D domain decomposition example using 12 processors: (A) decomposed in Y and Z direction; (B) decomposed in X and Z direction; (C) decomposed in X and Y direction (Li & Laizet, 2010).

where α is a positive constant between 0 and 1. This formulation has been found to reduce the magnitude of the aliasing error and is referred to as the pseudo skew symmetric formulation when $\alpha = 1/2$. The advective term then reduces to the following expression

$$\frac{\partial \rho u_j \phi}{\partial x_j} = \frac{1}{2}\left(\frac{\partial \rho u_j \phi}{\partial x_j} + \rho u_j \frac{\partial \phi}{\partial x_j} + \phi \frac{\partial \rho u_j}{\partial x_j}\right). \tag{2.20}$$

In our simulations, this formulation is used in the momentum equations where $\phi = u_i$ and in the energy equation where $\phi = e_0$.

2.5 Temporal discretization scheme

There exists a wide variety of choices in choosing an appropriate method for time integration. Single step explicit methods, such as the forward Euler method can determine the values at the next point in time using short time steps. Linear multistep methods, such as the Adams Bashforth method use the values of the variable at previous points in time in order to determine the value of the variable at the next point in time. Adams Moulton methods are also multistep methods similar to the Adams Bashforth methods, the difference being that they are implicit methods which necessitates solving a tridiagonal matrix for performing the time integration. Other implicit methods include the backward Euler method and the trapezoidal method. There are also the predictor-corrector methods which consists of two steps, the prediction step and the corrector step. It uses an explicit multistep method to give an inital estimate of the variable in the prediction step. The corrector step uses an implicit method to refine this initial estimate. The details of these methods are mentioned in works done by previous authors, such as Ziegel (1987); Wanner & Hairer (1991); Butcher (2016).

The time integration method chosen for our simulations is the total variation diminishing (TVD) 3rd order Runge Kutta method, as mentioned in Kupka *et al.* (2012);

Gottlieb & Shu (1998). According to this method, the value of a physical quantity ϕ^{n+1} at the $(n+1)^{th}$ time step is calculated from its current value ϕ^n through the following steps.

$$\begin{aligned} \phi^{n+1/3} &= \phi^n + 0.5\Delta t L\left(\phi^n\right), \\ \phi^{n+2/3} &= \phi^n + \Delta t\left(-L\left(\phi^n\right) + 2L\left(\phi^{n+1/3}\right)\right), \\ \phi^{n+1} &= \phi^n + \Delta t\left(L\left(\phi^n\right) + 4L\left(\phi^{n+1/3}\right) + \left(\phi^{n+2/3}\right)\right)/6, \end{aligned} \tag{2.21}$$

where the equation with respect to which the time integration is being performed is given by $\partial\phi/\partial t = L(\phi)$ and $\phi^{n+1/3}$ and $\phi^{n+2/3}$ give the value of the variable calculated at points intermediate between the n^{th} and the $(n+1)^{th}$ time steps. This is an example of an explicit intermediate step method. As the method is explicit in nature, the solution is determined directly and it is not necessary to solve a tridiagonal matrix as is the case with implicit methods. Also, implicit methods require the derivatives to be linearized, which is not suitable for analyzing turbulent flows. The term intermediate step method implies that it takes into account the slopes at points intermediate between two successive points in time. The advantages of this method include the fact that this scheme preserves stability and monotonicity. This method is also easy to implement and it is self starting. It does not require the starting values from previous time points to begin the time integration, as is the case with Adams Bashforth methods and therefore has lower memory storage requirements than the Adams Bashforth and the Adams Moulton methods. These advantages greatly override the disadvantage that this method is computationally more expensive than the Adams Bashforth and the predictor-corrector methods.

3

Real gas equations of state and their applicability in Direct Numerical Simulations

3.1 Introduction

In this chapter, the different kinds of equations of state in use for real gases, such as the multiparameter equations of state, the scaling laws and the cubic equations of state are explored. The reasons for choosing a cubic equation of state have been explained and also, the considerations behind the choice of the Peng Robinson equation are mentioned in detail.

3.2 Overview of the equations of state close to the critical point

Close to the vapour liquid critical point of CO_2, the ideal gas equation of state cannot accurately describe the properties of the fluid due to the sharp variations for small changes in the temperature (T) and the density (ρ). So, real gas equations of state have to be used. Among the real gas equations, the cubic equations of state, such as van der Waals, Redlich Kwong and Peng Robinson equations of state are known to provide a good representation of the thermodynamic properties of the fluid near the critical point. The multiparameter equations of state, such as Span and Wagner and Kunz and Wagner equations of state are derived based on optimization and not from the first principles like the cubic equations of state. These are more computationally expensive to implement, but provide a far more accurate description of the properties. Only very close to the critical point, the scaling laws are used but their validity extends to a small region near the critical point. Thus, the scaling laws do not have applicability over a wide range. The various forms of the equations of state are described below.

3.2.1 Multiparameter Equations of state

The multiparameter equations of state are empirical equations of state, which implies that they are derived by fitting model coefficients and parameters to experimental data. These equations are formulated in terms of the reduced Helmholtz free energy ($a(T,\rho)/RT$). The reduced Helmholtz free energy is split up into the sum of the contribution $a^0(T,\rho)/RT$ from the ideal gas and the residual contribution $a^r(T,\rho)/RT$ of the real fluid . This has been described by previous authors, such as Span & Wagner (1996) and is expressed as follows.

$$\frac{a(T,\rho)}{RT} = \frac{a^0(T,\rho) + a^r(T,\rho)}{RT} = \alpha^0(\tau,\delta) + \alpha^r(\tau,\delta), \tag{3.1}$$

where $\tau = T_c/T$ is the inverse reduced temperature and $\delta = \rho/\rho_c$ is the reduced density. The ideal gas contribution can be easily derived according to the following formula.

$$a^0 = \int_{T_0}^{T} C_p^0 dT + H^0 - RT - T\int_{T_0}^{T} \frac{C_p^0 - R}{T} dT - RT ln\left(\frac{\rho}{\rho^0}\right) - Ts^0, \tag{3.2}$$

where $\rho^0 = P^0/RT^0$ is the density, H^0 is the enthalpy, C_p^0 is the heat capacity and s^0 is the entropy of the fluid in a reference state. The residual contribution from the real gas is given as follows.

$$\alpha^r(\tau,\delta) = \sum_{i=1}^{I_{pol}} n_i \tau^{t_i} \delta^{d_i} + \sum_{i=1}^{I_{exp}} n_i \tau^{t_i} \delta^{d_i} exp\left(-\delta^{p_i}\right), \tag{3.3}$$

where I_{pol} and I_{exp} are the number of polynomial and exponential terms; n_i denotes the coefficients; d_i, t_i and p_i represent the exponents. These coefficients and exponents and also the number of polynomial and exponential terms vary for the different multiparameter equations of state written by different authors. For example, $I_{pol} = 6$, $I_{exp} = 12$ for Span & Wagner (1996); $I_{pol} = 8$, $I_{exp} = 19$ for the functional form developed by Miyamoto & Watanabe (2001, 2000, 2002); and $I_{pol} = 13$, $I_{exp} = 32$ for the equation proposed by Friend *et al.* (1989, 1991). The number of terms and also the values of the coefficients and exponents are different in case of polar and non-polar fluids. The multiparameter equation developed by Kunz & Wagner (2012) has been used in the Refprop library Lemmon *et al.* (2010) to calculate the thermodynamic properties of CO_2. As these equations are based on an optimized fit to experimental data, they provide a very accurate estimation near the vapour-liquid critical point of CO_2. However, they involve a very large number of terms. Owing to this complexity, it is computationally expensive to implement these equations directly in the Navier-Stokes solver. The thermodynamic variables can be tabulated using look-up tables with respect to the variables, such as density and internal energy. The temperature and pressure can then be evaluated using an appropriate interpolation method. This approach was investigated and it was found that the methods of interpolation, such as the bilinear and Lagrangian interpolation methods would suffer from the problems of consistency due to the large gradients near the critical point. The issues regarding the consistency of interpolation methods have been enumerated by previous authors, such as Rinaldi *et al.* (2012).

3.2.2 Scaling laws

The properties of the fluid extremely close to the critical point can be best described with the help of the scaling laws developed by Levelt (1970); Sengers *et al.* (1983). These laws express the thermodynamic variables near the critical point as a function of the distance r of the thermodynamic state with respect to the critical point and the contour variable θ which gives the location of the thermodynamic state along a constant r line, such that $\theta = -1$ represents the dew line and $\theta = +1$ represents the bubble line. The scaling laws have proved to be extremely accurate near the critical point, but their zone of applicability is restricted to a small zone close to the critical point. For the purpose of our simulations, it is not required to go so close to the critical point that it necessitates the use of the scaling laws.

3.2.3 Cubic equations of state

Cubic equations of state provide a simple analytical relationship for the calculation of thermodynamic variables near the critical point. Although these are not as accurate as the multiparameter equations of state, the problems of storing large numbers of variables in look-up tables is avoided. Thus, the cubic equations are faster to implement and provide a reasonably accurate depiction of thermodynamic variables near the critical point, whilst using a lesser amount of memory compared to the look-up table approach. The cubic equation of state (EOS) to be used is chosen by comparing the accuracy of the thermodynamic properties predicted by the different cubic equations near the critical point of CO_2.

The thermodynamic properties like density (ρ), heat capacity (C_p), isoenthalpic compressibility (Ψ_{H^0}) and the speed of sound (c) predicted by the van der Waals (VdW), Peng Robinson (PR) and Redlich Kwong (RK) equation of state at the constant pressure of 80 bar near the critical point of supercritical CO_2 are compared with the actual value of these properties extracted from the Refprop library. This is done as follows.

3.3 Van der Waals equation of state

The van der Waals (VdW) equation of state is given as

$$P^\star = \frac{R^\star T^\star}{\vartheta^\star - b^\star} - \frac{a^\star}{\vartheta^{\star 2}}, \tag{3.4}$$

where P is the pressure, T is the temperature, ϑ is the specific volume and the superscript $\star$ is used to denote dimensional quantities. The constants $a^\star$ and $b^\star$ are determined by the critical properties of the real gas. These constants are given as

$$a^\star = 3P_c^\star \left(V_c^{\star 2}\right); b^\star = V_c^\star/3, \tag{3.5}$$

where $P_c^\star$ is the critical pressure and $V_c^\star$ is the critical volume of the gas.

3.3.1 Departure function for internal energy

In order to calculate thermodynamic properties from a real gas equation, the departure function for that property with respect to the chosen equation of state has to be evaluated. The departure function for any thermodynamic property of a real gas is defined as the difference in the value of that property determined from the chosen real gas equation of state and the value of the same property for an ideal gas under the same conditions of temperature and pressure. Mathematically, it can be expressed as follows.

$$X^R(T,P) = X(T,P) - X_{ig}(T,P), \tag{3.6}$$

where $X(T,P)$ is a thermodynamic property of the real gas at temperature (T) and pressure (P), $X_{ig}(T,P)$ is the same property for the ideal gas (IG) and $X^R(T,P)$ is the departure

function under the same conditions of temperature and pressure. For the compressible Navier-Stokes solver, the energy equation calculates the total energy. The kinetic energy is then subtracted from the total energy to determine the internal energy. The departure function for the van der Waals equation of state is given as follows.

The residual internal energy (e^R) is given as:

$$e^R = e^\star - e^\star_{ig} = \int_\infty^{\vartheta^\star} \left(T^\star \left(\frac{\partial S^\star}{\partial \vartheta^\star} \right)_{T^\star} - P^\star \right) d\vartheta^\star, \tag{3.7}$$

where $e^\star$ is the internal energy of the real gas and $e^\star_{ig}$ is the internal energy of the ideal gas under the same conditions of temperature and pressure. Using Maxwell's relations, we get: $(\partial S^\star/\partial \vartheta^\star)_{T^\star} = (\partial P^\star/\partial T^\star)_{\vartheta^\star}$, where $S^\star$ is the entropy. Substituting in the integral, $e^R = \int_\infty^{\vartheta^\star} \left(T^\star \left(\partial P^\star/\partial T^\star \right)_{\vartheta^\star} - P^\star \right) d\vartheta^\star$. Furthermore, from the van der Waals equation: $(\partial P^\star/\partial T^\star)_{\vartheta^\star} = R/(\vartheta^\star - b^\star)$. The expression for the residual internal energy is thereby given as: $U^R = \int_\infty^{\vartheta^\star} \left(a^\star/\vartheta^{\star 2} \right) d\vartheta^\star$. This has also been given in the works published by previous authors, such as Poling *et al.* (2001); Elliott & Lira (1999). Thus, we get

$$e^\star - C_{\vartheta^\star} T^\star = -\frac{a^\star}{\vartheta^\star}; e^\star = C_{\vartheta^\star} T^\star - a^\star \rho^\star, \tag{3.8}$$

where $C_{\vartheta^\star}$ is the heat capacity of the gas at constant volume.

The enthalpy is related to internal energy as: $h^0 = e^\star + P^\star/\rho^\star$. The heat capacity at constant pressure is given as $C_{P^\star} = \left(\partial h^0/\partial T^\star \right)_{P^\star}$.

3.3.2 Calculation of the speed of sound

The speed of sound from cubic equations of state can be calculated in accordance with the methodology as mentioned below. For polytropic van der Waal fluids, the calculation of thermodynamic properties, such as, internal energy and speed of sound from the fundamental variables temperature and density depends primarily on the dimensionless reciprocal specific heat at constant volume (β), which is given by $\beta = R^\star/C_{\vartheta^\star}$. The value of β is related to the number of active degrees of freedom of a molecule given by N. This takes into account the translational, rotational and vibrational degrees of freedom of a molecule. It should be noted that under certain conditions of temperature and pressure, all the vibrational degrees of a molecule may not be activated. This can lead to N attaining fractional values for different fluids. Moreover, two different molecules having similar molecular weights may have different values of N due to differing levels of molecular complexity. According to the law of equipartition of energy, the internal energy of a molecule is equally distributed among all the active degrees of freedom. Due to this, the isochoric specific heat is expressed as $C_{\vartheta^\star} = (N/2) R^\star$, where $R^\star$ is the molar gas constant per unit mass of the gas molecule. Thus, according to the definition of β, it can be expressed as $\beta = 2/N$. For CO_2, N is equal to 7.0.

The expression for pressure given in the van der Waals equation of state, as mentioned in equation 3.4 can be split up into the sum of the ideal, repulsive and attractive components in the following manner

$$P^\star = \frac{R^\star T^\star}{\vartheta^\star} + \frac{b^\star R^\star T^\star}{\vartheta^\star\left(\vartheta^\star - b^\star\right)} - \frac{a^\star}{\vartheta^2}. \tag{3.9}$$

The speed of sound is defined as

$$c^2\left(s^\star, \vartheta^\star\right) = -\vartheta^{\star 2}\left(\frac{\partial P^\star}{\partial \vartheta^\star}\right)_{s^\star}. \tag{3.10}$$

It can be defined as the sum of the following contributions

$$c^2 = c^2_{ideal} + \delta c^2_{rep} + \delta c^2_{att}. \tag{3.11}$$

The sum of the contributions from the ideal and the repulsive components is obtained by applying the above formula to the sum of the ideal and the repulsive components in the van der Waals equation. The result is given as

$$c^2_{ideal} + \delta c^2_{rep} = \left(1 + \frac{2}{N}\right) R^\star T^\star \left(\frac{\vartheta^\star}{\vartheta^\star - b^\star}\right)^2. \tag{3.12}$$

The contribution of the attractive component is given by

$$\delta c^2_{att} = -\vartheta^{\star 2}\left(\frac{\partial\left(-\frac{a^\star}{\vartheta^2}\right)}{\partial \vartheta^\star}\right)_{T^\star} = -\frac{2a^\star}{\vartheta^*}. \tag{3.13}$$

The ideal and repulsive components are reduced with increasing molecular complexity as they are connected to the internal energy of the translational modes. With increasing molecular complexity, an increasing number of vibrational modes are available to store the energy at the expense of the translational modes. This is the reason that the contributions from the ideal and the repulsive components are multiplied by the factor $(1 + 2/N)$ which reduces with increasing molecular complexity, whereas it is not so for the attractive component. The final expression for the speed of sound of a van der Waals gas is therefore given by

$$c^2\left(T^\star, \vartheta^\star\right)_{VdW} = \left(1 + \frac{2}{N}\right) R^\star T^\star \left(\frac{\vartheta^\star}{\vartheta^\star - b^\star}\right)^2 - \frac{2a^\star}{\vartheta^\star}. \tag{3.14}$$

3.3.3 Calculation of isoenthalpic compressibility

For an ideal gas, the isothermal compressibility is expressed as

$$\Psi_{T^\star} = \left(\frac{\partial \rho^\star}{\partial P^\star}\right)_{T^\star}. \tag{3.15}$$

This definition is only applicable for ideal gases. For real gases, the compressibility has to be evaluated at isoenthalpic conditions, and is given as

$$\Psi_{H^0} = \left(\frac{\partial \rho^\star}{\partial P^\star}\right)_{H^0} = -\frac{1}{\vartheta^{\star 2}}\left(\frac{\partial \vartheta^\star}{\partial P^\star}\right)_{H^0} = \frac{1}{\vartheta^{\star 2}}\frac{\left(\frac{\partial H^0}{\partial P^\star}\right)_{\vartheta^\star}}{\left(\frac{\partial H^0}{\partial \vartheta^\star}\right)_{P^\star}}. \tag{3.16}$$

This can be calculated for real gases using the various real gas equations of state. For the van der Waals equation of state,

$$H^0 = C_{\vartheta^\star} T^\star + P^\star \vartheta^\star - \left(a^\star / \vartheta^\star\right). \tag{3.17}$$

Now, from the chain rule, we know that

$$\begin{aligned} \left(\partial \vartheta^\star / \partial P^\star\right)_{H^0} &= -\left(\partial H^0 / \partial P^\star\right)_{\vartheta^\star} / \left(\partial H^0 / \partial \vartheta^\star\right)_{P^\star}, \\ \left(\partial H^0 / \partial P^\star\right)_{\vartheta^\star} &= \left(\partial H^0 / \partial T^\star\right)_{\vartheta^\star} \left(\partial T^\star / \partial P^\star\right)_{\vartheta^\star}. \end{aligned} \tag{3.18}$$

Combining the previous equation with the departure function for enthalpy, we get that the partial derivative of enthalpy with respect to pressure at constant volume is given by

$$\left(\partial H^0 / \partial P^\star\right)_{\vartheta^\star} = \vartheta^\star + C_{\vartheta^\star} / \left(\partial P^\star / \partial T^\star\right)_{\vartheta^\star} \tag{3.19}$$

and the partial derivative of enthalpy with respect to volume at constant pressure is

$$\left(\partial H^{\star 0} / \partial \vartheta^\star\right)_{P^\star} = C_{\vartheta^\star} / \left(\partial \vartheta^\star / \partial T^\star\right)_{P^\star} + P^\star + \left(a^\star / \vartheta^{\star 2}\right). \tag{3.20}$$

The other required derivatives, such as the partial derivatives of pressure with respect to temperature and volume are given as

$$\left(\frac{\partial P^\star}{\partial T^\star}\right)_{\vartheta^\star} = \frac{R^\star}{\vartheta^\star - b^\star}, \left(\frac{\partial P^\star}{\partial \vartheta^\star}\right)_{T^\star} = -\frac{R^\star T^\star}{\left(\vartheta^\star - b^\star\right)^2} + \frac{2a^\star}{\vartheta^{\star 3}}, \tag{3.21}$$

$$\left(\frac{\partial \vartheta^\star}{\partial T^\star}\right)_{P^\star} = -\frac{\left(\frac{\partial P^\star}{\partial T^\star}\right)_{\vartheta^\star}}{\left(\frac{\partial P^\star}{\partial \vartheta^\star}\right)_{T^\star}}. \tag{3.22}$$

3.4 Redlich Kwong equation of state

The non-dimensional Redlich Kwong (RK) equation of state is given as

$$P^\star = \frac{R^\star T^\star}{\vartheta^\star - b^\star} - \frac{a^\star \alpha}{\left(\vartheta^\star\right)\left(\vartheta^\star + b^\star\right)}. \tag{3.23}$$

The dimensional constants $a^\star$ and $b^\star$ are evaluated from the critical properties of the fluid as $a^\star = \left(0.42748 R^{\star 2} T_c^{\star 2.5}\right) / \left(P_c\right)$ and $b^\star = \left(0.08662 R^\star T_c^\star\right) / \left(P_c^\star\right)$. The parameter α is given as: $\alpha = 1 / \sqrt{T^\star}$.

3.4.1 Departure function for internal energy

For this equation of state, following the same procedure as mentioned above for the van der Waals equation of state, we get,

$$T^\star \left(\frac{\partial P^\star}{\partial T^\star}\right)_{\vartheta^\star} - P^\star = \frac{a^\star \left(\alpha - T^\star \frac{d\alpha}{dT^\star}\right)}{(\vartheta^\star)(\vartheta^\star + b^\star)}. \tag{3.24}$$

So, the residual internal energy is calculated as

$$e^R = \int_{\infty}^{\vartheta^\star} \left(T^\star \left(\frac{\partial P^\star}{\partial T^\star}\right)_{\vartheta^\star} - P^\star\right) = \frac{a^\star \left(\alpha - T^\star \frac{d\alpha}{dT^\star}\right)}{b^\star} ln \frac{\vartheta^\star}{\vartheta^\star + b^\star}. \tag{3.25}$$

Substituting the value of α

$$e^\star = C_{\vartheta^\star} T^\star + \frac{3}{2} \frac{a^\star}{b^\star \sqrt{T^\star}} ln \frac{1}{1 + b^\star \rho}. \tag{3.26}$$

3.4.2 Calculation of the speed of sound

Following a similar methodology to that mentioned above for the van der Waals equation of state, the speed of sound from the Redlich Kwong equation of state is calculated from the following formula

$$c_{RK}^2 = \vartheta^{\star 2} \left(\frac{T^\star}{C_v} \left(\frac{\partial P^\star}{\partial T^\star}\right)_{\vartheta^\star}^2 - \left(\frac{\partial P^\star}{\partial \vartheta^\star}\right)_{T^\star}\right). \tag{3.27}$$

Thus, it is seen that the speed of sound is a function of the partial derivative of pressure with respect to temperature at constant volume and the partial derivative of pressure with respect to volume at constant temperature. These partial derivatives are given by

$$\left(\frac{\partial P^\star}{\partial T^\star}\right)_{\vartheta^\star} = \frac{R^\star}{\vartheta^\star - b^\star} - \frac{a^\star \left(d\alpha^\star / dT^\star\right)}{(v^\star)(\vartheta^\star + b^\star)}, \tag{3.28}$$

$$\left(\frac{\partial P^\star}{\partial \vartheta^\star}\right)_{T^\star} = -\left(\frac{R^\star T^\star}{\vartheta^\star - b^\star}\right)^2 + \frac{a^\star \alpha^\star \left(2\vartheta^\star + b^\star\right)}{\left(\vartheta^\star \left(\vartheta^\star + b^\star\right)\right)^2}. \tag{3.29}$$

The speed of sound can be calculated by substituting these derivatives into the formula for speed of sound given above.

3.4.3 Calculation of isoenthalpic compressibility

For the Redlich Kwong equation of state, the pressure ($P^\star$) and the enthalpy ($H^\star$) are given by the following equations

$$\begin{aligned} P^\star &= R^\star T^\star / \left(\vartheta^\star - b^\star\right) - a^\star \alpha / \left(\left(\vartheta^\star\right)\left(\vartheta^\star + b^\star\right)\right), \\ H^0 &= C_{\vartheta^\star} T^\star + P^\star \vartheta^\star + \left(3a^\star \alpha\right) / \left(2b^\star\right) ln \left(\vartheta^\star / \left(\vartheta^\star + b^\star\right)\right) \end{aligned} \tag{3.30}$$

as a functions of the volume ($\vartheta^\star$) and temperature ($T^\star$).

Following the chain rule of calculus,

$$\begin{aligned}\left(\partial\vartheta^\star/\partial P^\star\right)_{H^0} &= -\left(\partial H^0/\partial P^\star\right)_{\vartheta^\star} / \left(\partial H^0/\partial\vartheta^\star\right)_{P^\star},\\ \left(\partial H^0/\partial P^\star\right)_{\vartheta^\star} &= \left(\partial H^0/\partial T^\star\right)_{\vartheta^\star}\left(\partial T^\star/\partial P^\star\right)_{\vartheta^\star},\\ \left(\partial H^0/\partial\vartheta^\star\right)_{P^\star} &= \left(\partial H^0/\partial T^\star\right)_{P^\star}\left(\partial T^\star/\partial\vartheta^\star\right)_{P^\star}.\end{aligned} \tag{3.31}$$

Combining these with the departure function for enthalpy, we get,

$$\left(\frac{\partial H^0}{\partial P^\star}\right)_{\vartheta^\star} = \frac{C_{\vartheta^\star}}{\left(\frac{\partial P^\star}{\partial T^\star}\right)_{\vartheta^\star}} + \vartheta^\star + \frac{3}{2}\frac{a^\star}{b^\star}\frac{\left(\frac{\partial\alpha}{\partial T^\star}\right)}{\left(\frac{\partial P^\star}{\partial T^\star}\right)_{\vartheta^\star}} ln\left(\frac{\vartheta^\star}{\vartheta^\star + b^\star}\right). \tag{3.32}$$

$$\left(\frac{\partial H^0}{\partial\vartheta^\star}\right)_{P^\star} = \frac{C_{\vartheta^\star}}{\left(\frac{\partial\vartheta^\star}{\partial T^\star}\right)_{P^\star}} + P^\star + \frac{3}{2}\frac{a^\star\alpha}{b^\star}\left(\frac{1}{\vartheta^\star} - \frac{1}{(\vartheta^\star + b^\star)}\right) + \frac{3a^\star\frac{\partial\alpha}{\partial T^\star}}{2b^\star\left(\frac{\partial\vartheta^\star}{\partial T^\star}\right)_{P^\star}} ln\left(\frac{\vartheta^\star}{\vartheta^\star + b^\star}\right) \tag{3.33}$$

The other required derivatives are given as

$$\left(\frac{\partial\vartheta^\star}{\partial T^\star}\right)_{P^\star} = -\frac{\left(\frac{\partial P^\star}{\partial T^\star}\right)_{\vartheta^\star}}{\left(\frac{\partial P^\star}{\partial\vartheta^\star}\right)_{T^\star}}, \left(\frac{\partial P^\star}{\partial T^\star}\right)_{\vartheta^\star} = \frac{R^\star}{\vartheta^\star - b^\star} - \frac{a^\star\frac{\partial\alpha}{\partial T^\star}}{\vartheta^\star(\vartheta^\star + b^\star)}, \tag{3.34}$$

$$\left(\frac{\partial P^\star}{\partial\vartheta^\star}\right)_{T^\star} = -\frac{R^\star T^\star}{(\vartheta^\star - b^\star)^2} + \frac{a^\star\alpha}{b^\star}\left(\frac{1}{\vartheta^{\star 2}} - \frac{1}{(\vartheta^\star + b^\star)^2}\right). \tag{3.35}$$

3.5 Peng Robinson equation of state

The Peng Robinson equation of state is given as

$$P^\star = \frac{R^\star T^\star}{\vartheta^\star - b^\star} - \frac{a^\star\alpha}{\vartheta^{\star 2} + 2b\vartheta^\star - b^{\star 2}}. \tag{3.36}$$

3.5.1 Departure function for internal energy

The residual internal energy (e^R) is given by the following equation.

$$e^R = e - e^{ig} = \int_\infty^{\vartheta^\star}\left(T^\star\left(\frac{\partial S^\star}{\partial\vartheta^\star}\right)_{T^\star} - P^\star\right)d\vartheta^\star, \tag{3.37}$$

where $S^\star$ is the entropy. Using Maxwell's relations, we get

$$\left(\partial S^\star/\partial\vartheta^\star\right)_{T^\star} = \left(\partial P^\star/\partial T^\star\right)_{\vartheta^\star}. \tag{3.38}$$

Integrating, we have

$$U^R = \int_{\infty}^{\vartheta^\star} \left(T^\star \left(\partial P^\star / \partial T^\star \right)_{\vartheta^\star} - P^\star \right) d\vartheta^\star. \tag{3.39}$$

Substituting the value of pressure P from the Peng Robinson equation,

$$T^\star \left(\frac{\partial P^\star}{\partial T^\star} \right)_{\vartheta^\star} - P^\star = \frac{a^\star \left(\alpha - T^\star \frac{d\alpha}{dT^\star} \right)}{\left(\vartheta^\star + b^\star + \sqrt{2} b^\star \right) \left(\vartheta^\star + b^\star - \sqrt{2} b^\star \right)}, \tag{3.40}$$

$$T^\star \left(\frac{\partial P^\star}{\partial T^\star} \right)_{\vartheta^\star} - P^\star = \frac{a^\star \left(\alpha - T^\star \frac{d\alpha}{dT^\star} \right)}{2\sqrt{2} b^\star} \left[\frac{1}{\left(\vartheta^\star + b^\star - \sqrt{2} b^\star \right)} - \frac{1}{\left(\vartheta^\star + b^\star + \sqrt{2} b^\star \right)} \right]. \tag{3.41}$$

The departure function for internal energy e for the Peng Robinson equation is thus given as

$$e^R = \int_{\infty}^{\vartheta^\star} \left[T^\star \left(\frac{\partial P^\star}{\partial T^\star} \right)_{\vartheta^\star} - P^\star \right] d\vartheta^\star, \tag{3.42}$$

$$e^\star = C_{\vartheta^\star} T^\star + \frac{a^\star \left(\alpha - T^\star \frac{d\alpha}{dT^\star} \right)}{2\sqrt{2} b^\star} ln \frac{\left(1 + b^\star \left(1 - \sqrt{2} \right) \rho^\star \right)}{\left(1 + b^\star \left(1 + \sqrt{2} \right) \rho^\star \right)}. \tag{3.43}$$

3.5.2 Calculation of the speed of sound

Following a similar method as to that mentioned above for the van der Waals and the Redlich Kwong equation of state, the formula is derived as

$$c_{PR}^2 = \vartheta^{\star 2} \left(\frac{T^\star}{C_v} \left(\frac{\partial P^\star}{\partial T^\star} \right)_{\vartheta^\star}^2 - \left(\frac{\partial P^\star}{\partial \vartheta^\star} \right)_{T^\star} \right). \tag{3.44}$$

The partial derivatives in the above equation are given as

$$\left(\frac{\partial P^\star}{\partial T^\star} \right)_{\vartheta^\star} = \frac{R^\star}{\vartheta^\star - b^\star} - \frac{a^\star \left(d\alpha^\star / dT^\star \right)}{\vartheta^{\star 2} + 2 b^\star \vartheta^\star - b^{\star 2}}, \tag{3.45}$$

$$\left(\frac{\partial P^\star}{\partial \vartheta^\star} \right)_{T^\star} = - \left(\frac{R^\star T^\star}{\vartheta^\star - b^\star} \right)^2 + \frac{2 a^\star \alpha^\star \left(\vartheta^\star + b^\star \right)}{\left(\vartheta^{\star 2} + 2 b^\star \vartheta^\star - b^{\star 2} \right)^2}. \tag{3.46}$$

3.5.3 Calculation of the isoenthalpic compressibility

For the Peng Robinson equation of state, enthalpy is given by

$$H^0 = C_{\vartheta^\star} T^\star + P^\star \vartheta^\star + a^\star \frac{(\alpha - T^\star (\partial\alpha/\partial T^\star))}{\left(2\sqrt{2} b^\star\right)} ln\left(\frac{\vartheta^\star + b^\star\left(1 - \sqrt{2}\right)}{\vartheta^\star + b^\star\left(1 + \sqrt{2}\right)}\right). \tag{3.47}$$

Now, from the chain rule, we know that,

$$\begin{aligned} \left(\partial\vartheta^\star/\partial P^\star\right)_{H^0} &= -\left(\partial H^0/\partial P^\star\right)_{\vartheta^\star} / \left(\partial H^0/\partial\vartheta^\star\right)_{P^\star}, \\ \left(\partial H^0/\partial P^\star\right)_{\vartheta^\star} &= \left(\partial H^0/\partial T^\star\right)_{\vartheta^\star} \left(\partial T^\star/\partial P^\star\right)_{\vartheta^\star}. \end{aligned} \tag{3.48}$$

Combining this with the departure function for enthalpy, we get

$$\left(\frac{\partial H^0}{\partial P^\star}\right)_{\vartheta^\star} = \frac{C_{\vartheta^\star}}{\left(\frac{\partial P^\star}{\partial T^\star}\right)_{\vartheta^\star}} + \vartheta^\star - \frac{a^\star T^\star \frac{\partial^2\alpha}{\partial T^{\star 2}}}{2\sqrt{2} b^\star \left(\frac{\partial P^\star}{\partial T^\star}\right)_{\vartheta^\star}} ln\left(\frac{\vartheta^\star + b^\star\left(1 - \sqrt{2}\right)}{\vartheta^\star + b^\star\left(1 + \sqrt{2}\right)}\right), \tag{3.49}$$

$$\begin{aligned} \left(\frac{\partial H^0}{\partial\vartheta^\star}\right)_{P^\star} = \frac{C_{\vartheta^\star}}{\left(\frac{\partial\vartheta^\star}{\partial T^\star}\right)_{P^\star}} + P^\star - \frac{a^\star T^\star \frac{\partial^2\alpha}{\partial T^{\star 2}}}{2\sqrt{2} b^\star \left(\frac{\partial\vartheta^\star}{\partial T^\star}\right)_{P^\star}} ln\left(\frac{\vartheta^\star + b^\star\left(1 - \sqrt{2}\right)}{\vartheta^\star + b^\star\left(1 + \sqrt{2}\right)}\right) \\ + \frac{a^\star\left(\alpha - T^\star \frac{\partial\alpha}{\partial T^\star}\right)}{2\sqrt{2} b^\star}\left(\frac{1}{\vartheta^\star + b^\star\left(1 - \sqrt{2}\right)} - \frac{1}{\vartheta^\star + b^\star\left(1 + \sqrt{2}\right)}\right). \end{aligned} \tag{3.50}$$

The other derivatives are given as

$$\left(\frac{\partial\vartheta^\star}{\partial T^\star}\right)_{P^\star} = -\frac{\left(\frac{\partial P^\star}{\partial T^\star}\right)_{\vartheta^\star}}{\left(\frac{\partial P^\star}{\partial\vartheta^\star}\right)_{T^\star}}, \tag{3.51}$$

$$\left(\frac{\partial P^\star}{\partial T^\star}\right)_{\vartheta^\star} = \frac{R^\star}{\vartheta^\star - b^\star} - \frac{a^\star \frac{\partial\alpha}{\partial T}}{\vartheta^{\star 2} + 2b^\star\vartheta^\star - b^{\star 2}}, \tag{3.52}$$

$$\left(\frac{\partial P^\star}{\partial\vartheta^\star}\right)_{T^\star} = -\frac{R^\star T^\star}{\left(\vartheta^\star - b^\star\right)^2} + \frac{2a^\star\alpha\left(\vartheta^\star + b^\star\right)}{\left(\vartheta^{\star 2} + 2b^\star\vartheta^\star - b^{\star 2}\right)^2}. \tag{3.53}$$

3.6 Comparison of thermodynamic properties from different cubic equations of state

The plots in figures 3.1(c) and 3.1(d) show the density and the heat capacity at constant pressure (C_p) for supercritical CO_2 at 80 bar as a function of temperature. Additionally, the plots in figures 3.1(a) and 3.1(b) show the speed of sound and the isothermal compressibility of CO_2 determined by the different cubic equations of state at 80 bar as a

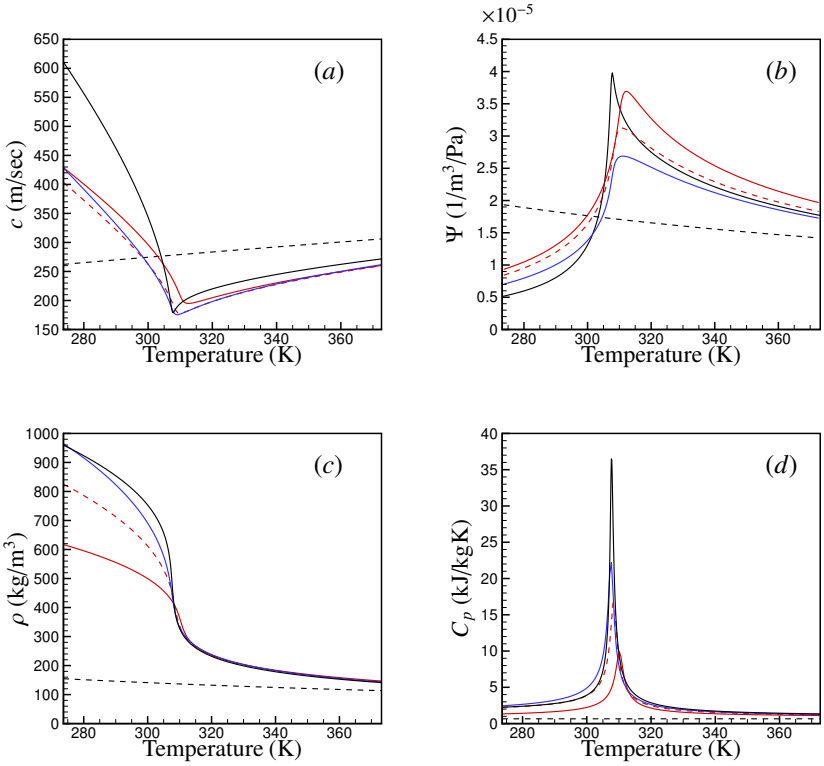

Figure 3.1: Speed of sound, isoenthalpic compressibility, density and heat capacity as a function of temperature for supercritical CO_2 at 80 bar for different cubic equations of state compared to that from the Refprop library (Lemmon *et al.* (2010)). (– – –) IG, (——) VdW, (– – –) RK, (——) PR, (——) Refprop

function of temperature. From these figures, it is clearly established that the Peng Robinson equation of state represents the actual properties obtained from the Refprop library far more accurately than the other cubic equations of state, such as van der Waals equation and the Redlich Kwong equation of state. Hence, the Peng Robinson equation is chosen to calculate the thermodynamic properties in the Navier-Stokes solver.

The constants in the Peng Robinson equation of state are non-dimensionalized with respect to the reference properties of supercritical CO_2 at 80 bar and 300 K, denoted by the subscript 0. This is given as follows.

$$R = \frac{R^\star T_0^\star}{U_0^{\star 2}}, a = \frac{a^\star \rho_0^\star}{U_0^{\star 2}}, b = b^\star \rho_0^\star. \tag{3.54}$$

3.7 Implementation of the departure function for the Peng Robinson equation of state

The non-dimensionalized departure function for the Peng Robinson equation of state is given as

$$U = \frac{RT_rT_c}{\gamma - 1} + \frac{(1+K)\left(1+K\left(1-T_r^{0.5}\right)\right)a}{2\sqrt{2}b} ln\left(\frac{1+b\left(1-\sqrt{2}\right)\rho}{1+b\left(1+\sqrt{2}\right)\rho}\right), \tag{3.55}$$

where $\gamma = R/C_\vartheta + 1$ and $T_r = T/T_c$ is the reduced non-dimensional temperature. It is evident that the equation above is quadratic in $\sqrt{T_r}$. It can be represented as

$$A\sqrt{T_r}^2 + B\sqrt{T_r} + C = 0, \tag{3.56}$$

where A,B and C are given as follows.

$$A = \frac{RT_c}{\gamma - 1}, \tag{3.57}$$

$$B = -\frac{K(1+K)a}{2\sqrt{2}b} ln\left(\frac{1+b\left(1-\sqrt{2}\right)\rho}{1+b\left(1+\sqrt{2}\right)\rho}\right), \tag{3.58}$$

$$C = \frac{(1+K)^2 a}{2\sqrt{2}b} ln\left(\frac{1+b\left(1-\sqrt{2}\right)\rho}{1+b\left(1+\sqrt{2}\right)\rho}\right) - U. \tag{3.59}$$

The analytical formula for finding the roots of a quadratic equation is used to determine the roots. Two positive roots are not possible for this equation as it is thermodynamically not possible to have the same internal energy for a gas at a particular density and two different temperatures. Therefore, one of the roots is positive and the other is negative. The negative root is frivolous and is neglected. We can thus arrive at a unique solution for the temperature. The temperature and density are substituted back into equation 3.36 to calculate the pressure. This methodology is adopted to avoid iterations with a Newton-Raphson solver and to arrive at the solution in a computationally efficient manner.

4

Direct Numerical Simulations of fully compressible turbulent flows of supercritical carbon dioxide near the vapour-liquid critical point

Part of the contents of this chapter appeared in:

Fully compressible low-Mach number simulations of carbon dioxide at supercritical pressures and trans-critical temperatures. Sengupta U., Nemati, H., Boersma, B.J. & Pecnik, R. *Flow, Turbulence and Combustion*, (2017)

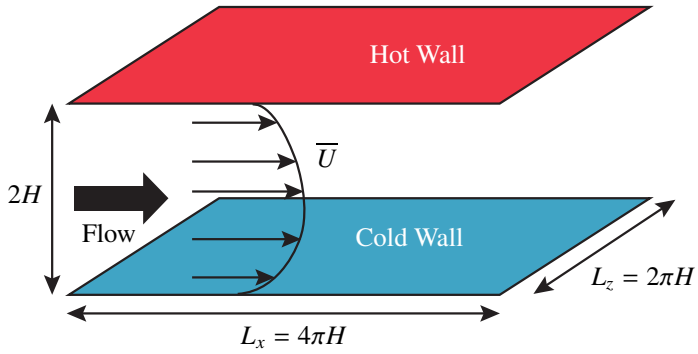

Figure 4.1: Flow geometry for fully developed turbulent channel flow with wall temperature difference

4.1 Introduction

4.2 Details of simulated cases

The computational domain for the fully developed flow in the channel geometry is as follows: streamwise length $L_x = 4\pi H$, spanwise length $L_z = 2\pi H$ and wall normal height $L_y = 2H$, where H is the half channel height. This has been shown in figure 4.1. The number of grid points used is $720 \times 720 \times 360$ in the streamwise, spanwise and wall-normal directions, respectively. For all the simulated cases, walls have isothermal wall boundary conditions. The lower wall is the cold wall and the upper wall is the hot wall. The turbulent channel flow geometry is given in Figure 4.1. The channel is periodic in the streamwise and spanwise directions. In these directions, the mesh is uniform and pseudo spectral methods are used to calculate the derivatives using the Fast Fourier Transform (FFT) library. In order to minimize aliasing errors, the derivatives for the advective terms in the periodic directions are calculated using the quasi skew-symmetric method developed by Morinishi (2010). In the wall-normal direction, the mesh is fully collocated and a finite difference scheme is used in which the derivatives for the advective and the diffusive terms are obtained by interpolating the quantities to the cell faces and then differentiating to obtain the values of the derivatives at the cell center. The time integration is performed using an explicit third order Runge Kutta method as given by Gottlieb & Shu (1998). A hyperbolic tangent function is used to obtain a non-uniform mesh in the wall-normal direction. The domain is parallelized using 2DECOMP&FFT library with 2D pencil decomposition.

The details of the simulations performed are given in Table 4.1. All the simulations are performed at a bulk Reynolds Number of 2800 based on the reference density (ρ_0), reference viscosity (μ_0), bulk velocity (U_b) and half channel height (H). The reference Prandtl Number is 3.019. The first four cases mentioned in Table 4.1 have variable transport properties tabulated from Refprop. The first and the third case have a low Mach

Case	T_{wc}, T_{wh}	Transport properties (μ,κ)	$Re_{\tau wc}$	$Re_{\tau wh}$	Ma
LSC_1	300 K, 315 K	Tabulated Refprop data	218.18	310.12	0.2
HSC_1	300 K, 315 K	Tabulated Refprop data	215.48	313.30	0.5
LSC_2	306 K, 321 K	Tabulated Refprop data	343.63	438.52	0.2
HSC_2	306 K, 321 K	Tabulated Refprop data	345.07	427.47	0.4
SCCTP	300 K, 315 K	Constant	126.41	224.46	0.2

Table 4.1: Details of the simulations performed using supercritical CO_2, stating cold and hot wall temperatures, T_{wc}, T_{wh}, viscosity and thermal conductivity, μ, κ, and resulting friction Reynolds number at both walls.

number of 0.2 and are referred to as LSC_1 and LSC_2, respectively. The second and the fourth cases are at higher Mach numbers and are referred to as HSC_1 and HSC_2, respectively. The final case has constant viscosity and thermal conductivity calculated at the reference conditions and is called the supercritical constant transport property (SCCTP) case. The cases LSC_1 and SCCTP have isothermal wall boundary conditions with temperatures 300 K and 315 K at the two walls. For the case LSC_2, the wall temperatures are 306 K and 321 K. At a pressure of 80 bar, the pseudo-critical temperature of CO_2 is around 307.5 K, which is 1.025 times the reference temperature of 300 K. Thus, the cases LSC_1 and SCCTP have the trans-critical transition roughly in the middle of the channel whereas, the case LSC_2 has trans-critical transition close to the cold wall. The higher Mach number cases HSC_1 and HSC_2 have the same isothermal wall boundary conditions as the cases LSC_1 and LSC_2, respectively. For the higher Mach number cases HSC_1 and HSC_2, the pressure fluctuations increase in comparison to the lower Mach number cases. This is because pressure fluctuations in turbulent flows increase with the increase in Mach number. For the case HSC_1, it is found that if the bulk pressure in the channel is maintained at 80 bar, which is the same as that for the lower Mach number cases, then some points in the channel have pressures lying within the two-phase region due to the increase in pressure fluctuations. In order to avoid this, the bulk pressure for HSC_1 is increased to 83 bar. Then, it is seen that, in spite of the increase in pressure fluctuations, all points in the channel have pressures above the critical pressure and hence fall outside the two phase region.

The code has been validated for fully developed turbulent flows of an ideal gas with the data published by Kim *et al.* (1987); Coleman *et al.* (1995). This is shown in Appendix A.

The Reynolds and Favre averages denote the averaging of a physical quantity X with regard to time and density, respectively. They are expressed respectively as $\overline{X}$ and $\widetilde{X}$. The corresponding fluctuations are given as X' and X'', respectively. This can be represented by the following relation

$$X = \overline{X} + X' = \widetilde{X} + X''. \tag{4.1}$$

Case	$(\Delta x/\eta)_{max}$	$(\Delta y_{min}/\eta)_{max}$	$(\Delta z/\eta)_{max}$
LSC_1	3.60	0.62	1.80
HSC_1	3.62	0.63	1.81
LSC_2	5.00	0.81	2.50
HSC_2	5.20	0.89	2.60
SCCTP	2.50	0.12	1.25

Table 4.2: Spatial resolution with respect to the Kolmogorov scales (η); $\Delta x, \Delta y, \Delta z$: grid spacings in streamwise, wall-normal and spanwise directions, respectively.

Some other important properties of Reynolds and Favre averages are given as follows

$$\begin{aligned} \overline{X'} &= 0, \\ \widetilde{X} &= \frac{1}{\overline{\rho}}\overline{\rho X}, \\ \overline{\rho X''} &= 0, \\ \overline{X''} = -\frac{1}{\overline{\rho}}\overline{\rho' X'} &= \overline{X} - \widetilde{X}, \\ X'' &= X' + \overline{X''}, \\ \overline{X'Y'} = \overline{X'Y''} &= \overline{X''Y'}. \end{aligned} \tag{4.2}$$

These relations have been mentioned by previous authors, such as Gerolymos & Vallet (2014); Huang *et al.* (1995).

The mesh resolution is expressed in terms of the Kolmogorov and the Batchelor scales. The Kolmogorov length scales, which indicate the resolution of the momentum scales are defined as $\eta = \left((\overline{\mu}/\overline{\rho})^3 \overline{\rho}/\epsilon\right)^{0.25}$. Here, μ, ρ and ϵ refer to the viscosity, density and the dissipation of turbulent kinetic energy obtained from the turbulent kinetic energy budgets of the simulations, respectively. As the Prandtl number in supercritical fluids is more than unity, the mesh resolution in terms of the Batchelor scales is also important as the Batchelor scales indicate the resolution of the thermal scales. The Batchelor scales are defined as: $\eta_B = \eta/\sqrt{Pr}$, where Pr refers to the Prandtl number determined by the local mean properties. The mesh resolution in terms of the Kolmogorov and the Batchelor scales are given in Table 4.2 and Table 4.3, respectively. The maximum mesh resolution in terms of the Kolmogorov length scales are within the limits $\Delta y < 2\eta$, $\Delta z < 6\eta$ and $\Delta x < 12\eta$, as specified by previous authors Zonta *et al.* (2012); Lee *et al.* (2013).

DNS data is extracted after convergence and time averaging is done using data for 10 flow through times at an interval of 2000 time steps for each of the cases mentioned above. The time step chosen is given by $\Delta t = 10^{-4}$ for the lower Mach number cases LSC_1, LSC_2 and SCCTP and $\Delta t = 5 \times 10^{-3}$ for the higher Mach number cases HSC_1 and HSC_2.

Case	$(\Delta x/\eta_B)_{max}$	$(\Delta y_{min}/\eta_B)_{max}$	$(\Delta z/\eta_B)_{max}$
LSC_1	5.30	0.96	2.65
HSC_1	5.33	0.98	2.66
LSC_2	14.40	2.52	7.20
HSC_2	14.9	2.77	7.45
SCCTP	4.40	0.25	2.20

Table 4.3: Spatial resolution with respect to the Batchelor scales (η_B); $\Delta x, \Delta y, \Delta z$: grid spacings in streamwise, wall-normal and spanwise directions, respectively.

4.3 Mean flow and turbulence statistics

The mean velocity profile of all the five cases are shown in Figure 4.2(a). In the constant viscosity case SCCTP, the velocity profile is almost symmetric. The velocity profile deviates from symmetry for the variable viscosity cases LSC_1, LSC_2, HSC_1 and HSC_2. This is due to the decrease in viscosity with the increase of temperature causing higher velocity gradients near the hot wall and lower velocity gradients near the cold wall. The same has been observed by Zonta *et al.* (2012) for incompressible flows.

The effects of different location of the trans-critical transition at low Mach numbers are evident on comparing the mean temperature, mean density and the density fluctuations for the cases LSC_1 and LSC_2. The mean temperature profiles for the cases LSC_1 and LSC_2 are presented in Figure 4.2(b). For the case LSC_1, the trans-critical transition occurs roughly near the middle of the channel which is therefore a region of high C_p. The temperature profile for LSC_1 is much flatter near the middle of the channel. However, for the LSC_2 case, the trans-critical transition occurs very close to the cold wall and the temperature in the bulk of the channel is much higher than T_{pc}. So, the portions of the channel away from the cold wall are a region of low C_p. Thus, for the LSC_2 case, the temperature changes more rapidly with channel height away from the cold wall. For the high Mach number case HSC_1, which has the same wall temperatures as LSC_1, the bulk temperature is seen to be higher than that for LSC_1. This is partially due to an increase in Mach number which increases the effects of viscous heating and also due to a rise in pressure to 83.5 bar which leads to a higher bulk temperature compared to LSC_1. In the case HSC_2, which has the same wall temperatures as LSC_2, the rise in Mach number to 0.4 only leads to a marginal increase in the bulk temperature at the same bulk pressure of 80 bar.

The mean density profiles for the cases LSC_1 and LSC_2 are given in Figure 4.3(a). It can be observed that the density changes by a factor of around 2.5 from the hot wall to the cold wall. For the case LSC_1, the density changes steeply near both walls with a flatter profile near the middle of the channel. But, for the case LSC_2, the trans-critical transition very near to the cold wall results in the steep decline of density profile close to the cold wall and an approximately flat profile thereafter. The same pattern is seen to be repeated

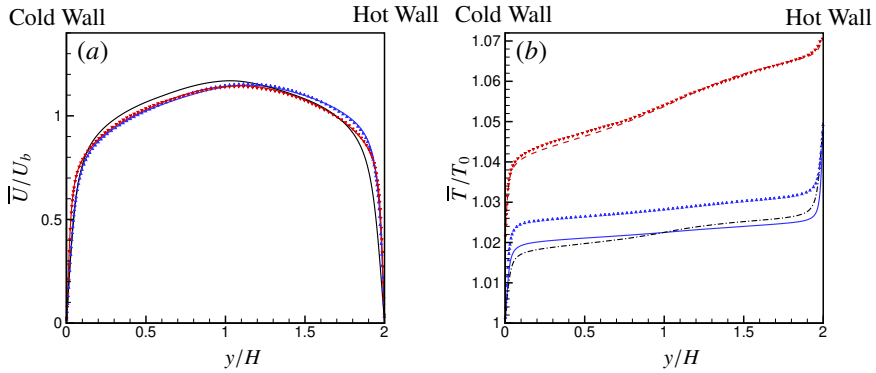

Figure 4.2: Mean velocity and mean temperature as a function of channel height for turbulent flows of supercritical CO_2. (a) Mean velocity; (b) Mean temperature; (——) LSC_1; (▲) HSC_1; (– – –) LSC_2; (▼) HSC_2; (— - —) SCCTP.

for the higher Mach number cases HSC_1 and HSC_2, which have trans-critical transition near the channel center and the cold wall, respectively.

By observing the root mean square (RMS) density fluctuation profiles for the cases LSC_1 and LSC_2 in Figure 4.3(b), it is evident that for LSC_1, the RMS density fluctuation exhibits two peaks near the walls and a smaller peak near the middle of the channel. This behaviour is analogous to the density fluctuation behaviour for turbulent ideal gas flows with wall temperature differences. This is however not the case for LSC_2 for which the RMS density fluctuation has a very high value close to the cold wall and a much smaller peak near the middle of the channel. The peak of the density fluctuation near the hot wall is eliminated. Due to the trans-critical transition near the cold wall, the temperature for most of the remaining channel height is higher than the pseudo-critical temperature. For temperatures far away from the pseudo-critical temperature, the change of density with change in temperature is minimal. Thus, the density profile is almost flat for locations away from the cold wall. This can be seen by observing the profiles of mean density in figure 4.3(a) for the case LSC_2. For the other cases, LSC_1 and SCCTP, the density has sharp gradients near both walls. Due to the absence of a significant gradient of mean density near the hot wall for LSC_2, the passive mixing across a mean gradient is minimal. This causes the peak of the density fluctuation near the hot wall to disappear for SC_2. Thus, trans-critical transition very close to the wall causes this unusual behaviour in the density fluctuations. The temperature and the RMS pressure fluctuations for the two cases are shown in figures 4.4(a) and 4.4(b), respectively. The case LSC_2 has higher temperature fluctuations and lower pressure fluctuations near the center of the channel compared to the other two cases.

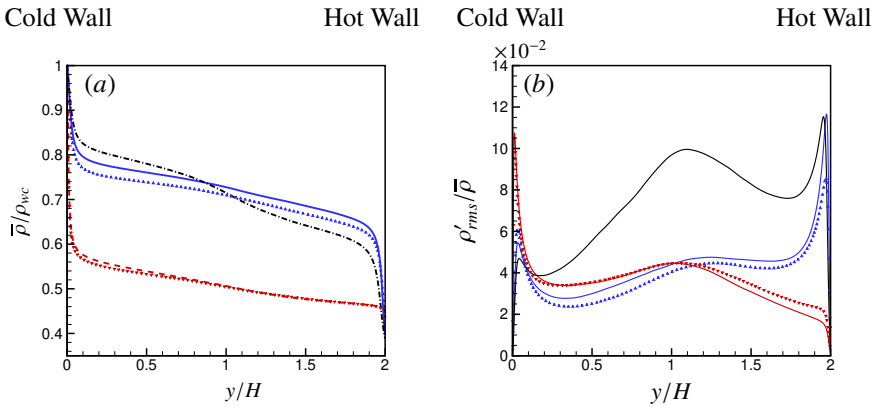

Figure 4.3: Mean Density and rms density fluctuations as a function of channel height for turbulent flows of supercritical CO_2. (a) Mean Density (b) RMS Density Fluctuation; (——) LSC_1; (▲) HSC_1; (——) LSC_2; (▼) HSC_2; (— - —) SCCTP.

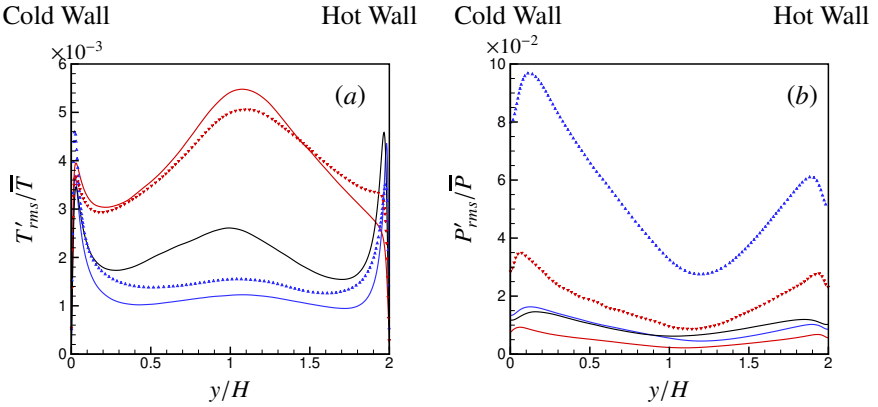

Figure 4.4: Temperature and pressure fluctuations as a function of channel height for turbulent flows of supercritical CO_2; (a) Temperature Fluctuation; (b) Pressure fluctuation; (——) LSC_1; (▲) HSC_1; (——) LSC_2; (▼) HSC_2; (— - —) SCCTP.

4.4 Near Wall Turbulence

The streaks for the fluctuations of the streamwise velocity with respect to Favre average (u''), density, temperature and pressure fluctuations normalized by their mean values near the hot and the cold walls of the channel are shown for LSC_2 in Figure 4.5. The density, pressure and temperature streaks are normalized by their local mean values. The computational box is also scaled by the semi-local variables. So, the streaks are plotted as a function of x^* and z^*. The streaks are calculated at the locations $y^* = 14.72$ near the hot wall and $y^* = 16.98$ near the cold wall based on the maxima for the root mean square velocity fluctuations near the respective walls. For this case, it is seen that there is no peak for the density fluctuation near the hot wall. This is due to the trans-critical transition very close to the cold wall. This behaviour is affirmed on analyzing the streaks for the density fluctuation in Figure 4.4 when it is seen that, near the hot wall, there are almost no high density streaks whereas, near the cold wall, high density streaks are more prevalent. The temperature fluctuation streaks indicate the same behaviour to a lesser degree. Near the cold wall, there is a higher occurrence of high temperature fluctuations compared to that near the hot wall. The streaks also prove that, near the walls, the density is much more correlated with temperature compared to pressure as, no significant occurrences of high or low pressure fluctuations can be seen near the walls. The analysis of the Favre averaged velocity fluctuations near the walls reveal that the high speed streaks are more enhanced near the cold wall compared to the hot wall. Also, the velocity streaks indicate more coherent structures near the cold wall.

4.5 Van Driest scaling and extended van Driest scaling

For all of the above mentioned simulations, the temperatures and the wall stresses at the cold and hot walls are different from one another. So, the channel has been divided into hot and cold sides depending on the location of zero Reynolds shear stress. The location of zero shear stress for the five cases are listed in Table 4.4.

The laminar, turbulent and total shear stress on the hot and the cold sides of the channel scaled by the wall stress on the respective sides, are shown in Figure 4.6. The total shear stress shows a small kink near the walls. This is due to the fact that the effect of fluctuating viscosity has not been considered.

The semi-local scaled variables are evaluated as follows

$$u^*_{\tau c} = \sqrt{\frac{\tau_{wc}}{\overline{\rho}}}, u^*_{\tau h} = \sqrt{\frac{\tau_{wh}}{\overline{\rho}}}, \tag{4.3}$$

$$Re^*_{\tau c} = \frac{\overline{\rho} u^*_{\tau c} H}{\overline{\mu}}, Re^*_{\tau h} = \frac{\overline{\rho} u^*_{\tau h} H}{\overline{\mu}}, \tag{4.4}$$

$$y^* = \frac{y \overline{\rho} u^*_{\tau}}{\overline{\mu}} = \frac{y}{H} \frac{\overline{\rho} u^*_{\tau} H}{\overline{\mu}}, \tag{4.5}$$

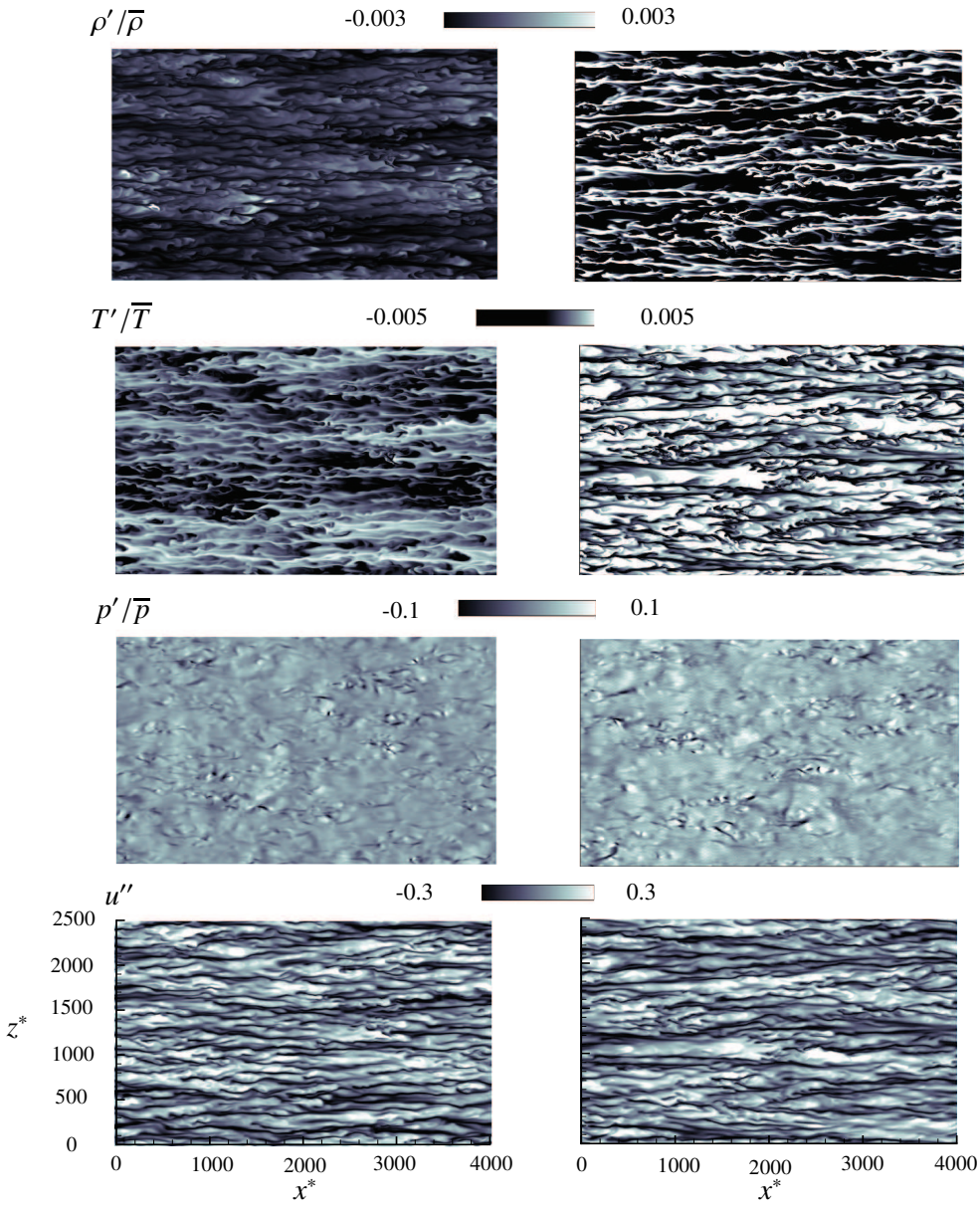

Figure 4.5: Fluctuations for streamwise velocity (u''), density ($\rho'/\overline{\rho}$), temperature ($T'/\overline{T}$), pressure ($p'/\overline{p}$) on the hot and cold sides of the channel for turbulent flows of supercritical CO_2 (LSC_2). From top to bottom: Density streaks, temperature streaks, pressure streaks, velocity streaks. Left hand side: Hot wall ($y^* = 14.72$) and Right hand side: Cold Wall ($y^* = 16.98$).

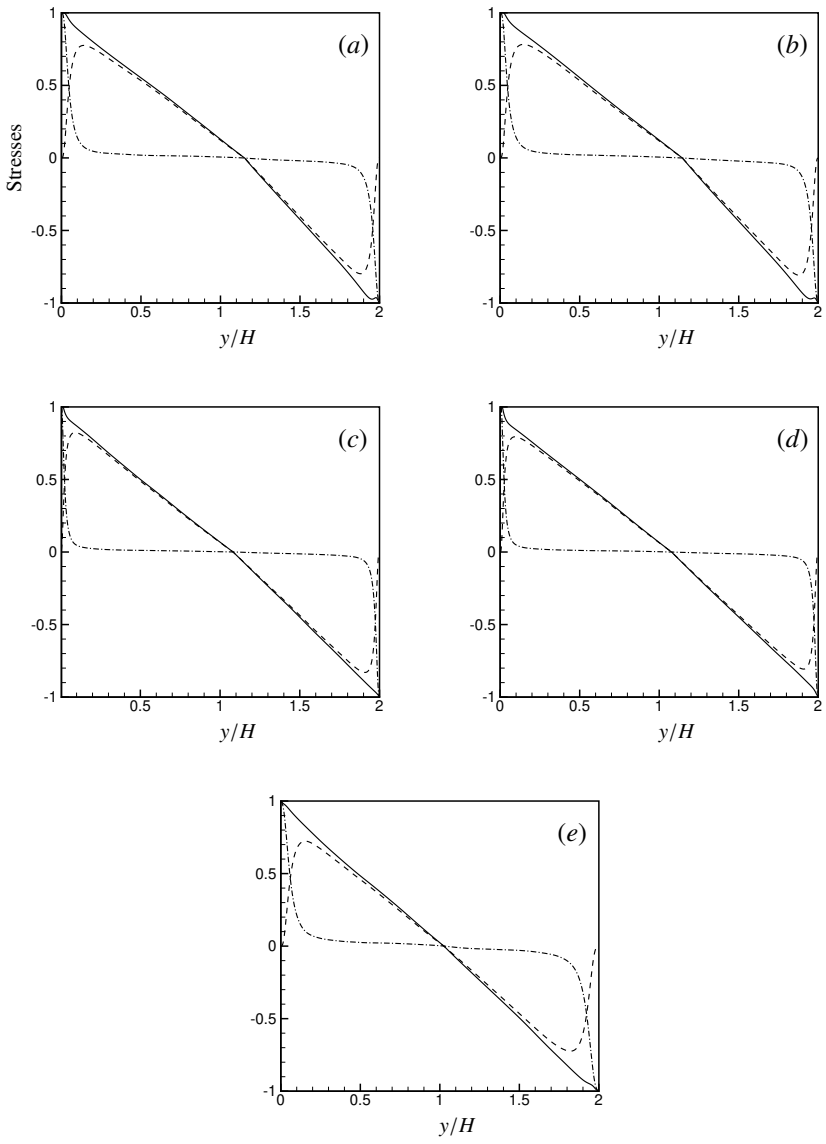

Figure 4.6: Shear stresses as a function of channel height for turbulent flows of supercritical CO_2. (– – –) $-\overline{\rho}\overline{u'v'}/\tau_w$; (—·—) $\left(\overline{\mu}\partial\overline{U}/\partial y\right)/\tau_w$; (———) $\left(-\overline{\rho}\overline{u'v'}+\left(\overline{\mu}\partial\overline{U}/\partial y\right)\right)/\tau_w$. (a) LSC_1; (b) HSC_1; (c) LSC_2; (d) HSC_2; (e) SCCTP.

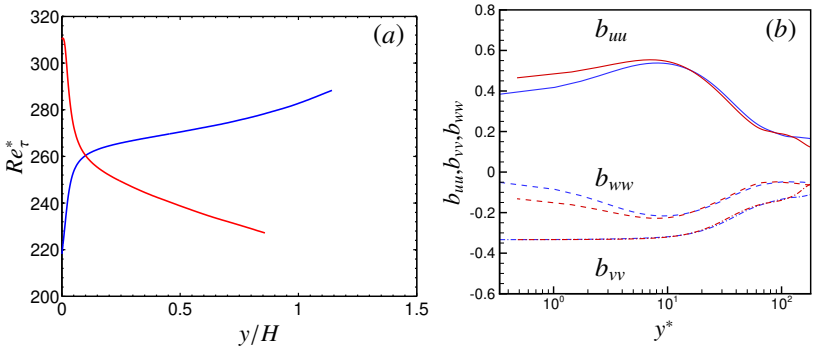

Figure 4.7: Re^*_τ and anisotropies as a function of y^* for LSC_1. (———) b_{uu}; (—·—) b_{vv}; (– – –) b_{ww}; (———) Cold Side; (———) Hot Side.

Case	Location of zero Shear Stress
LSC_1	$y/H = 1.1488$
HSC_1	$y/H = 1.1470$
LSC_2	$y/H = 1.0765$
HSC_2	$y/H = 1.0602$
SCCTP	$y/H = 1.0172$

Table 4.4: Location of the boundary between hot and cold sides of the channel

$$y^*_c = yRe^*_{\tau c};\ y^*_h = yRe^*_{\tau h}. \tag{4.6}$$

The subscripts c and h represent the cold and hot side of the channel respectively.

The semi-local scaled Reynolds number (Re^*_τ) can be expressed in terms of the friction Reynolds number at the wall ($Re_{\tau w}$) as: $Re^*_\tau = \sqrt{\overline{\rho}/\rho_w}/\left(\overline{\mu}/\mu_w\right) Re_{\tau w}$. Based on Patel *et al.* (2015), the changes in the semi-local Reynolds number, Re^*_τ, defined as $Re^*_\tau = \overline{\rho} u^*_\tau H/\overline{\mu} = \sqrt{\overline{\rho}/\rho_w}/\left(\overline{\mu}/\mu_w\right) Re_{\tau w}$, have a significant impact on inter-component energy transfer and hence on turbulence anisotropy in the flow field. The anisotropies are defined as $b_{ij} = \overline{u'_i u'_j}/\overline{u'_k u'_k} - 1/3\delta_{ij}$, where δ_{ij} is the Kronecker delta. When $dRe^*_\tau/dy < 0$, it causes a reduction in momentum transfer and redistribution in turbulent kinetic energy from the streamwise direction to the other directions. This is evident in an increase in the streamwise anisotropy and a decrease in the spanwise anisotropy. The opposite behaviour is observed when $dRe^*_\tau/dy > 0$. The semi-locally scaled Reynolds number (Re^*_τ) and the anisotropies b_{uu}, b_{ww} and b_{vv} in the streamwise , spanwise and wall-normal directions, respectively are show for the simulations in figures 4.7 to 4.10. It is seen from figures 4.7 and 4.8, that for the cases LSC_1 and HSC_1, the streamwise anisotropy on the

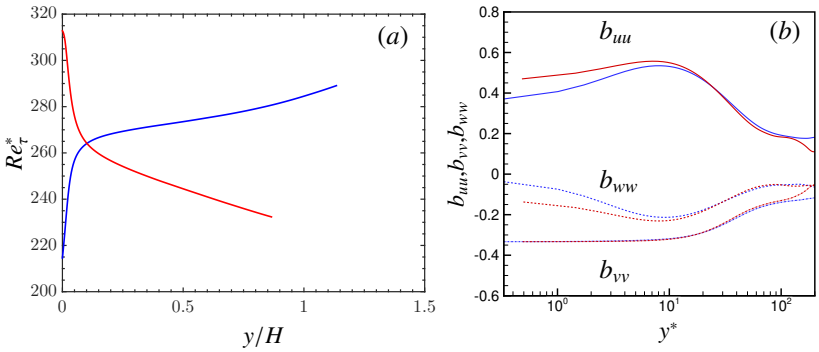

Figure 4.8: Re_τ^* and anisotropies as a function of y^* for HSC_1. (———) b_{uu}; (—·—) b_{vv}; (– – –) b_{ww}; (———) Cold Side; (———) Hot Side.

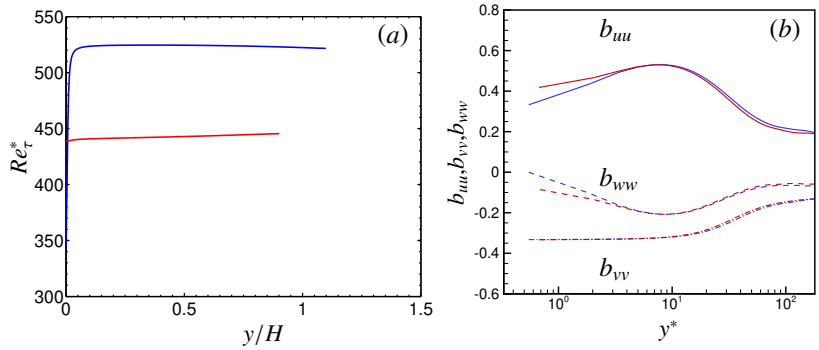

Figure 4.9: Re_τ^* and anisotropies as a function of y^* for LSC_2. (———) b_{uu}; (—·—) b_{vv}; (– – –) b_{ww}; (———) Cold Side; (———) Hot Side.

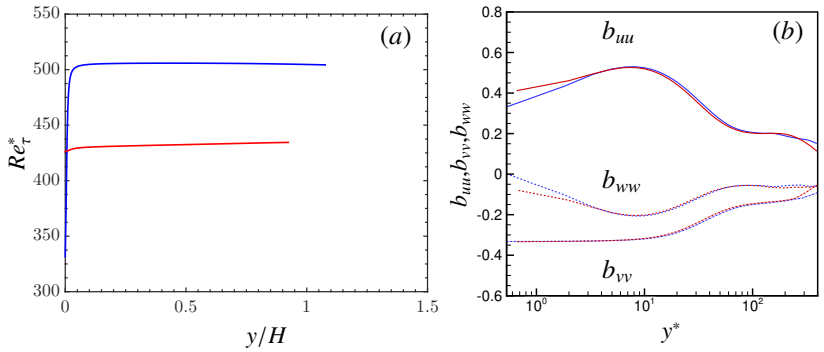

Figure 4.10: Re^*_τ and anisotropies as a function of y^* for HSC_2. (———) b_{uu}; (—·—) b_{vv}; (– – –) b_{ww}; (———) Cold Side; (———) Hot Side.

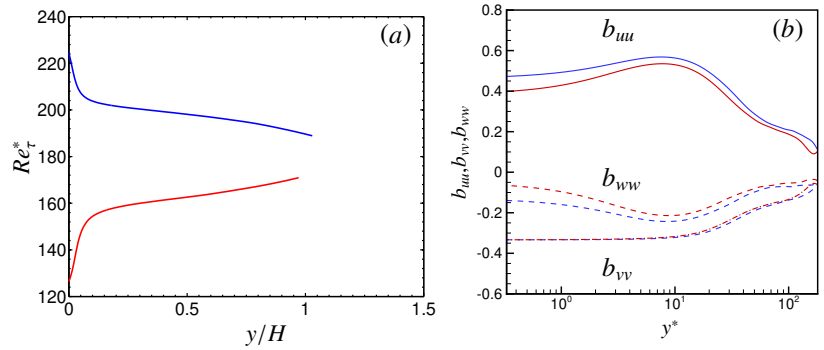

Figure 4.11: Re^*_τ and anisotropies as a function of y^* for SCCTP. (———) b_{uu}; (—·—) b_{vv}; (– – –) b_{ww}; (———) Cold Side; (———) Hot Side.

cold side is less than that on the hot side of the channel. This can be explained by the fact that $dRe_\tau^*/dy > 0$ on the cold side of the channel and $dRe_\tau^*/dy < 0$ on the hot side of the channel. So, there is a reduction in redistribution of turbulent kinetic energy on the hot side and an increase on the cold side of the channel. The exact opposite is observed for the streamwise anisotropy in SCCTP as Re_τ^* is decreasing on the cold side of the channel and increasing on the hot side of the channel. This is demonstrated in figure 4.11. From figures 4.9 and 4.10, it is observed that, for the cases LSC_2 and HSC_2, the anisotropies are nearly equal on the two sides of the channel due to the flatter Re_τ^* profiles as a result of which dRe_τ^*/dy is almost equal to zero for most of the channel height. For all the cases, it is seen that an increase in streamwise anisotropy is accompanied with a corresponding decrease in the spanwise anisotropy, while the anisotropy in the wall-normal direction in the hot and cold sides of the channel seems to be relatively unaffected whether Re_τ^* is increasing or decreasing. The van Driest transformation, as mentioned in Huang *et al.* (1995) has been previously used to scale the streamwise velocity $\left(\overline{u}^{VD}\right)$ in compressible flows. This provides a reasonable collapse of the velocity profiles with the log law of the wall. A more recent approach is the extended van Driest transformation developed by Trettel & Larsson (2016) and Patel *et al.* (2016). The extended van Driest transformed velocity $(\overline{u}^*)$ is plotted as a function of y^* for our simulations in the figure 4.12. This is seen to produce a fairly good collapse of the velocity profiles with the log law for the wall.

4.6 Turbulent statistics and budgets

The velocity fluctuations and the quantities involved in evaluating the budgets for the turbulent kinetic energy ($k = 1/2\widetilde{\overline{\rho}u_i''u_i''}$) are scaled by the semi-local variables and plotted as a function of y^*. The budget equation used is the same as that given by Morinishi *et al.* (2004) and Huang *et al.* (1995). This is given as

$$P_k + D_k + \epsilon_k + C_k = 0, \tag{4.7}$$

where the production P_k, D_k, ϵ_k and C_k refer to the production, diffusion, dissipation and the compressibility terms for turbulent kinetic energy. These are expressed as

$$P_k = -\widetilde{\overline{\rho}u''v''}\frac{\partial\widetilde{u}}{\partial y}, D_k = \frac{\partial\left[\overline{\Gamma'_{i2}u'_i} - \widetilde{\overline{\rho}v''u_i''u_i''} - \overline{p'v'}\right]}{\partial y}, \tag{4.8}$$

$$\epsilon_k = -\overline{\Gamma'_{ij}\frac{\partial u'_i}{\partial x_j}}, C_k = -C_{k1} + C_{k2} + C_{k3}, \tag{4.9}$$

$$C_{k1} = \overline{v''}\frac{\partial\overline{p}}{\partial y}; C_{k2} = \overline{u_i''\frac{\partial\Gamma_{i2}}{\partial y}}, C_{k3} = \overline{p'\frac{\partial u'_k}{\partial x_k}}. \tag{4.10}$$

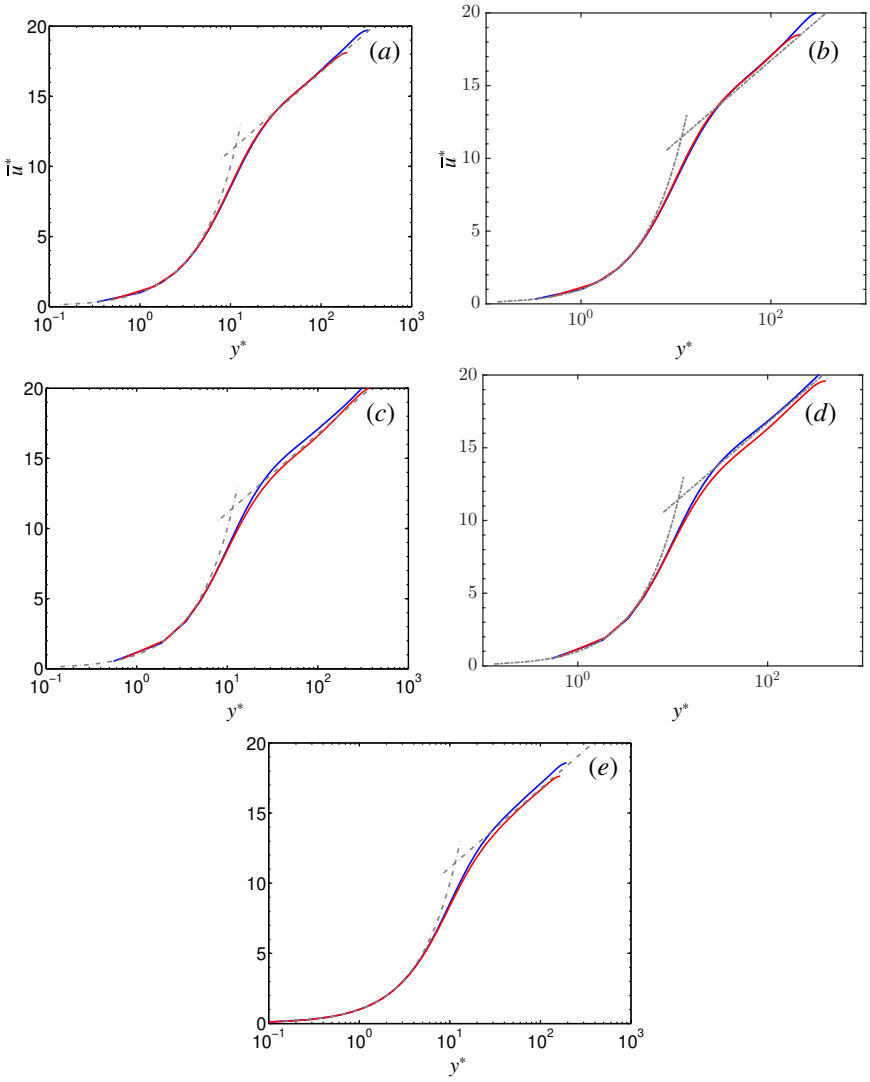

Figure 4.12: Extended van Driest transformed velocity as a function of y^* for turbulent flows of supercritical CO_2. (a) LSC_1; (b) HSC_1; (c) LSC_2; (e) HSC_2; (e) SCCTP.

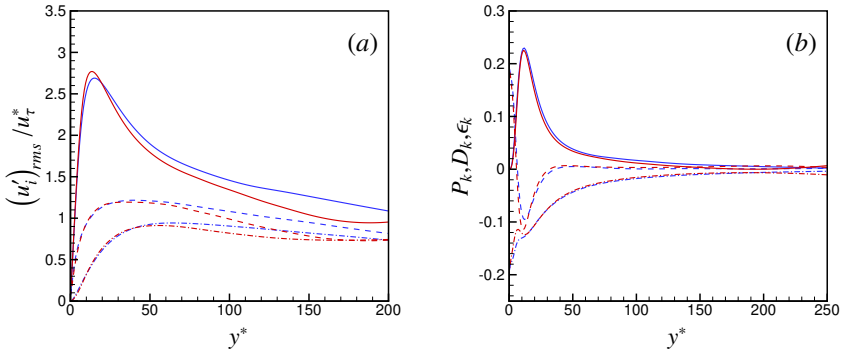

Figure 4.13: Semi-locally scaled velocity fluctuations and turbulent kinetic energy budgets as a function of y^* for LSC_1. (a) (———) $u'rms/u_\tau^*$; (—·—) v'_{rms}/u_τ^* (– – –) w'_{rms}/u_τ^*. (b) (———) P_k; (– – –) D_k ; (—··—) ϵ_k. (———) Cold Side; (———) Hot Side.

The velocity fluctuations and the turbulent kinetic energy budgets scaled by the semi-local variables are shown in figures 4.13 to 4.17. The velocity fluctuations and the turbulent kinetic energy budgets, if scaled by bulk variables do not collapse on top of each other. But, the values on the hot and cold sides of the channel are found to collapse on top of each other when scaled by semi-local variables. The validity of the semi-local scaling also reaffirms the relevance of the Morkovin hypothesis for all of the simulations performed. This signifies that the changes in the turbulence structures are due to the change in the mean density and mean viscosity gradients and fluctuations of the quantities have a limited impact on the turbulence in the flow.

4.7 Inertial and viscous effects

As the flow is compressible in nature with variable viscosity, the turbulence in the flow is influenced both by the variable inertial and viscous effects on the hot and cold side of the channel. The magnitudes of the inertial and viscous forces on the hot and cold sides of the channel were quantified by Zonta *et al.* (2012). These are given as follows.

$$F_I^h \propto \rho_b^h U_b^h (h^h)^2, F_I^c \propto \rho_b^c U_b^c (h^c)^2, \tag{4.11}$$

where (F_I^h F_I^c), (ρ_b^h ρ_b^c), (U_b^h U_b^c) and (h^h h^c) refer to the inertial force, the bulk density, the bulk velocity and the channel height on the hot and cold sides of the channel, respectively.

$$F_V^h \propto \mu_b^h U_b^h h^h, F_V^c \propto \mu_b^c U_b^c h^c, \tag{4.12}$$

where (F_V^h F_V^c) and (μ_b^h μ_b^c) refer to the viscous forces and the bulk viscosity on the hot and cold sides of the channel, respectively. The ratio of inertial and viscous forces on the hot and cold sides of the channel are given in Table 4.5.

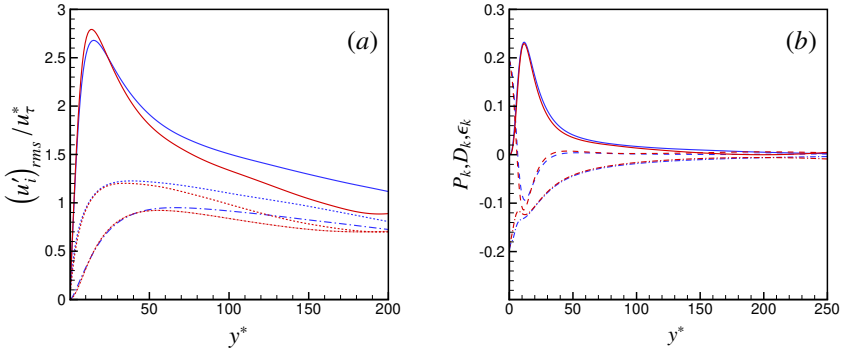

Figure 4.14: Semi-locally scaled velocity fluctuations and turbulent kinetic energy budgets as a function of y^* for HSC_1. (a) (———) $u'rms/u_\tau^*$; (—·—) v'_{rms}/u_τ^* (– – –) w'_{rms}/u_τ^*. (b) (———) P_k; (– – –) D_k ; (—··—) ϵ_k. (———) Cold Side; (———) Hot Side.

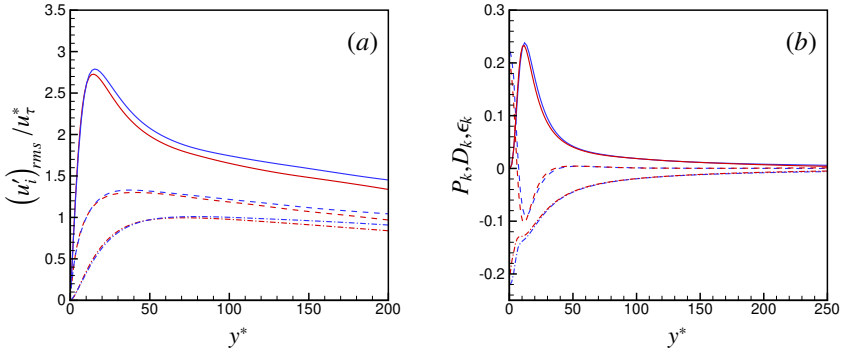

Figure 4.15: Semi-locally scaled velocity fluctuations and turbulent kinetic energy budgets as a function of y^* for LSC_2. (a) (———) $u'rms/u_\tau^*$; (—·—) v'_{rms}/u_τ^* (– – –) w'_{rms}/u_τ^*. (b) (———) P_k; (– – –) D_k ; (—··—) ϵ_k. (———) Cold Side; (———) Hot Side.

Case	F_I^c/F_I^h	F_V^c/F_V^h
LSC_1	2.03	1.60
HSC_1	2.00	1.58
LSC_2	1.57	1.23
HSC_2	1.55	1.24
SCCTP	1.39	1.06

Table 4.5: Ratio of the inertial and viscous forces on the hot and cold sides of the channel

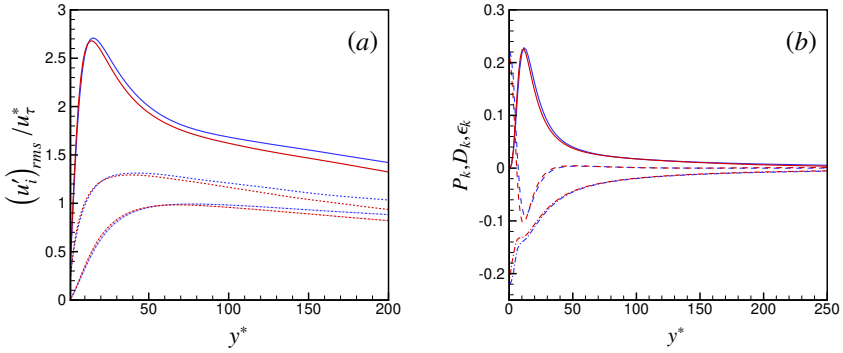

Figure 4.16: Semi-locally scaled velocity fluctuations and turbulent kinetic energy budgets as a function of y^* for HSC_2. (a) (———) $u'rms/u_\tau^*$; (—·—) v'_{rms}/u_τ^* (– – –) w'_{rms}/u_τ^*. (b) (———) P_k; (– – –) D_k ; (—·—) ϵ_k. (———) Cold Side; (———) Hot Side.

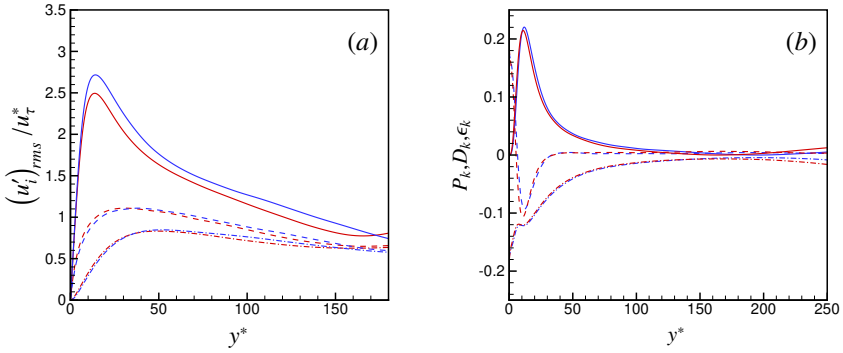

Figure 4.17: Semi-locally scaled velocity fluctuations and turbulent kinetic energy budgets as a function of y^* for SCCTP. (a) (———) $u'rms/u_\tau^*$; (—·—) v'_{rms}/u_τ^* (– – –) w'_{rms}/u_τ^*. (b) (———) P_k; (– – –) D_k ; (—·—) ϵ_k. (———) Cold Side; (———) Hot Side.

This shows that in all the cases, there is an increase in the viscous forces from the hot to the cold side of the channel, but there is an even bigger increase in inertial forces. This is due to the fact that the inertial force is proportional to the square of the channel height and the channel height on the cold side is greater than the channel height on the hot side for each of the cases simulated. Also, for the constant viscosity case, the ratio of the viscous forces on the two sides of the channel is found to be close to unity. This is not the case with the variable viscosity cases.

4.8 Compressibility Effects

The velocity field can be decomposed into the sum of its' solenoidal and dilatational components, as given by $u = u_s + u_d$, where u_s and u_d give the solenoidal and the dilataional components of the velocity, respectively. The solenoidal velocity gives the incompressible component of the velocity field and is characterized by $\nabla.u_s = 0$. So, we get, $\nabla.u = \nabla.u_d$. The dilatational velocity is the irrotational part of the velocity field and is characterized by $\nabla \times u_d = 0$. This gives the relation $\nabla \times u = \nabla \times u_s$.

Given these definitions, it is possible to derive the Helmholtz decomposition for the vorticities as

$$\nabla \times \nabla \times A = \nabla (\nabla.A) - \nabla^2 A. \tag{4.13}$$

Applying this identity to the above relation, we get,

$$\nabla (\nabla.u) - \nabla^2 u = \nabla (\nabla.u_s) - \nabla^2 u_s. \tag{4.14}$$

As $\nabla.u_s = 0$, it gives us the following Poisson equation for the solenoidal velocity component

$$-\nabla^2 u_s = \nabla (\nabla.u) - \nabla^2 u = \nabla \times \nabla \times u. \tag{4.15}$$

Solving this Poisson relation, we can obtain the value of u_s. This is then subtracted from the total velocity to find the dilatational velocity u_d.

Previous authors, such as Huang *et al.* (1995); Kreuzinger *et al.* (2006) have divided the turbulent kinetic energy dissipation into the sum of the solenoidal, dilatational and inhomogeneous parts. The solenoidal, dilatational and the inhomogeneous parts of the dissipation of turbulent kinetic energy are derived in the following manner.

$$\begin{aligned} \epsilon_k = \overline{\Gamma'_{ij} \frac{\partial u''_i}{\partial x_j}} = \overline{\left(\mu S^s_{ij} + \mu S^d_{ij}\right)' \frac{\partial \left(u''_{is} + u''_{id}\right)}{\partial x_j}} \\ = \overline{\left(\mu S^s_{ij}\right)' \frac{\partial u''_{is}}{\partial x_j}} + \overline{\left(\mu S^d_{ij}\right)' \frac{\partial u''_{id}}{\partial x_j}} + \overline{\left(\mu S^s_{ij}\right)' \frac{\partial u''_{id}}{\partial x_j}} + \overline{\left(\mu S^d_{ij}\right)' \frac{\partial u''_{is}}{\partial x_j}}. \end{aligned} \tag{4.16}$$

$$\epsilon^s_k = \overline{\left(\mu S^s_{ij}\right)' \frac{\partial u''_{is}}{\partial x_j}}, \epsilon^d_k = \overline{\left(\mu S^d_{ij}\right)' \frac{\partial u''_{id}}{\partial x_j}}, \epsilon^{inh}_k = \overline{\left(\mu S^s_{ij}\right)' \frac{\partial u''_{id}}{\partial x_j}} + \overline{\left(\mu S^s_{ij}\right)' \frac{\partial u''_{id}}{\partial x_j}}, \tag{4.17}$$

where ϵ_k^s, ϵ_k^d and ϵ_k^{inh} refer to the solenoidal, dilatational and inhomogeneous parts of the dissipation of turbulent kinetic energy. The inhomogeneous component of the dissipation is found to be negligible. The dilatational dissipation is the part of the total dissipation attributed to compressibility effects. So, the total dissipation can be divided into the sum of the incompressible and compressible parts, namely, the solenoidal and the dilatational dissipation. The compressibility effects are thereby evaluated by comparing the solenoidal dissipation to the total dissipation for turbulent kinetic energy (ϵ_k). Both of these quantities on the hot and cold sides of the channel are scaled by the semi-local variables and are plotted in figure 4.18 for the cases HSC_1, LSC_2 and HSC_2. If compressibility effects are minimal, the solenoidal dissipation and the total dissipation should almost collapse on top of each other. The biggest difference between the solenoidal and the total dissipation is observed in the case LSC_2 and HSC_2 very near to the cold wall. The other case HSC_1 with trans-critical transition near the middle of the channel does not exhibit significant levels of compressibility close to the walls as the solenoidal and total dissipations almost collapse on top of each other. The same has been observed for the cases LSC_1 and SCCTP, due to which the figures for these cases have not been shown above. So, for turbulent flows of supercritical CO_2, it is possible to experience significant levels of compressibility caused by trans-critical transition near to the cold wall. But, overall, the compressibility effects experienced are still small as they are significant only in the case of trans-critical transition very close to the wall and are confined to a limited region close to the wall. It is also concluded that the effect of trans-critical transition close to the cold wall is more significant for creating compressibility effects than an increase in Mach number. This is evident from the observation that the low Mach number case LSC_2 has significant compressibility effects near the cold wall, whereas the high Mach number case HSC_1 does not. For all the cases, the solenoidal dissipation is more in magnitude near the cold wall compared to the total dissipation. Thus, the dilatational dissipation is opposite in sign to the total dissipation of turbulent kinetic energy near the cold wall. So, the compressibility effects near the cold wall act as a source for turbulent kinetic energy production.

4.9 Real Gas Effects

Turbulent flows of ideal gases with low Mach numbers behave mostly like an isobaric process. For ideal gases, we have, in general

$$\frac{dP}{\overline{P}} = \frac{dT}{\overline{T}} + \frac{d\rho}{\overline{\rho}}. \tag{4.18}$$

As dP is small in magnitude compared to dT and $d\rho$, we get,

$$\frac{dT}{\overline{T}} \approx \frac{d\rho}{\overline{\rho}}. \tag{4.19}$$

Replacing dT and $d\rho$ with T_{rms} and ρ_{rms}, we get,

$$\frac{T_{rms}}{\overline{T}} \approx \frac{\rho_{rms}}{\overline{\rho}}. \tag{4.20}$$

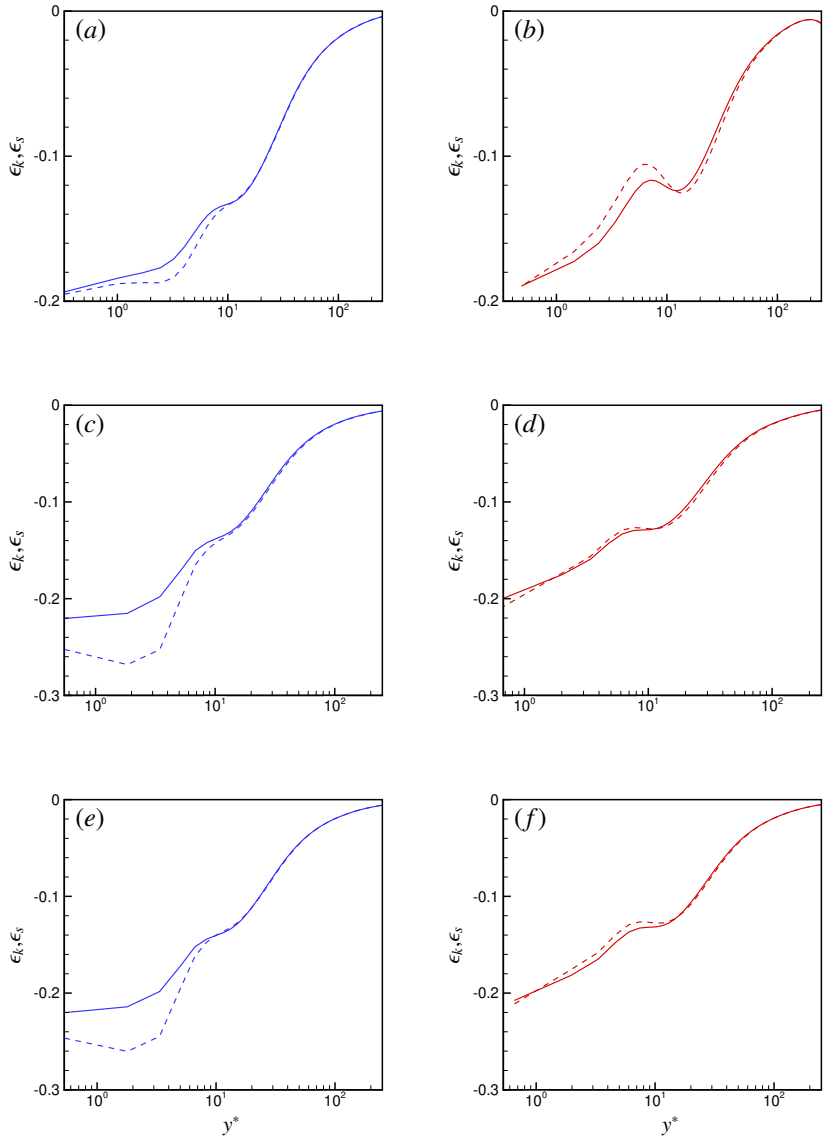

Figure 4.18: Solenoidal and total dissipation as a function of y^* for turbulent flows of supercritical CO_2 (——) ϵ_k; (– – –) ϵ_s; (——) Cold Side; (——) Hot Side.
Top row: HSC_1; Middle row: LSC_2; Bottom row: HSC_2.

This relation is seen to be satisfied by fully developed turbulent flows of an ideal gas at low Mach numbers. The same concept can be extended to low Mach number supercritical fluid flows which are represented by real gas equations of state. In case of the simulations LSC_1, LSC_2 and SCCTP which use the Peng Robinson equation of state, this is done as follows

$$P = \frac{\rho RT}{1 - b\rho} - \frac{a\alpha\rho^2}{1 + 2b\rho - b^2\rho^2}. \tag{4.21}$$

Using the chain rule of calculus and approximating the derivatives as the derivatives with respect to the mean quantities, we get,

$$dP = \left(\frac{\partial \overline{P}}{\partial \overline{\rho}}\right)_T d\rho + \left(\frac{\partial \overline{P}}{\partial \overline{T}}\right)_\rho dT. \tag{4.22}$$

Replacing dP,$d\rho$ and dT by P_{rms},ρ_{rms} and T_{rms}, respectively, we get,

$$P_{rms} = \left(\frac{\partial \overline{P}}{\partial \overline{\rho}}\right)_T \rho_{rms} + \left(\frac{\partial \overline{P}}{\partial \overline{T}}\right)_\rho T_{rms}. \tag{4.23}$$

In the case of turbulent flows of supercritical CO_2 at low Mach numbers, it behaves nearly like an isobaric process and hence, the root mean square (rms) density fluctuations can be predicted using the rms pressure fluctuations, the rms temperature fluctuations and the partial derivatives for mean pressure with respect to mean temperature and mean density as derived from the Peng Robinson equation of state. This is given as follows

$$\rho^0_{rms} \approx \left(P_{rms} - \left(\frac{\partial \overline{P}}{\partial \overline{T}}\right)_\rho T_{rms}\right) / \left(\frac{\partial \overline{P}}{\partial \overline{\rho}}\right)_T, \tag{4.24}$$

where the superscript 0 is used to define the predicted value of the density fluctuations. The derivatives are calculated as

$$\left(\frac{\partial \overline{P}}{\partial \overline{\rho}}\right)_T = \frac{R\overline{T}}{(1 - b\overline{\rho})^2} - \frac{2a\overline{\alpha\rho}\,(1 + b\overline{\rho})}{\left(1 + 2b\overline{\rho} - b^2\overline{\rho}^2\right)^2}, \tag{4.25}$$

$$\left(\frac{\partial \overline{P}}{\partial \overline{T}}\right)_\rho = \frac{\overline{\rho}R}{1 - b\overline{\rho}} - \frac{a\overline{\rho}^2 \frac{d\overline{\alpha}}{dT}}{1 + 2b\overline{\rho} - b^2\overline{\rho}^2}. \tag{4.26}$$

The actual and predicted values of the rms density fluctuations are shown for the lower Mach number cases in the figure 4.19. From the figure, it is seen that this model provides a relatively good match with the actual value of the rms density fluctuation as obtained from the DNS of fully developed turbulent supercritical CO_2 flows.

The pressure as derived from the Peng Robinson equation consists of three contributions, namely the ideal gas contribution and the repulsive and attractive contributions which constitute the real gas effects. These are defined as follows

$$P_{id} = \rho RT, P_{rep} = \frac{b\rho^2 RT}{1-b\rho}, P_{att} = \frac{a\alpha\rho^2}{1+2b\rho-b^2\rho^2}. \tag{4.27}$$

The total pressure is given as

$$P = P_{id} + P_{rep} - P_{att}. \tag{4.28}$$

The pressure fluctuations, which are negligible in magnitude compared to the density fluctuations can then be derived as a balance of the following terms

$$\frac{P_{rms}}{\overline{P}_{id}} = \left(\frac{\partial \overline{P}}{\partial \overline{T}}\right)_{\rho} \frac{T_{rms}}{\overline{P}_{id}} - \left(\frac{\partial \overline{P}}{\partial \overline{\rho}}\right)_{T} \frac{\rho^0_{rms}}{\overline{P}_{id}}. \tag{4.29}$$

Now, on decomposing the pressure in the Peng Robinson equation of state into the ideal, repulsive and attractive contributions, we get,

$$\frac{P^{id}_{rms}}{\overline{P}_{id}} = \left(\frac{\partial \overline{P}_{id}}{\partial \overline{T}}\right)_{\rho} \frac{T_{rms}}{\overline{P}_{id}} - \left(\frac{\partial \overline{P}_{id}}{\partial \overline{\rho}}\right)_{T} \frac{\rho^0_{rms}}{\overline{P}_{id}}, \tag{4.30}$$

$$\left(P'^{id}_{rms}\right)^{nd} = \frac{P^{id}_{rms}}{\overline{P}_{id}} = \frac{T_{rms}}{\overline{T}} - \frac{\overline{\rho}^0_{rms}}{\overline{\rho}}, \tag{4.31}$$

where the superscript *nd* is an acronym for non-dimensional

$$\frac{P^{rep}_{rms}}{\overline{P}_{id}} = \left(\frac{\partial \overline{P}_{rep}}{\partial \overline{T}}\right)_{\rho} \frac{T_{rms}}{\overline{P}_{id}} - \left(\frac{\partial \overline{P}_{rep}}{\partial \overline{\rho}}\right)_{T} \frac{\rho^0_{rms}}{\overline{P}_{id}}, \tag{4.32}$$

$$\left(P'^{rep}_{rms}\right)^{nd} = \frac{P^{rep}_{rms}}{\overline{P}_{id}} = \frac{b\overline{\rho}}{1-b\overline{\rho}} \frac{T_{rms}}{\overline{T}} - \frac{b\overline{\rho}\,(2-b\overline{\rho})}{(1-b\overline{\rho})^2} \frac{\rho^0_{rms}}{\overline{\rho}}, \tag{4.33}$$

$$\frac{P^{att}_{rms}}{\overline{P}_{id}} = \left(\frac{\partial \overline{P}_{att}}{\partial \overline{T}}\right)_{\rho} \frac{T_{rms}}{\overline{P}_{id}} - \left(\frac{\partial \overline{P}_{att}}{\partial \overline{\rho}}\right)_{T} \frac{\rho^0_{rms}}{\overline{P}_{id}}, \tag{4.34}$$

$$\left(P'^{att}_{rms}\right)^{nd} = \frac{P^{att}_{rms}}{\overline{P}_{id}} = \frac{a\overline{\rho}\frac{d\overline{\alpha}}{d\overline{T}}}{\left(1+2b\overline{\rho}-b^2\overline{\rho}^2\right)R} \frac{T_{rms}}{\overline{T}} - \frac{2a\overline{\alpha\rho}\,(1+b\overline{\rho})}{\left(1+2b\overline{\rho}-b^2\overline{\rho}^2\right)^2 R\overline{T}} \frac{\rho^0_{rms}}{\overline{\rho}}. \tag{4.35}$$

The ideal, repulsive and attractive components of the rms pressure fluctuation is shown in figure 4.20 for the cases LSC_1, LSC_2 and SCCTP. It is seen that the sum of these contributions balance each other and the actual pressure fluctuation is negligible in magnitude compared to each of these components. This analysis is not applicable for higher Mach number cases. At higher Mach numbers, the initial assumption of approximating the derivatives of pressure by the derivatives taken with respect to mean quantities is not applicable.

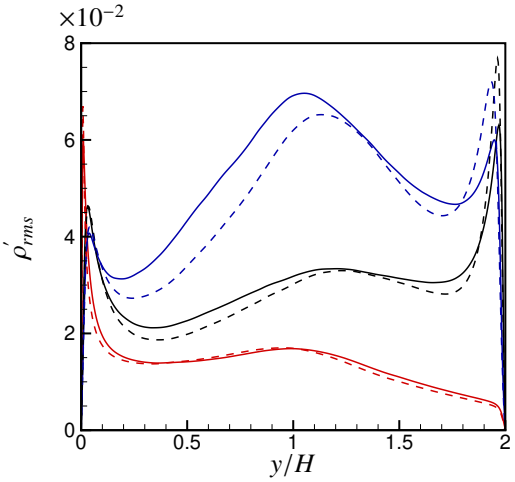

Figure 4.19: Actual and predicted rms density fluctuations as a function of channel height. (———) Actual density fluctuation; (– – –) Predicted density fluctuation. (———) LSC_1; (———) LSC_2; (———) SCCTP

4.10 Turbulent heat flux budget equation

The turbulent heat flux budget equation is given as

$$\frac{\partial\overline{\left(\rho h'' u_i''\right)}}{\partial t} + C_{h,i} + T_{h,i} + P_{h,i} + V_{h,i} + \epsilon_{h,i} + \Psi_{h,i} + W_{h,i} = 0, \tag{4.36}$$

where $C_{h,i}$ is the mean convection, $T_{h,i}$ is the turbulence diffusion, $P_{h,i}$ is the production, $V_{h,i}$ is the molecular diffusion, $\epsilon_{h,i}$ is the dissipation, $\Psi_{h,i}$ is the correlation between pressure gradient and fluctuating enthalpy and $W_{h,i}$ is the transport of the viscous dissipation by fluctuating velocity. These terms are represented as

$$C_{h,i} = \frac{\partial\overline{\left(\rho\widetilde{u}_j h'' u_i''\right)}}{\partial x_j}, T_{h,i} = \frac{\partial\overline{\left(\rho u_j'' h'' u_i''\right)}}{\partial x_j}, P_{h,i} = \overline{h''\rho u_j''}\frac{\partial\widetilde{u}_i}{\partial x_j} + \overline{u_i''\rho u_j''}\frac{\partial\widetilde{h}}{\partial x_j}, \tag{4.37}$$

$$V_{h,i} = \left(\frac{\partial\overline{\left(u_i'' q_j\right)}}{\partial x_j} - \frac{\partial\overline{\left(h''\Gamma_{ij}\right)}}{\partial x_j}\right), \epsilon_{h,i} = \left(\overline{\Gamma_{ij}\frac{\partial h''}{\partial x_j}} - \overline{q_j\frac{\partial u_i''}{\partial x_j}}\right), \tag{4.38}$$

$$\Psi_{h,i} = \overline{h''\frac{\partial\left(P\delta_{ij}\right)}{\partial x_j}}, W_{h,i} = -\overline{u_i''\Gamma_{kj}\frac{\partial u_k}{\partial x_j}}. \tag{4.39}$$

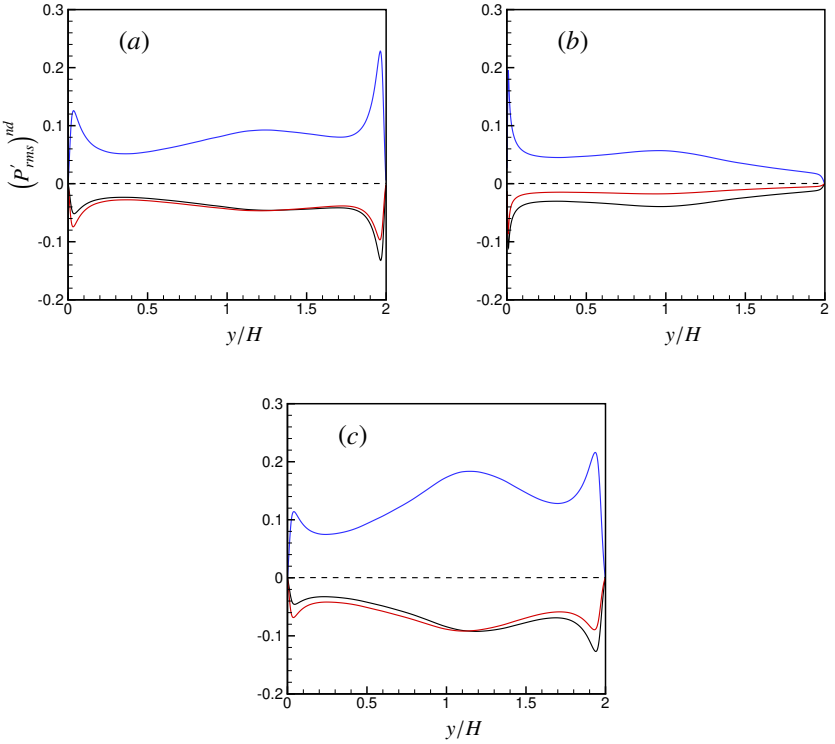

Figure 4.20: Contribution of the ideal, repulsive and the attractive components to the pressure fluctuations. (———) $\left(P'^{id}_{rms}\right)^{nd}$ (———) $\left(P'^{rep}_{rms}\right)^{nd}$ (———) $\left(P'^{att}_{rms}\right)^{nd}$; (– – –) $\left(P'_{rms}\right)^{nd}$; (a) ($LSC_1$); (b) ($LSC_2$); (c) SCCTP.

The derivation of this equation and the definitions for the terms mentioned above are given in Appendix B. The budgets for the turbulent heat flux are plotted in the figure 4.21. It is seen that these budgets are balanced for the cases LSC_1 and SCCTP. The budgets are only shown for two out of the five cases simulated. This is due to the reason that the turbulent heat flux budgets constitute fourth order terms. It is required to run the simulation for each case for a longer duration of time in order to get converged statistics for fourth order terms. This could not be achieved for all the cases considered due to the delay in acquiring computational resources. Comparison between the cases LSC_1 and SCCTP reveals that the average thermal conductivity is lower near the walls for LSC_1 compared to SCCTP. Also, the average heat capacity at constant pressure $\overline{C_p}$ is higher near the walls for LSC_1 in comparison to SCCTP. This is demonstrated in figure 4.22. A high thermal conductivity κ indicates that heat is conducted more easily across a medium and hence corresponds to a low temperature gradient. A high heat capacity at constant pressure C_p indicates that the medium will store more heat for the same rise in temperature and thereby denotes a low temperature gradient. Thus, the ratio $\overline{\kappa}/\overline{C_p}$ which determines the temperature gradient is smaller for LSC_1 near the walls. Thus, it is expected that the thermal boundary layer will be thinner for LSC_1 which results in a higher temperature gradient and turbulent heat flux near the walls. This is indeed found to be the case, as shown in figure 4.23. Thus, it is concluded that the presence of variable transport properties in the case LSC_1 enhances the turbulent heat flux near the walls and suppresses it near the center of the channel compared to SCCTP. This same behaviour is again confirmed on comparing the productions for turbulent heat flux for the cases LSC_1 and SCCTP, as shown in the figure 4.23(c).

Quadrant analysis of the turbulent heat flux contingent on Favre averaged velocity and internal energy fluctuations is performed for LSC_1 and SCCTP. The contributions of the four quadrants are shown in the figure 4.24. The two quadrants which contribute in the direction of the turbulent heat flux are seen to be quadrant (Q_{II}) ($v'' >, h'' < 0$) and quadrant (Q_{III}) ($v'' < 0, h'' > 0$). The quadrants which contribute in the opposite direction of turbulent heat flux are the quadrants (Q_I) and (Q_{IV}) represented by the conditions ($v'' > , h'' > 0$) and ($v'' <, h'' < 0$), respectively. In all the quadrants, it is seen that the turbulent heat flux is enhanced near the walls and suppressed near the center of the channel for LSC_1 compared to SCCTP. Also, near the cold walls, the biggest contribution is seen to be from quadrant Q_{II}. This indicates that, near the cold wall, the turbulent heat flux is generated mainly due to the injection of cold fluids from the walls towards the center of the channel. Near the hot walls, the behaviour is seen to be just the opposite and the turbulent heat flux is generated mainly due to the injection of hot fluids from the walls towards the center of the channel. Thus, the quadrants Q_{II} and Q_{III} are almost mirror images of each other with respect to the center of the channel.

If we compare the turbulent heat fluxes scaled by the reference velocity for the higher Mach number cases HSC_1 and HSC_2 as shown in figure 4.25(b), it is seen that the heat flux distributions are not symmetric, in contrast to that for the low Mach number cases, as seen in figure 4.23(b). Thus, an increase in the Mach number disturbs the symmetry of turbulent heat flux generation. There is a peak on the cold side of the channel for both HSC_1 and HSC_2. The trans-critical transition very close to the cold wall for HSC_2

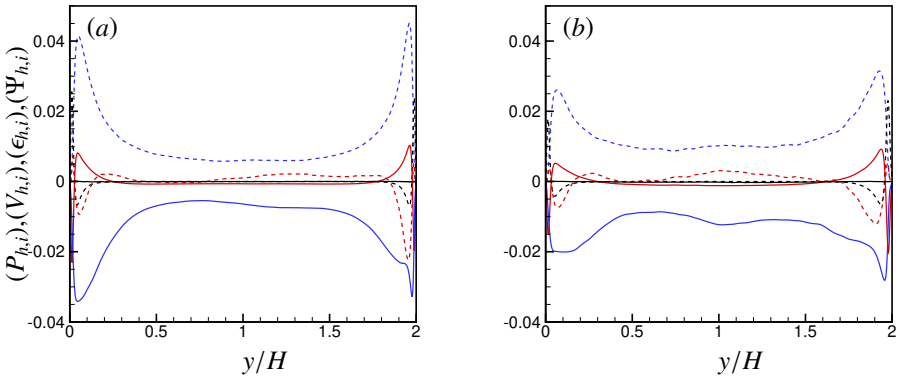

Figure 4.21: Turbulence heat flux budgets as a function of channel height. (– – –) $P_{h,i}$; (——) $\Psi_{h,i}$; (– – –) $V_{h,i}$; (——) $\epsilon_{h,i}$; (– – –) $\Gamma_{h,i}$; (——) Balance; (a) LSC_1; (b) SCCTP.

makes the gradient of temperature and internal energy minimal for the rest of the channel height. This is reflected in the peak for the Favre averaged internal energy fluctuation and the turbulent heat flux disappearing near the hot wall for the case HSC_2. The magnitude of the turbulent heat flux is also seen to decrease for HSC_2 indicating a reduction in the correlation between the fluctuating internal energy and the fluctuating velocity.

To conclude, it can be said that the turbulent heat flux budget equations are balanced for both the lower and higher Mach number cases. The major contributions to turbulent heat flux near the hot and cold walls comes from the injection of cold fluid from the wall to the centre near the cold wall and the injection of hot fluid from the wall to the centre near the hot wall. These are represented, respectively by the first quadrant (Q_I) and the third quadrant (Q_{III}), as given by quadrant analysis. The viscous dissipation is found to increase with the increase in Mach number. This disturbs the symmetry in the distribution of turbulent heat flux. The location of the point of trans-critical transition very close to the cold wall is found to result in the disappearance of the peak of turbulent heat flux dissipation near the hot wall. Thus, the turbulent heat flux distribution is influenced both by a change in the Mach number and the location of trans-critical transition.

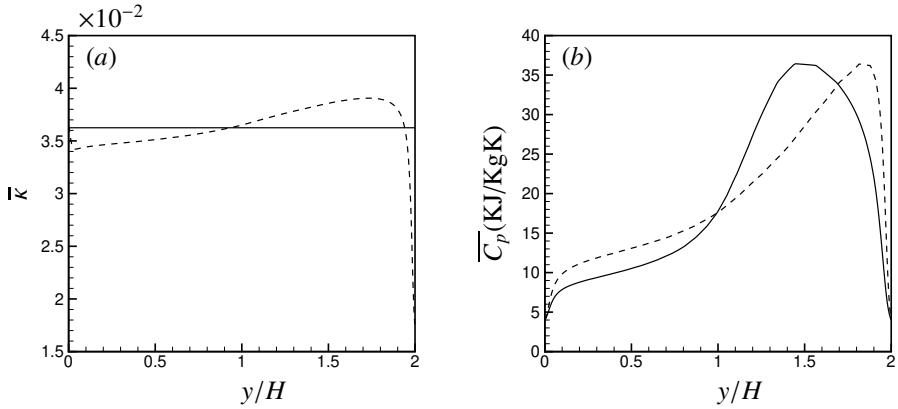

Figure 4.22: Thermal conductivity and heat capacity at constant pressure as a function of channel height. (———) SCCTP; (– – –) LSC_1.

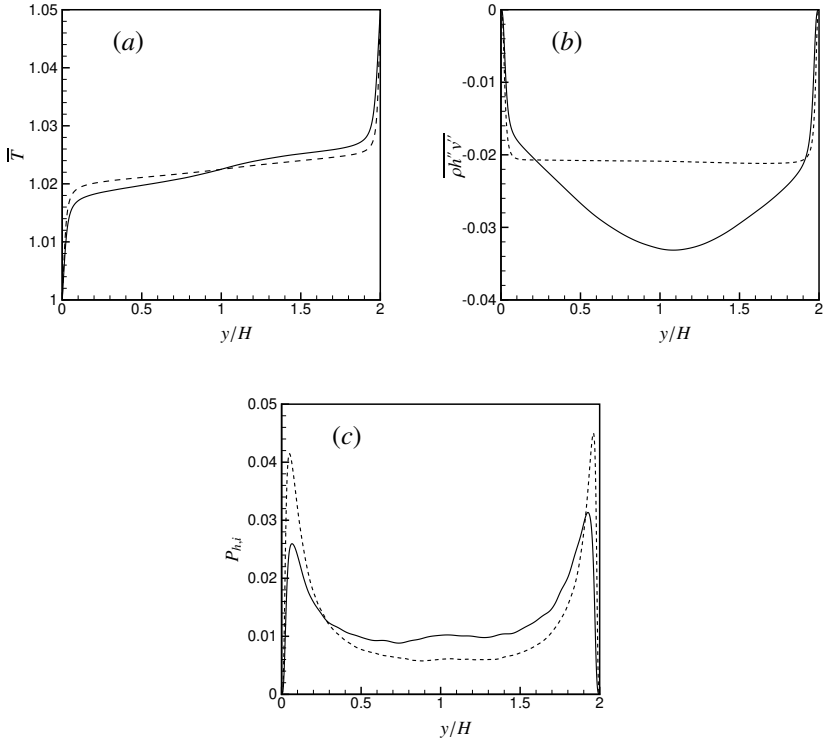

Figure 4.23: Average temperature and turbulent heat flux as a function of channel height. (———) SCCTP; (– – –) LSC_1.

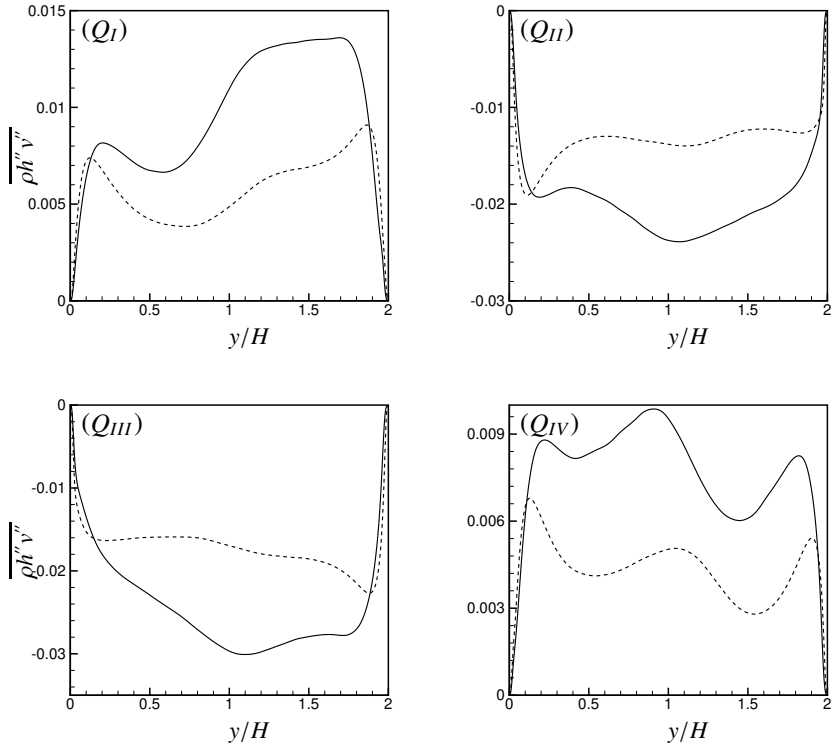

Figure 4.24: Quadrant analysis of turbulence heat flux in the wall normal direction as a function of channel height. (I) ($u'' > 0, h'' > 0$); (II) ($u'' > 0, h'' < 0$); (III) ($u'' < 0, h'' > 0$); (IV) ($u'' < 0, h'' < 0$); (———) SCCTP; (– – –) LSC_1

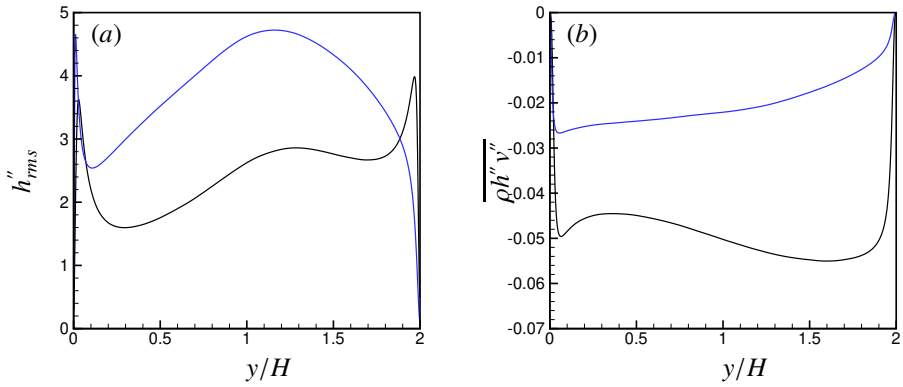

Figure 4.25: Favre averaged enthalpy fluctuations and turbulent heat flux as a function of channel height scaled by the bulk velocity. (——) HSC_1; (——) HSC_2.

5

Shock structure in Real gases including bulk viscosity.

5.1 Bulk Viscosity

The dynamics of fluid flows under most normal situations is a highly well explored area within the domain of classical physics. Fluid dynamics of flows under more extreme conditions, such as supersonic and hypersponic flows need a deeper investigation in order to understand the relationship between the continuum characteristics of the gas and its molecular structure. Fluid dynamics are described by the Navier-Stokes equations, which include a linear relationship between the deformation of a fluid element and the stress, where the constant of proportionality is referred to as the shear viscosity μ_s.

In 1845, Stokes introduced another coefficient λ in his seminal work "On the Theories of the Internal Friction of Fluids in Motion, and of the Equilibrium and Motion of Elastic Solids". This is also known as the second viscosity coefficient. In his work, Stokes formulated the law of viscous friction, which constitutes the backbone of modern fluid dynamics. This was initially aimed at explaining the phenomenon of the damping of a pendulum suspended in an "elastic fluid" for which no plausible explanation existed at that time. Stokes explained that internal friction in fluids may not only arise due to shear, but also due to molecular collisions and interactions in rapidly compressed fluids. The second viscosity coefficient was formulated as the constant of proportionality in order to substantiate this theory. Stokes believed that for fluids, the second viscosity coefficient might play a role in internal friction. But for the cases that he investigated, the second viscosity coefficient was not taken into consideration as the fluids were assumed to be incompressible for all practical purposes. This was called the Stokes' approximation.

The first and the second viscosity coefficients are commonly linked by the bulk viscosity according to the following relation

$$\mu_b = \lambda + \frac{2}{3}\mu_s. \tag{5.1}$$

The bulk viscosity μ_b appears in the momentum equation as $\nabla(\mu_b \nabla \cdot \mathbf{u})$, with $\mathbf{u}$ being the velocity vector. It also appears in the energy equation as $\mu_b(\nabla \cdot \mathbf{u})^2$, where it contributes to the viscous dissipation term. This has been mentioned by previous authors, such as Emanuel (1990). In fluid flows with vanishing dilatation represented by $\nabla \cdot \mathbf{u} \rightarrow 0$ or in flows of monatomic gases, the terms associated with bulk viscosity tend to vanish. However, in case of shock waves or strong heating in a turbulent flow for a gas with a high bulk viscosity, these assumptions are not valid.

5.2 Van der Waals Model

A shock wave is defined as a propagating disturbance through a medium, which is accompanied by sudden and nearly discontinuous changes in the pressure, density and temperature in the medium. The ideal gas model has been used extensively in order to study the features involving the propagation of shock waves through perfect gases. But, real gases exhibit features, which cannot be explained by the ideal gas equation of state. These include dense gases, such as perflurocarbons, hydrocarbons and siloxanes, which

have large heat capacities relative to their molecular weights. This is due to the high level of complexity in these molecules which increases the number of degrees of freedom leading to a corresponding increase in the heat capacity in accordance with the law of equipartition of energy. For these real gases, the speed of sound can decrease following a compression. Real gases also include the Bethe-Zeldovich-Thompson (BZT) gases, as mentioned in Alferez & Touber (2017) for which the isentropes can become locally concave in the pressure-volume diagram. Some of the phenomena experienced in case of shock waves in real gases and are not admissible for ideal gases are given as follows.

Rarefaction shocks are shock waves in which the density of the unperturbed or the pre-shock state is greater than that of the perturbed or the post-shock state. For ideal gases, only compression shock waves are admissible. But, for real gases, both compression are rarefaction shocks may be admissible or inadmissible depending on the shock strength and the characteristics of the pre shock state.This has been mentioned by previous authors, such as Zhao *et al.* (2011); Cramer & Sen (1987).

The shock splitting phenomenon occurs in real gases when an unstable shock decomposes into a combination of shock wave and rarefaction shocks. Phase transition induced by a shock takes place in real gases when the unperturbed and perturbed states of a shock are in different phases. This includes the phenomenon of a liquefaction shock wave. These are also mentioned in Zhao *et al.* (2011).

Thus, it is seen that shock waves for real gases can include a scope for a much wider analysis than available in the case of ideal gases. The van der Waals model has been chosen to represent real gas behaviour and is represented in greater detail in the following section.

All the thermodynamic quantities should be expressed in terms of their reduced values as this allows us to use the law of corresponding states according to which the reduced properties of all fluids exhibit identical behaviour and are independent of the material dependent parameters a and b in the equation of state. The reduced density, pressure and temperature are defined as the ratio of these properties to their values under critical conditions. These are given as follows

$$\begin{aligned} \rho_r &= \frac{\rho}{\rho_{cr}}, \\ P_r &= \frac{P}{P_{cr}}, \\ T_r &= \frac{T}{T_{cr}}, \end{aligned} \tag{5.2}$$

where the subscript r is used to express reduced quantities. The thermodynamic properties at the critical conditions can be calculated from the van der Waals equation of state as

$$\begin{aligned} \rho_{cr} &= \frac{1}{3b}, \\ P_{cr} &= \frac{a}{27b^2}, \\ T_{cr} &= \frac{8a}{27Rb}. \end{aligned} \tag{5.3}$$

The reduced internal energy, entropy and speed of sound are defined as

$$\begin{aligned} e_r &= e\left(\frac{\rho_{cr}}{P_{cr}}\right), \\ c_r &= c\sqrt{\left(\frac{\rho_{cr}}{P_{cr}}\right)}, \\ S_r &= S\left(\frac{T_{cr}\rho_{cr}}{P_{cr}}\right). \end{aligned} \tag{5.4}$$

These are expressed in terms of reduced quantities as follows

$$\begin{aligned} e_r &= \frac{8}{3\delta}T_r - 3\rho_r, \\ P_r &= \frac{8T_r\rho_r}{3-\rho_r} - 3\rho_r^2, \\ c_r &= \sqrt{(1+\delta)\,\frac{3\,(P_r+3\rho_r^2)}{\rho_r\,(3-\rho_r)} - 6\rho_r}, \\ S_r &= \frac{8}{3}ln\left(K_r T^{1/\delta}\frac{3-\rho_r}{\rho_r}\right). \end{aligned} \tag{5.5}$$

It is well known that thermodynamic stability requires convexity in the $P-\rho$ space. This means that $(\partial P_r/\partial\rho_r)_{T_r} > 0$. This is the area outside the locus of points for which $(\partial P_r/\partial\rho_r)_{T_r} = 0$. These are called the spinodal curves and they are given by the points represented by the equation $P_r = \rho_r^2\,(3-2\rho_r)$ for pressures below the critical pressure.

There is another important curve called the coexistence curve on which the fluid undergoes isothermal phase transition at constant pressure P_{coe}. The density of the liquid and the gas at the beginning and the end of this process are given as ρ_L and ρ_G, respectively. The chemical potential $\mu_K = e - TS + P/\rho$ remains constant during this isothermal phase transition. The points of liquefaction and gasification are determined by equating the work done at constant pressure for isothermal phase transition to the pressure work performed in this this transition as derived from the van der Waals equation of state. This is given as

$$\int_{\vartheta_L}^{\vartheta_G}(Pd\vartheta) = \int_{\vartheta_L}^{\vartheta_G}(P_{coe}d\vartheta)\,, \tag{5.6}$$

where $\vartheta_L = 1/\rho_L$ and $\vartheta_G = 1/\rho_G$ represent the specific volume of the liquid and the gas, respectively. The region between the spinodal curves and the coexistence curve include the metastable liquid and the metastable gas regions. These features are all shown in Figure 5.1. The van der Waals model has been used to represent the shock structure for a one dimensional steady shock. This is explained in the following section.

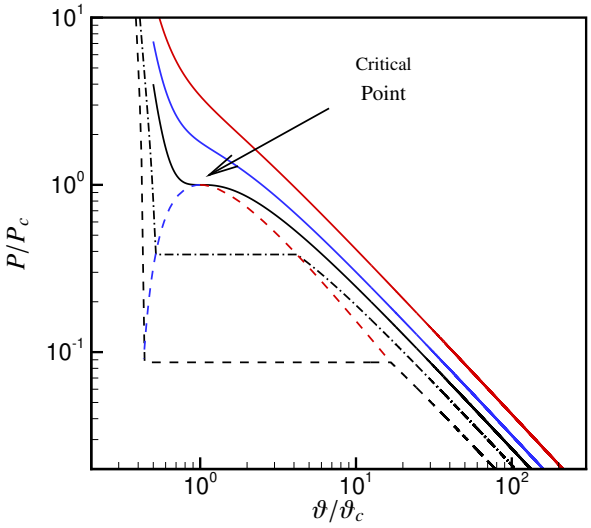

Figure 5.1: (– – –) $T/T_c = 0.6$, (—·—) $T/T_c = 0.8$, (——) $T/T_c = 1$, (——) $T/T_c = 1.2$, (——) $T/T_c = 1.6$, (– – –) Saturation liquid line, (– – –) Saturation vapour line.

5.3 Rankine-Hugoniot Conditions

The steady state one-dimensional Navier-Stokes equations in shocks are given by:

$$\frac{\partial(\rho u)}{\partial x} = 0, \tag{5.7}$$

$$\frac{\partial\left(\rho u^2 + P - \mu S_{xx}\right)}{\partial x} = 0, \tag{5.8}$$

$$\frac{\partial\left(\rho u\left(e_0 + \frac{P}{\rho}\right) - u\mu S_{xx}\right)}{\partial x} = \frac{\partial\left(\kappa\frac{\partial T}{\partial x}\right)}{\partial x}, \tag{5.9}$$

where ρ is the density, u is the velocity, P is the pressure, μ is the viscosity, S_{xx} is the strain, $e_0 = e + 1/2u^2$ is the total energy, e is the internal energy and κ is the thermal conductivity.

Utilizing the fact that the density and the velocity are non-dimensionalized by their initial values, we get,

$$\begin{aligned} \frac{\partial(\rho u)}{\partial x} &= 0, \\ \rho u = \rho_1 u_1 &= 1, \end{aligned} \tag{5.10}$$

where ρ_1, u_1 are the initial pre shock conditions for density and velocity.

The Navier-Stokes equations are given in the non conservative form as follows,

$$\frac{\partial u}{\partial x} + \frac{\partial P}{\partial x} = \frac{\partial (\mu S_{xx})}{\partial x}. \tag{5.11}$$

Integrating the momentum equation, we get,

$$\begin{aligned} \int_{-\infty}^{+\infty} \left(\frac{\partial u}{\partial x} + \frac{\partial P}{\partial x} - \frac{\partial (\mu S_{xx})}{\partial x} \right) dx = 0, \\ P_2 + \frac{1.0}{\rho_2} = P_1 + \frac{1.0}{\rho_1}, \end{aligned} \tag{5.12}$$

where P_1 and P_2 refer to the pre and post shock pressures and ρ_1 and ρ_2 refer to the pre and post shock densities.

Integrating the energy equation, we get,

$$\frac{\partial H}{\partial x} + \frac{\partial \left(1/2u^2\right)}{\partial x} = \frac{\partial (u\mu S_{xx})}{\partial x} + \frac{\partial \left(\kappa \frac{\partial T}{\partial x}\right)}{\partial x}. \tag{5.13}$$

$$\begin{aligned} \int_{-\infty}^{+\infty} \left(\frac{\partial H}{\partial x} + \frac{\partial \left(1/2u^2\right)}{\partial x} - \frac{\partial (u\mu S_{xx})}{\partial x} - \frac{\partial \left(\kappa \frac{\partial T}{\partial x}\right)}{\partial x} \right) = 0, \\ H_2 + \frac{1}{2\rho_2^2} = H_1 + \frac{1}{2\rho_2^2}. \end{aligned} \tag{5.14}$$

This gives the Rankine-Hugoniot conditions which are denoted by the following equations

$$\begin{aligned} P_2 + \frac{1}{\rho_2} = P_1 + \frac{1}{\rho_1}, \\ H_2 + \frac{1}{2\rho_2^2} = H_1 + \frac{1}{2\rho_1^2}. \end{aligned} \tag{5.15}$$

The Rankine Hugoniot conditions are used to determine the post shock conditions based on the pre shock density, temperature and Mach number. This is done using the van der Waals equation of state to calculate the pressure and the departure function for enthalpy, both of which are functions of the density and temperature and are given as follows

$$\begin{aligned} P = \frac{\rho RT}{1 - b\rho} - a\rho^2, \\ H = C_v T + \frac{P}{\rho} - a\rho, \end{aligned} \tag{5.16}$$

where $C_v = (f/2)R$ gives the ideal gas heat capacity at constant volume and f is the number of degrees of freedom of the gas molecule. The post shock conditions, such as density, temperature and pressure can be used to determine the Rankine line and the Hugoniot line on the $P - \vartheta$ plane.

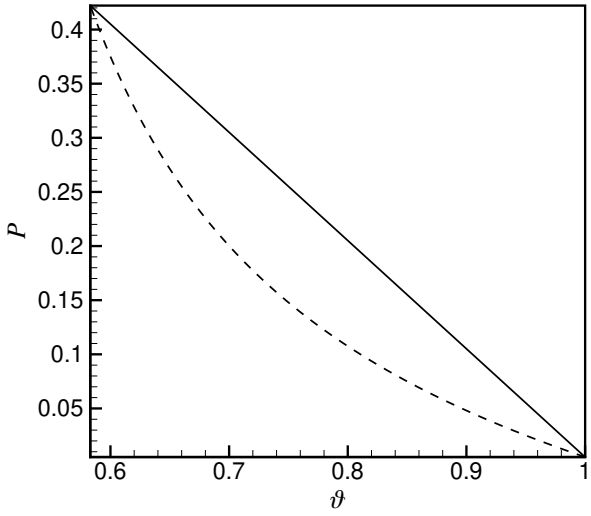

Figure 5.2: (———) Rankine Line, (– – –) Hugoniot Line.

The Rankine line is the solution to the following equations in the $P - \vartheta$ space within the range of the pre and post shock conditions

$$\begin{aligned} P_2 + \rho_2 u_2^2 &= P_1 + \rho_1 u_1^2, \\ P_2 &= P_1 - j^2 \left(\vartheta_2 - \vartheta_1\right), \\ j &= \rho u = \rho_1 u_1 = 1, \end{aligned} \tag{5.17}$$

where $\vartheta = 1/\rho$ is the specific volume and j is the non-dimensional mass flux.

The Hugoniot line is the solution to the following equations in the $P - \vartheta$ space within the range of the pre and post shock conditions

$$\begin{aligned} \rho u &= \rho_1 u_1 = 1, \\ H_2 &= H_1 + \frac{1}{2\rho_1^2} - \frac{1}{2\rho_2^2}. \end{aligned} \tag{5.18}$$

A similar derivation to the one given above has been performed in Chikitkin *et al.* (2015).

The shock is said to be admissible if the following conditions are satisfied

$$M_1 > 1 > M_2, \tag{5.19}$$

which indicates that the pre shock condition is supersonic and the post shock condition is subsonic and

$$S_2 - S_1 > 0, \tag{5.20}$$

which implies that there is entropy growth across the shock. These conditions are mentioned in Cramer & Sen (1987).

5.4 Shock structure of a van der Waals gas

Integrating the momentum equation from $-\infty$ to any location x, we get,

$$\int_{-\infty}^{x}\left(\frac{\partial u}{\partial \zeta}+\frac{\partial P}{\partial \zeta}-\frac{\partial\left(\mu S_{\zeta\zeta}\right)}{\partial \zeta}\right)d\zeta=0, \tag{5.21}$$

$$P-P_1+\frac{1}{\rho}-\frac{1}{\rho_1}=\mu S_{xx}, \tag{5.22}$$

$$\frac{\partial \rho}{\partial x}=\frac{\rho^2}{\frac{4}{3}\mu_s+\mu_b}\left(P-P_1+\frac{1}{\rho}-\frac{1}{\rho_1}\right). \tag{5.23}$$

The viscosity is given by $\mu = 4/3\mu_s+\mu_b$, where μ_s is the shear viscosity and μ_b is the bulk viscosity. Integrating the energy equation $-\infty$ to any location x, we get,

$$\int_{-\infty}^{x}\left(\frac{\partial H}{\partial \zeta}+\frac{\partial\left(1/2u^2\right)}{\partial \zeta}-\frac{\partial\left(u\mu S_{\zeta\zeta}\right)}{\partial \zeta}-\frac{\partial\left(\kappa\frac{\partial T}{\partial \zeta}\right)}{\partial \zeta}\right)=0, \tag{5.24}$$

$$H-H_1+\frac{1}{2\rho^2}-\frac{1}{2\rho_1^2}=\frac{1}{\rho}\left(\mu S_{xx}\right)+\kappa\frac{\partial T}{\partial x}. \tag{5.25}$$

Substituting μS_{xx} from equation 5.22,

$$\frac{\partial T}{\partial x}=\frac{\left(H-H_1+\frac{1}{2\rho^2}-\frac{1}{2\rho_1^2}+\frac{1}{\rho^3}\frac{\partial \rho}{\partial x}\right)}{\kappa}. \tag{5.26}$$

Thus, we derive that the following system of these two partial differential equations should be solved in order to determine the density and temperature inside the shock and thereby determine the shock thickness

$$\frac{\partial \rho}{\partial x}=\frac{\rho^2}{\frac{4}{3}\mu_s+\mu_b}\left(P-P_1+\frac{1}{\rho}-\frac{1}{\rho_1}\right), \tag{5.27}$$

$$\frac{\partial T}{\partial x}=\frac{\left(H-H_1+\frac{1}{2\rho^2}-\frac{1}{2\rho_1^2}+\frac{1}{\rho^3}\frac{\partial \rho}{\partial x}\right)}{\kappa}. \tag{5.28}$$

The pressure and enthalpy are functions of density and temperature as given by equation 5.16. The system of differential equations given above are solved for the

boundary conditions given by

$$\begin{aligned} \rho_{-\infty} &= \rho_1, \\ T_{-\infty} &= T_1, \\ P_{-\infty} &= P_1, \\ H_{-\infty} &= H_1, \end{aligned} \tag{5.29}$$

as given by the pre shock conditions and

$$\begin{aligned} \rho_{+\infty} &= \rho_2, \\ T_{+\infty} &= T_2, \\ P_{+\infty} &= P_2, \\ H_{+\infty} &= H_2, \end{aligned} \tag{5.30}$$

as determined from the Rankine-Hugoniot equations.

5.5 Significance of bulk viscosity in shocks

The van der Waals model as described above was used to investigate the shock structure for the following cases of supercritical carbon dioxide flows as given in table 5.1. The initial pre shock Mach number is 6.0 and the initial conditions are fixed at 80 bar and 300 K in all the 4 cases. So, the pre-shock condition relates to the supersonic flow of supercritical CO_2. The shear viscosity and thermal conductivities under the initial conditions are evaluated using the Refrop database, as mentioned in Lemmon *et al.* (2010). The ratio of bulk viscosity to shear viscosity in these 4 cases is increased from 1 to 1000 by a factor of 10. The Rankine-Hugoniot equations are used to first calculate the post shock temperature and density using the method mentioned above. The shock structures are then determined for all these cases by solving the system of partial differential equations, as given by 5.27 and 5.28. This enables us to determine the shock structure and to calculate the shock thickness. It is found that the shocks are admissible as the conditions of subsonic flow and increase in entropy in the post-shock environment, as given in the equations 5.19 and 5.20 are satisfied in all four cases. This is further evident from the fact that the Hugoniot line in found to be convex, as shown in the figure 5.2. The Rankine and the Hugoniot lines will be the same in all four cases along with the post-shock conditions. This is due to the fact that the Rankine line, the Hugoniot line and the post-shock conditions are not affected by a change in the viscosity. The shock structures for temperature and density normalized by their initial values are shown in the figures 5.4 and 5.3 respectively. It is seen that, in each case, an increase in the bulk viscosity by a factor of 10 radically alters the shock structure and increases shock thickness by almost the same order of magnitude. The viscosity and the thermal conductivity have been fixed at a constant value equal to the value under the initial conditions throughout the length of the shock for the purpose of convenience. In reality, this will not be the situation as the shear viscosity and thermal conductivity will also

Cases	P_1	T_1	Ma_1	μ_b/μ_s
S_1	80 bar	300 K	6.0	1
S_2	80 bar	300 K	6.0	10
S_3	80 bar	300 K	6.0	100
S_4	80 bar	300 K	6.0	1000

Table 5.1: Cases investigated for supercritical carbon dioxide at pre-shock conditions of 80 bar and 300 K and a pre shock Mach number of 6.0

vary with the change in the temperature and density. Thus, a logical extension to this work will be to incorporate the effects of the variation of shear viscosity and thermal conductivity across the shock with the help of a lookup table. The effects of the variation in bulk viscosity due to the changes in temperature and density can also be taken into account by using an appropriate model for bulk viscosity. Nevertheless, this work does provide a preliminary methodology to determine the shock thickness using a cubic equation of state. The van der Waals equation of state has been used here due to it's simplicity of form, but the analysis can easily be extended to other more complex cubic equations, such as Redlich Kwong and the Peng Robinson equation of state.

This analysis poses the question as to why the bulk viscosity was not taken into account while performing the DNS of supercritical CO_2 given in the previous chapters. This can be explained by the following reasons.

In our DNS simulations with supercritical CO_2, we have only investigated the subsonic range of flows. The increase in Mach number increases the pressure fluctuations for fully compressible flows. Therefore, for higher Mach numbers, it is essential that the mean pressure in the channel is increased so that the minimum pressures in the channel stay away from the 2 phase region. In order to get admissible shocks in our DNS simulations, the Mach number has to be increased to such an extent that the mean pressure in the channel would deviate far away from the vapour-liquid critical point in order to avoid the 2 phase region. This would defeat the purpose of performing DNS of CO_2 close to the critical point.

It is known that the bulk viscosity has to be multiplied to the dilatation in the fully compressible Navier-Stokes equations. It has been found that, in the cases that we have investigated, the dilatational field is negligible compared to the solenoidal field for most of the channel height.

Thus, it is seen that bulk viscosity has a substantial influence on the shock structure and its impact on turbulent flows of supercritical CO_2 should be taken into consideration. For our current simulations, the Mach numbers are not high enough to experience shocklets in the flow field. However, turbulent flows of supercritical CO_2 under supersonic or hypersonic conditions would experience shocklets in the flow field and, therefore, would possibly be impacted by bulk viscosity. If such simulations would be performed close to the vapour-liquid critical point of CO_2, then a part of the flow field

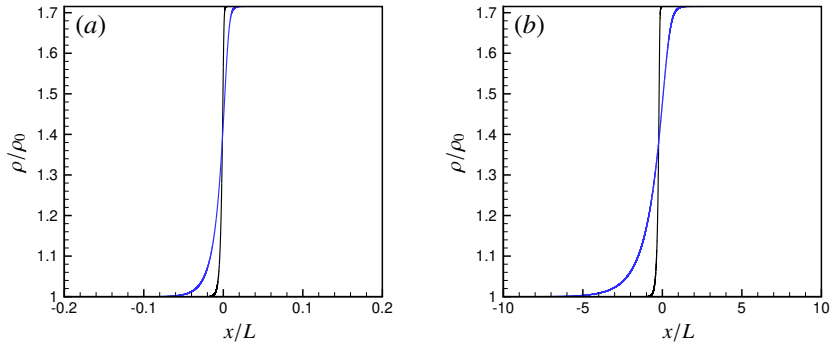

Figure 5.3: Density as a function of streamwise distance for a one dimensional steady state shock in presence of bulk viscosity. (a) (——) $\mu_b/\mu = 1$, (——) $\mu_b/\mu = 10$. (b) (——) $\mu_b/\mu = 100$, (——) $\mu_b/\mu = 1000$.

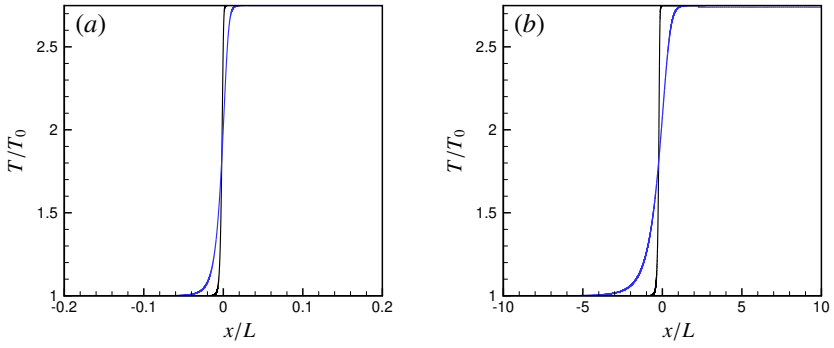

Figure 5.4: Temperature as a function of streamwise distance for a one dimensional steady state shock in presence of bulk viscosity. (a) (——) $\mu_b/\mu = 1$, (——) $\mu_b/\mu = 10$. (b) (——) $\mu_b/\mu = 100$, (——) $\mu_b/\mu = 1000$.

might also lie within the two-phase region large pressure fluctuations. A possible future investigation can be two-phase flows for CO_2 near the vapour-liquid critical point under supersonic or subsonic conditions. Under these conditions, comparison of the results from simulations that exclude and include bulk viscosity can provide an insight into the impact of bulk viscosity on turbulence and shock structure.

6

Conclusions and future directions

In the next section, the conclusions drawn from the research have been enunciated. Recommendations have also been made about the possible future directions in research in this field.

6.1 Conclusions

Fully compressible direct numerical simulations are performed for turbulent flows of supercritical CO_2 at low Mach numbers close to the vapour-liquid critical point involving trans-critical transition. The main conclusions from our research are as follows.

The location of trans-critical transition has an influence on the mean and turbulent statistics. Comparison of the mean temperature and the mean density profile for the cases LSC_1 and LSC_2 reveal significant differences. These are due to the changing nature of the density and the isobaric heat capacity for CO_2 due to the varying location of trans-critical transition. When the pseudo-critical temperature is located very close to the cold wall, it is seen to alter the traditional nature of turbulence. This is seen in the unusual nature of the density fluctuations for the case LSC_2 which is not observed in turbulent ideal gas flows with a wall temperature difference. The analysis of the streaks for density and temperature for LSC_2 also indicate that the cold wall region is characterized by much higher occurrences of high temperature and high density fluctuations than the region near the hot wall. The streamwise velocity streaks for LSC_2 near the hot and cold walls signify that high speed streaks are much more prevalent near the cold wall and also, the structures near the cold wall have a higher degree of coherence. A comparison of the high Mach number cases HSC_1 and HSC_2 with the corresponding lower Mach number cases reveals that, for HSC_1, the bulk temperature increases substantially compared to the bulk temperature in LSC_1. This is not found to be the case when the cases LSC_2 and HSC_2 are compared. The difference is caused due to the varying location of trans-critical transition and its effect on the Prandtl number profiles and the viscous heating terms. When the trans-critical transition happens very close to the cold wall, both the viscosity and the Prandtl number acquire a low constant value for most of the channel height. The result is low viscous heating and is manifested by only a small increase in the bulk temperature from LSC_2 to HSC_2. This is not the case in the cases LSC_1 and HSC_1 where the trans critical transition happens roughly in the middle of the channel.

A comparison of the semi-locally scaled solenoidal and total dissipation indicates that trans-critical transition very close to the wall can produce compressibility effects even at low Mach numbers. This is observed from the significant differences between solenoidal and total dissipation close to the cold wall for LSC_2. But, the compressibility effects in the overall perspective are quite small as these are only confined to a small part of the channel very close to the cold wall and also, for all the other simulations, they almost collapse on top of each other. The compressibility effects become even more accentuated for higher Mach number cases. A Helmholtz decomposition of the velocity field into the solenoidal and dilatational components reveal that, for the higher Mach number cases, the dilatational velocity has a more signficant contribution to the production, diffusion and

the dissipation of turbulent kinetic energy.

The change in the nature of the Re_τ^* profiles is has a significant impact on the redistribution of turbulent kinetic energy. This is evident in the fact that, on comparing the streamwise anisotropies on the hot and cold sides of the channel, the anisotropy is seen to increase when $dRe_\tau^*/dy < 0$ due to which there is a reduction in the redistribution of turbulent kinetic energy form the streamwise to the other directions. The opposite behaviour is observed when $dRe_\tau^*/dy > 0$. Thus, we can conclude that liquid-like behaviour which is characterized by an increasing Re_τ^* causes a decrease in the streamwise anisotropy and an increase in the spanwise anisotropy due to the increase in the turbulent kinetic energy redistribution from streamwise to the other directions, and the opposite is seen with gas-like behaviour.

The semi-locally scaled velocity fluctuations and turbulent kinetic energy budgets on the hot and cold sides of the channel are found to collapse almost on top of each other. This result is seen to reinforce Morkovin's hypothesis as it establishes that the changes in the turbulence structure are only caused by the change in the mean density gradients in the flow and the influence of density fluctuations on the changes in turbulence structures is insignificant.

The modelling of the pressure fluctuations indicates that, for the low Mach number cases, the RMS pressure fluctuation can be modelled based on the temperature and density profiles averaged in the streamwise and spanwise directions. It consists of the sum of the contributions from the ideal, attractive and the repulsive components. For the low Mach number cases, it is found that the magnitude of the RMS pressure fluctuation is negligible compared to the contributions from the individual components mentioned above. The same cannot be said of the higher Mach number cases, ie, in the higher Mach number cases, the density and temperature fluctuations also play a significant role in determining the pressure fluctuation which cannot be modelled based on the average temperature and density profiles.

The turbulent heat flux budget equations are seen to be balanced for both the lower and higher Mach number cases. Quadrant analysis of the turbulent heat flux shows that the main contribution to the turbulent heat flux near the hot and the cold walls comes from the first quadrant (Q_I) and the third quadrant (Q_{III}), respectively. These denote the injection of cold fluid from the wall to the centre near the cold wall and the injection of hot fluid from the wall to the centre near the hot wall. It is found that an increase in Mach number disturbs the symmetry in the turbulent heat flux distribution. This is due the influence of viscous dissipation. Also, the change in the location of trans-critical transition is found to drastically alter the profile of turbulent heat flux. If the location of trans-critical transition is located away from the walls, the distribution of the turbulent heat flux is found to have a peak near both walls. On the contrary, if the location of trans-critical transition is located very close to the cold wall, the peak of the turbulent heat flux near the hot wall is found to disappear. This proves that both the Mach number and the location of trans-critical transition affects the turbulent heat flux.

The effect of bulk viscosity on the shock structure of supercritical CO_2 under the pre-shock conditions of a Mach number of 6.0, a temperature of 300 K and a pressure of 80 bar. As the ratio of bulk to shear viscosity is raised from 1 to 1000 by factors of 10, it is

seen that this increase in bulk viscosity increases the shock thickness by the same order of magnitude.

6.2 Recommendations for future work

This research can be further expanded in order to perform simulations for different geometries and wall boundary conditions:

- **Turbulent flows in pipe or annulus geometry** Fully compressible turbulent flows of supercritical fluids can be investigated in pipe or annulus geometries which are more applicable to situations prevailing in the industry.
- **Adiabatic wall boundary condition** One of the important questions to consider is the effect of compressibility and location of trans-critical transition if one of the walls is adiabatic instead of isothermal. The effect of either the cold or the hot wall being made adiabatic needs to be investigated.
- **Conjugate heat transfer.** More realistic situations include thick walls, so the effects of wall thickness and thermal effusivity ratios on fully compressible flows should be considered.
- **Shock structure for real gases** In our investigation, the van der Waals model has been used to study the shock structure for real gases. However, more complex real gas models, such as Redlich Kwong and Peng Robinson equations of state can be used to study the effect of bulk viscosity on the shock structure of real gases. Also, the effects of the variation of shear viscosity and thermal conductivity with the change of temperature and density can be taken into account by loading these transport properties into the solver for a range of temperatures and densities with the help of a look-up table. Also, instead of keeping the bulk viscosity fixed, an appropriate model can be used to calculate the values of bulk viscosity as a function of temperature and density within the width of the shock.

Appendix A

Validation of the fully compressible Navier Stokes solver

The compressible Navier-Stokes code has been validated with the data published by previous authors for both low Mach number (Kim *et al.* (1987)) and high Mach number (Coleman *et al.* (1995)) cases. This is shown in the figures 1 and 2 with the help of both mean and turbulent statistics. The low Mach number and high Mach number cases used for validating the code are henceforth referred to as KMM and CKM, respectively. The corresponding simulations carried out with our present code are called Ma0.2 and Ma1.5. The details of these simulations are given in Table 1. The plots in figures 1 and 2 show a fairly good agreement for the mean flow profiles, the turbulent velocity fluctuations and the Reynolds shear stress with the data published by previous authors.

Table 1: Validation of the code for low and high Mach number cases; Ma: Mach number; Re: bulk Reynolds number; Re_τ: friction Reynolds number at the wall; Pr: Prandtl number; N_x,N_y,N_z: number of grid points; L_x,L_y,L_z: lengths of channel

Case	Ma	Re	Re_τ	Pr	$N_x \times N_y \times N_z$	$L_x \times L_y \times L_z$
KMM	0.0	2800	178	0.7	$192 \times 129 \times 160$	$4\pi h \times 2h \times \frac{4}{3}\pi h$
CKM	1.5	3000	222	0.7	$144 \times 119 \times 80$	$4\pi h \times 2h \times \frac{4}{3}\pi h$
Ma0.2	0.2	2800	180	0.7	$120 \times 168 \times 120$	$4\pi h \times 2h \times 2\pi h$
Ma1.5	1.5	3000	209	0.7	$120 \times 168 \times 120$	$4\pi h \times 2h \times 2\pi h$

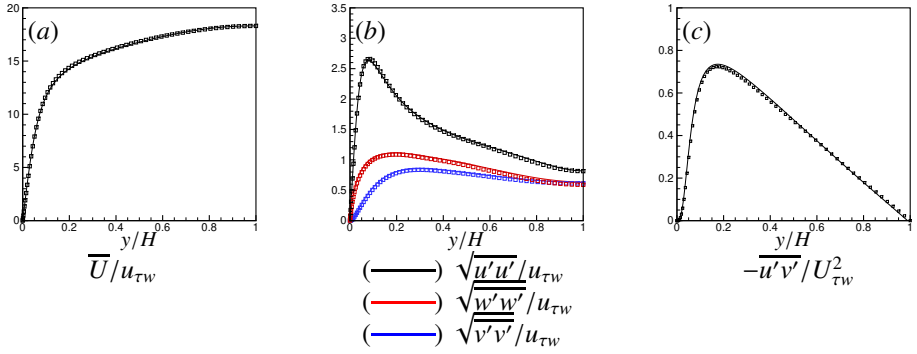

Figure 1: Validation of the compressible DNS code (Kim *et al.* (1987)); Lines: present; Symbols: KMM.

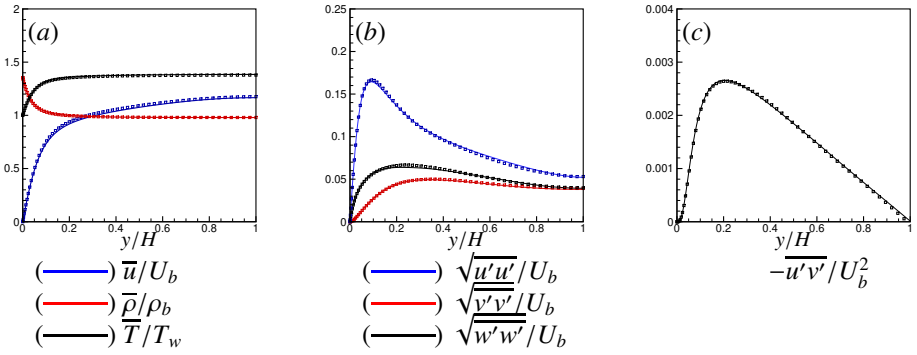

Figure 2: Validation of the compressible DNS code (Coleman *et al.* (1995)); Lines: present; Symbols: CKM.

Appendix B

Derivation of the turbulent heat flux budget equations

The fully compressible Navier Stokes equations for conservation of mass, momentum and internal energy are given as:

$$\frac{\partial \rho}{\partial t} + \frac{\partial \left(\rho u_j\right)}{\partial x_j} = 0 \tag{1}$$

$$\frac{\partial \left(\rho u_i\right)}{\partial t} + \frac{\partial \left(\rho u_i u_j + P\delta_{ij} - \Gamma_{ji}\right)}{\partial x_j} = 0 \tag{2}$$

$$\frac{\partial \rho e}{\partial t} + \frac{\partial \left(\rho u_j e + u_j P + q_j - u_k \Gamma_{kj}\right)}{\partial x_j} - u_j \frac{\partial P}{\partial x_j} + u_k \frac{\partial \Gamma_{kj}}{\partial x_j} = 0 \tag{3}$$

, where $e = h - P/\rho$ is the internal energy and h is the enthalpy. The energy equation written in terms of enthalpy is given as:

$$\frac{\partial \rho h}{\partial t} + \frac{\partial \left(\rho u_j h + q_j - u_k \Gamma_{kj}\right)}{\partial x_j} + u_k \frac{\partial \Gamma_{kj}}{\partial x_j} = \left(\frac{\partial P}{\partial t} + u_j \frac{\partial P}{\partial x_j}\right) \tag{4}$$

The material derivative of pressure on the right hand side can be neglected for open systems, as mentioned in Nicoud (2000). Thus, we get that the energy equation represented in terms of enthalpy is given as

$$\frac{\partial \rho h}{\partial t} + \frac{\partial \left(\rho u_j h + q_j - u_k \Gamma_{kj}\right)}{\partial x_j} + u_k \frac{\partial \Gamma_{kj}}{\partial x_j} = 0 \tag{5}$$

Converting the momentum and energy equations into the nonconservative form, we get,

$$\frac{\partial \rho}{\partial t} + \frac{\partial \left(\rho u_j\right)}{\partial x_j} = 0 \tag{6}$$

$$\rho\frac{\partial u_i}{\partial t}+\rho u_j\frac{\partial u_i}{\partial x_j}+\frac{\partial\left(P\delta_{ij}-\Gamma_{ji}\right)}{\partial x_j}=0 \tag{7}$$

$$\rho\frac{\partial h}{\partial t}+\rho u_j\frac{\partial h}{\partial x_j}+\frac{\partial\left(q_j-u_k\Gamma_{kj}\right)}{\partial x_j}+u_k\frac{\partial\Gamma_{kj}}{\partial x_j}=0 \tag{8}$$

Multiplying the continuity equation by $h^{''}u_i^{''}$, the momentum equation by $h^{''}$ and the energy equation by $u_i^{''}$, and by taking the Reynolds average, we get,

$$\overline{h^{''}u_i^{''}\frac{\partial\rho}{\partial t}}+\overline{h^{''}u_i^{''}\frac{\partial\left(\rho u_j\right)}{\partial x_j}}=0 \tag{9}$$

$$\overline{h^{''}\rho\frac{\partial u_i}{\partial t}}+\overline{h^{''}\rho u_j\frac{\partial u_i}{\partial x_j}}+\overline{h^{''}\frac{\partial\left(P\delta_{ij}-\Gamma_{ji}\right)}{\partial x_j}}=0 \tag{10}$$

$$\overline{u_i^{''}\rho\frac{\partial h}{\partial t}}+\overline{u_i^{''}\rho u_j\frac{\partial h}{\partial x_j}}+\overline{u_i^{''}\frac{\partial\left(q_j-u_k\Gamma_{kj}\right)}{\partial x_j}}+\overline{u_i^{''}u_k\frac{\partial\Gamma_{kj}}{\partial x_j}}=0 \tag{11}$$

where X'' refers to the Favre averaged fluctuations for any physical quantity X.

Now, adding the above three equations, we get,

$$\begin{aligned}\overline{\frac{\partial\rho h^{''}u_i^{''}}{\partial t}}+\overline{\frac{\partial\left(\rho u_j h^{''}u_i^{''}\right)}{\partial x_j}}+\overline{h^{''}\left(\rho u_j\right)\frac{\partial\widetilde{u_i}}{\partial x_j}}+\overline{u_i^{''}\left(\rho u_j\right)\frac{\partial\widetilde{h}}{\partial x_j}}+\overline{h^{''}\frac{\partial\left(P\delta_{ij}-\Gamma_{ji}\right)}{\partial x_j}}\\ +\overline{u_i^{''}\frac{\partial\left(q_j-u_k\Gamma_{kj}\right)}{\partial x_j}}+\overline{u_i^{''}u_k\frac{\partial\Gamma_{kj}}{\partial x_j}}=0\end{aligned} \tag{12}$$

With the help of Favre averaging, we get the following expressions

$$\frac{\partial\overline{\left(\rho u_j h^{''}u_i^{''}\right)}}{\partial x_j}=\frac{\partial\overline{\left(\rho\widetilde{u_j}h^{''}u_i^{''}\right)}}{\partial x_j}+\frac{\partial\overline{\left(\rho u_j^{''}h^{''}u_i^{''}\right)}}{\partial x_j} \tag{13}$$

$$\begin{aligned}\overline{h^{''}\left(\rho u_j\right)}\frac{\partial\widetilde{u_i}}{\partial x_j}=\overline{h^{''}\left(\rho\widetilde{u_j}\right)}\frac{\partial\widetilde{u_i}}{\partial x_j}+\overline{h^{''}\left(\rho u_j^{''}\right)}\frac{\partial\widetilde{u_i}}{\partial x_j}=\\ \overline{\rho h^{''}}\widetilde{u_j}\frac{\partial\widetilde{u_i}}{\partial x_j}+\overline{h^{''}\left(\rho u_j^{''}\right)}\frac{\partial\widetilde{u_i}}{\partial x_j}=\overline{h^{''}\left(\rho u_j^{''}\right)}\frac{\partial\widetilde{u_i}}{\partial x_j}\end{aligned} \tag{14}$$

$$\overline{u_i^{''}\left(\rho u_j\right)}\frac{\partial\widetilde{h}}{\partial x_j} = \overline{u_i^{''}\left(\rho u_j^{''}\right)}\frac{\partial\widetilde{h}}{\partial x_j} \tag{15}$$

$$-\overline{u_i^{''}\frac{\partial\left(u_k\Gamma_{kj}\right)}{\partial x_j}} + \overline{u_i^{''}u_k\frac{\partial\Gamma_{kj}}{\partial x_j}} = -\overline{u_i^{''}\Gamma_{kj}\frac{\partial u_k}{\partial x_j}} \tag{16}$$

$$\begin{aligned}\overline{h^{''}\frac{\partial\left(P\delta_{ij}-\Gamma_{ji}\right)}{\partial x_j}} + \overline{u_i^{''}\frac{\partial q_j}{\partial x_j}} = &\left(-\overline{\frac{\partial\left(h^{''}\Gamma_{ij}\right)}{\partial x_j}} + \overline{\frac{\partial\left(u_i^{''}q_j\right)}{\partial x_j}}\right)\\ &+\left(\overline{\Gamma_{ij}\frac{\partial h^{''}}{\partial x_j}} - \overline{q_j\frac{\partial u_i^{''}}{\partial x_j}}\right) + \overline{h^{''}\frac{\partial\left(P\delta_{ij}\right)}{\partial x_j}}\end{aligned} \tag{17}$$

The other terms vanish as, by definition $\overline{\rho X^{''}} = 0$ for any physical quantity X. Substituting all the above expressions, we get,

$$\begin{aligned}&\overline{\frac{\partial\left(\rho h^{''}u_i^{''}\right)}{\partial t}} + \overline{\frac{\partial\left(\rho\widetilde{u}_j h^{''}u_i^{''}\right)}{\partial x_j}} + \overline{\frac{\partial\left(\rho u_j^{''}h^{''}u_i^{''}\right)}{\partial x_j}} + \overline{h^{''}\rho u_j^{''}}\frac{\partial\widetilde{u}_i}{\partial x_j} + \overline{u_i^{''}\rho u_j^{''}}\frac{\partial\widetilde{h}}{\partial x_j}\\ &+\left(\overline{\frac{\partial\left(u_i^{''}q_j\right)}{\partial x_j}} - \overline{\frac{\partial\left(h^{''}\Gamma_{ij}\right)}{\partial x_j}}\right) + \left(\overline{\Gamma_{ij}\frac{\partial h^{''}}{\partial x_j}} - \overline{q_j\frac{\partial u_i^{''}}{\partial x_j}}\right) + \overline{h^{''}\frac{\partial\left(P\delta_{ij}\right)}{\partial x_j}} - \overline{u_i^{''}\Gamma_{kj}\frac{\partial u_k}{\partial x_j}} = 0\end{aligned} \tag{18}$$

These terms are represented as:

$$C_{h,i} = \overline{\frac{\partial\left(\rho\widetilde{u}_j h^{''}u_i^{''}\right)}{\partial x_j}}, T_{h,i} = \overline{\frac{\partial\left(\rho u_j^{''}h^{''}u_i^{''}\right)}{\partial x_j}}, P_{h,i} = \overline{h^{''}\rho u_j^{''}}\frac{\partial\widetilde{u}_i}{\partial x_j} + \overline{u_i^{''}\rho u_j^{''}}\frac{\partial\widetilde{h}}{\partial x_j} \tag{19}$$

$$V_{h,i} = \left(\overline{\frac{\partial\left(u_i^{''}q_j\right)}{\partial x_j}} - \overline{\frac{\partial\left(h^{''}\Gamma_{ij}\right)}{\partial x_j}}\right), \epsilon_{h,i} = \left(\overline{\Gamma_{ij}\frac{\partial h^{''}}{\partial x_j}} - \overline{q_j\frac{\partial u_i^{''}}{\partial x_j}}\right) \tag{20}$$

$$\Psi_{h,i} = \overline{h^{''}\frac{\partial\left(P\delta_{ij}\right)}{\partial x_j}}, W_{h,i} = -\overline{u_i^{''}\Gamma_{kj}\frac{\partial u_k}{\partial x_j}} \tag{21}$$

, where $C_{h,i}$ is the mean convection;$T_{h,i}$ is the turbulence diffusion;$P_{h,i}$ is the production; $V_{h,i}$ is the molecular diffusion; $\epsilon_{h,i}$ is the dissipation; $\Psi_{h,i}$ is the correlation between pressure gradient and fluctuating enthalpy and $W_{h,i}$ is the transport of the viscous dissipation by fluctuating velocity.

References

Adebiyi, G. & Hall, W. 1976 Experimental investigation of heat transfer to supercritical pressure carbon dioxide in a horizontal pipe. *International Journal of Heat and Mass Transfer* **19** (7), 715–720.

Alferez, N. & Touber, E. 2017 One-dimensional refraction properties of compression shocks in non-ideal gases. *Journal of Fluid Mechanics* **814**, 185–221.

Bae, J. H., Yoo, J. Y. & Choi, H. 2005 Direct numerical simulation of turbulent supercritical flows with heat transfer. *Physics of Fluids* **17**, 105104.

Bae, J. H., Yoo, J. Y. & McEligot, D. M. 2008 Direct numerical simulation of heated CO_2 flows at supercritical pressure in a vertical annulus at Re= 8900. *Physics of Fluids* **20**, 055108.

Battista, F., Picano, F. & Casciola, C. M. 2014 Turbulent mixing of a slightly supercritical van der waals fluid at low-mach number. *Physics of Fluids* **26** (5), 055101.

Blaisdell, G., Spyropoulos, E. & Qin, J. 1996 The effect of the formulation of nonlinear terms on aliasing errors in spectral methods. *Applied Numerical Mathematics* **21** (3), 207–219.

Boersma, B. 2011 A 6th order staggered compact finite difference method for the incompressible navier–stokes and scalar transport equations. *Journal of Computational Physics* **230** (12), 4940–4954.

Brunner, G. 2010 Applications of supercritical fluids. *Annual review of chemical and biomolecular engineering* **1**, 321–342.

Butcher, J. C. 2016 *Numerical methods for ordinary differential equations*. John Wiley & Sons.

Canuto, C., Hussaini, M., Quarteroni, A., Thomas Jr, A. *et al.* 2012 *Spectral methods in fluid dynamics*. Springer Science & Business Media.

Chikitkin, A., Rogov, B., Tirsky, G. & Utyuzhnikov, S. 2015 Effect of bulk viscosity in supersonic flow past spacecraft. *Applied Numerical Mathematics* **93**, 47–60.

Coleman, G., Kim, J. & Moser, R. 1995 A numerical study of turbulent supersonic isothermal-wall channel flow. *Journal of Fluid Mechanics* **305**, 159–183.

Cramer, M. S. & Sen, R. 1987 Exact solutions for sonic shocks in van der waals gases. *The Physics of fluids* **30** (2), 377–385.

Dostal, V., Hejzlar, P. & Driscoll, M. J. 2006 The supercritical carbon dioxide power cycle: comparison to other advanced power cycles. *Nuclear technology* **154** (3), 283–301.

Elliott, J. & Lira, C. 1999 *Introductory chemical engineering thermodynamics*. Prentice Hall PTR Upper Saddle River, NJ.

Emanuel, G. 1990 Bulk viscosity of a dilute polyatomic gas. *Physics of Fluids A: Fluid Dynamics* **2** (12), 2252–2254.

Fenghour, A., Wakeham, W. A. & Vesovic, V. 1998 The viscosity of carbon dioxide. *Journal of Physical and Chemical Reference Data* **27** (1), 31–44.

Foysi, H., Sarkar, S. & Friedrich, R. 2004 Compressibility effects and turbulence scalings in supersonic channel flow. *Journal of Fluid Mechanics* **509**, 207–216.

French, D. 1998 1997 kyoto protocol to the 1992 un framework convention on climate change. *Journal of Environmental Law* **10** (2), 227–239.

Friend, D., Ely, J. & Ingham, H. 1989 Thermophysical properties of methane. *Journal of Physical and Chemical Reference Data* **18** (2), 583–638.

Friend, D., Ingham, H. & Fly, J. 1991 Thermophysical properties of ethane. *Journal of physical and chemical reference data* **20** (2), 275–347.

Gerolymos, G. & Vallet, I. 2014 Pressure, density, temperature and entropy fluctuations in compressible turbulent plane channel flow. *Journal of Fluid Mechanics* **757**, 701–746.

Ghajar, A. & Asadi, A. 1986 Improved forced convective heat-transfer correlations for liquids in the near-critical region. *AIAA journal* **24** (12), 2030–2037.

Gottlieb, S. & Shu, C. 1998 Total variation diminishing runge-kutta schemes. *Mathematics of computation of the American Mathematical Society* **67** (221), 73–85.

Hall, W. & Jackson, J. 1969 Laminarization of a turbulent pipe flow by buoyancy forces. In *ASME*.

Hiroaki, T., Niichi, N., Masaru, H. & Ayao, T. 1971 Forced convection heat transfer to fluid near critical point flowing in circular tube. *International Journal of Heat and Mass Transfer* **14** (6), 739–750.

Huang, P. G., Coleman, G. N. & Bradshaw, P. 1995 Compressible turbulent channel flows: DNS results and modelling. *Journal of Fluid Mechanics* **305** (1), 185–218.

Joseph, D. 2006 Helmholtz decomposition coupling rotational to irrotational flow of a viscous fluid. *Proceedings of the National Academy of Sciences* **103** (39), 14272–14277.

Kawai, S., Terashima, H. & Negishi, H. 2015 A robust and accurate numerical method for transcritical turbulent flows at supercritical pressure with an arbitrary equation of state. *Journal of Computational Physics* **300**, 116–135.

Kim, J., Moin, P. & Moser, R. 1987 Turbulence statistics in fully developed channel flow at low reynolds number. *Journal of Fluid Mechanics* **177**, 133–166.

Krasnoshchekov, E., Kuraeva, I. & Protopopov, V. 1969 Local heat transfer of carbon dioxide at supercritical pressure under cooling conditions. *High Temperature* **7** (5), 856–+.

Krasnoshchekov, E. & Protopopov, V. 1966 Experimental study of heat exchange in carbon dioxide in the supercritical range at high temperature drops(heat transfer in turbulent carbon dioxide pipeflow at supercritical region). *High Temperature* **4**, 375–382.

Kreuzinger, J., Friedrich, R. & Gatski, T. B. 2006 Compressibility effects in the solenoidal dissipation rate equation: A priori assessment and modeling. *International journal of heat and fluid flow* **27** (4), 696–706.

Kunz, O., Klimeck, R., Wagner, W. & Jaeschke, M. 2007 The gerg-2004 wide-range reference equation of state for natural gases. *European Gas Reserach Group (Groupe Européen de Recherches Gazières) Technical Monograph* **15**.

Kunz, O. & Wagner, W. 2012 The gerg-2008 wide-range equation of state for natural gases and other mixtures: an expansion of gerg-2004. *Journal of chemical & engineering data* **57** (11), 3032–3091.

Kupka, F., Happenhofer, N., Higueras, I. & Koch, O. 2012 Total-variation-diminishing implicit–explicit runge–kutta methods for the simulation of double-diffusive convection in astrophysics. *Journal of Computational Physics* **231** (9), 3561–3586.

Lee, J., Yoon Jung, S., Jin Sung, H. & Zaki, T. A. 2013 Effect of wall heating on turbulent boundary layers with temperature-dependent viscosity. *Journal of Fluid Mechanics* **726**, 196–225.

Lele, S. 1994 Compressibility effects on turbulence. *Annual review of fluid mechanics* **26** (1), 211–254.

Lele, S. K. 1992 Compact finite difference schemes with spectral-like resolution. *Journal of computational physics* **103** (1), 16–42.

Lemmon, E. W., Huber, M. L. & McLinden, M. O. 2002 NIST reference fluid thermodynamic and transport properties–refprop.

Lemmon, E. W., Huber, M. L. & McLinden, M. O. 2010 NIST Standard ReferenceDatabase 23: Reference Fluid Thermodynamic and Transport Properties - REFPROP. 9.0.

Levelt, J. 1970 Scaling predictions for thermodynamic anomalies near the gas-liquid critical point. *Industrial & Engineering Chemistry Fundamentals* **9** (3), 470–480.

Li, N. & Laizet, S. 2010 2DECOMP&FFT–a highly scalable 2d decomposition library and FFT interface. In *Cray User Group 2010 conference*, pp. 1–13.

Miyamoto, H. & Watanabe, K. 2000 A thermodynamic property model for fluid-phase propane. *International journal of thermophysics* **21** (5), 1045–1072.

Miyamoto, H. & Watanabe, K. 2001 Thermodynamic property model for fluid-phase n-butane. *International journal of thermophysics* **22** (2), 459–475.

Miyamoto, H. & Watanabe, K. 2002 A thermodynamic property model for fluid-phase isobutane. *International journal of thermophysics* **23** (2), 477–499.

Morinishi, Y. 2010 Skew-symmetric form of convective terms and fully conservative finite difference schemes for variable density low-mach number flows. *Journal of Computational Physics* **229** (2), 276 – 300.

Morinishi, Y., Tamano, S. & Nakabayashi, K. 2004 Direct numerical simulation of compressible turbulent channel flow between adiabatic and isothermal walls. *Journal of Fluid Mechanics* **502**, 273–308.

Müller, H., Niedermeier, C., Matheis, J., Pfitzner, M. & Hickel, S. 2016 Large-eddy simulation of nitrogen injection at trans-and supercritical conditions. *Physics of Fluids* **28** (1), 015102.

Nemati, H., Patel, A., Boersma, B. & Pecnik, R. 2015 Mean statistics of a heated turbulent pipe flow at supercritical pressure. *International Journal of Heat and Mass Transfer* **83**, 741–752.

Nemati, H., Patel, A., Boersma, B. J. & Pecnik, R. 2016 The effect of thermal boundary conditions on forced convection heat transfer to fluids at supercritical pressure. *Journal of Fluid Mechanics* **800**, 531–556.

Nicoud, F. 2000 Conservative high-order finite-difference schemes for low-mach number flows. *Journal of Computational Physics* **158** (1), 71–97.

Oberthür, S. & Ott, H. 1999 *The Kyoto Protocol: international climate policy for the 21st century*. Springer Science & Business Media.

Onnes, H. 1901 Expression of the equation of state of gases and liquids by means of series. In *KNAW, Proceedings*, , vol. 4, pp. 1901–1902.

Pachauri, R., Allen, M., Barros, V., Broome, J., Cramer, W., Christ, R., Church, J., Clarke, L., Dahe, Q., Dasgupta, P. *et al.* 2014 *Climate change 2014: synthesis report. Contribution of Working Groups I, II and III to the fifth assessment report of the Intergovernmental Panel on Climate Change*. IPCC.

Patel, A., Boersma, B. & Pecnik, R. 2016 The influence of near-wall density and viscosity gradients on turbulence in channel flows. *Journal of Fluid Mechanics* **809**, 793–820.

Patel, A., Peeters, J., Boersma, B. & Pecnik, R. 2015 Semi-local scaling and turbulence modulation in variable property turbulent channel flows. *Physics of Fluids (1994-present)* **27** (9), 095101.

Peeters, J., Pecnik, R., Rohde, M., van der Hagen, T. & Boersma, B. 2017 Characteristics of turbulent heat transfer in an annulus at supercritical pressure. *Physical Review Fluids* **2** (2), 024602.

Peng, D. & Robinson, D. 1976 A new two-constant equation of state. *Industrial & Engineering Chemistry Fundamentals* **15** (1), 59–64.

Petukhov, B., Krasnoshchekov, E. & Protopopov, V. 1961 An investigation of heat transfer to fluids flowing in pipes under supercritical conditions. *ASME International Developments in Heat Transfer Part* **3**, 569–578.

Petukhov, B. & Polyakov, A. 1974 Boundaries of regimes with"worsened"heat transfer for supercritical pressure of coolant. *Tech. Rep.*. Institute of High Temperatures, Academy of Sciences of the USSR.

Poling, B., Prausnitz, J., O'connell, J. *et al.* 2001 *The properties of gases and liquids*, , vol. 5. Mcgraw-hill New York.

Redlich, O. & Kwong, J. 1949 On the thermodynamics of solutions. v. an equation of state. fugacities of gaseous solutions. *Chemical reviews* **44** (1), 233–244.

Rinaldi, E., Pecnik, R. & Colonna, P. 2012 Accurate and efficient look-up table approach for dense gas flow simulations. *Proceedings of the 6th European Congress on Computational Methods in Applied Sciences and Engineering, Vienna-Austria* pp. 8690–8704.

Sarkar, S. 1995 The stabilizing effect of compressibility in turbulent shear flow. *Journal of Fluid Mechanics* **282**, 163–186.

Schmitt, T., Selle, L., Ruiz, A. & Cuenot, B. 2010 Large-eddy simulation of supercritical-pressure round jets. *The American Institute of Aeronautics and Astronautics journal* **48** (9), 2133–2144.

Sciacovelli, L., Cinnella, P. & Gloerfelt, X. 2017 Direct numerical simulations of supersonic turbulent channel flows of dense gases. *Journal of Fluid Mechanics* **821**, 153–199.

Sengers, L. J., Morrison, G. & Chang, R. 1983 Critical behavior in fluids and fluid mixtures. *Fluid Phase Equilibria* **14**, 19–44.

Shitsman, M. 1963 Impairment of the heat transmission at supercritical pressures (heat transfer process examined during forced motion of water at supercritical pressures). *High Temperature* **1**, 237–244.

Sinha, K. & Candler, G. V. 2003 Turbulent dissipation-rate equation for compressible flows. *AIAA journal* **41** (6), 1017–1021.

Soave, G. 1972 Equilibrium constants from a modified redlich-kwong equation of state. *Chemical Engineering Science* **27** (6), 1197–1203.

Span, R. & Wagner, W. 1996 A new equation of state for carbon dioxide covering the fluid region from the triple-point temperature to 1100 k at pressures up to 800 mpa. *Journal of physical and chemical reference data* **25** (6), 1509–1596.

Stocker, T. 2014 *Climate change 2013: the physical science basis: Working Group I contribution to the Fifth assessment report of the Intergovernmental Panel on Climate Change*. Cambridge University Press.

Trettel, A. & Larsson, J. 2016 Mean velocity scaling for compressible wall turbulence with heat transfer. *Physics of Fluids* **28** (2), 026102.

Vesovic, V., Wakeham, W., Olchowy, G., Sengers, J., Watson, J. & Millat, J. 1990 The transport properties of carbon dioxide. *Journal of Physical and Chemical Reference Data* **19** (3), 763–808.

Van der Waals, D. 1873 *Over de Continuiteit van den Gas-en Vloeistoftoestand*, , vol. 1. Sijthoff.

Wanner, G. & Hairer, E. 1991 Solving ordinary differential equations ii. *Stiff and Differential-Algebraic Problems* .

Wei, L. & Pollard, A. 2011 Direct numerical simulation of compressible turbulent channel flows using the discontinuous galerkin method. *Computers & Fluids* **47** (1), 85–100.

Wright, S. A., Conboy, T. M., Parma, E. J., Lewis, T. G. & Suo-Anttila, A. J. 2011 Summary of the sandia supercritical co2 development program. *Tech. Rep.*. Sandia National Laboratories (SNL-NM), Albuquerque, NM (United States).

Yamagata, K., Nishikawa, K., Hasegawa, S., Fujii, T. & Yoshida, S. 1972 Forced convective heat transfer to supercritical water flowing in tubes. *International Journal of Heat and Mass Transfer* **15** (12), 2575–2593.

Yoo, J. Y. 2013 The turbulent flows of supercritical fluids with heat transfer. *Annual Review of Fluid Mechanics* **45**, 495–525.

Zhao, N., Mentrelli, A., Ruggeri, T. & Sugiyama, M. 2011 Admissible shock waves and shock-induced phase transitions in a van der waals fluid. *Physics of fluids* **23** (8), 086101.

Ziegel, E. 1987 Numerical recipes: The art of scientific computing.

Zonta, F., Marchioli, C. & Soldati, A. 2012 Modulation of turbulence in forced convection by temperature-dependent viscosity. *Journal of Fluid Mechanics* **697**, 150–174.

Acknowledgments

I would firstly like to express my sincere gratitude and respect for Dr. Rene Pecnik, who was my daily supervisor. He gave me a lot of his valuable time and patiently supported me in developing my research skills. Also, he was available for a discussion almost anytime when it was necessary. I also learnt from him the qualities of achieving a high level of perfection in my work.

I am also deeply indebted to my promoter Prof. Bendiks Jan Boersma who also helped me in my research and always gave his valuable inputs in my journal publications. He was also very approachable and was always willing to have academic discussions to clarify any doubts that I had in my work.

I would also like to convey my deepest regards and heartfelt thanks towards the distinguished members of the thesis defence committee for accepting our invitation to oversee these proceedings.

I would like to leave a special word of thanks for my colleague and friend Dr. Hassan Nemati who helped me in improving my programming skills and collaborated with me in my publications and also to my friend Stephan Smit for helping me to translate the summary of my thesis to Dutch.

To my other PhD colleagues Ashish, Jurriaan, Enrico, Simone and Gustavo, I would like to say that I have been privileged to have been associated with this group of people who are not only brilliant and knowledgeable academic minds but also great friends. I have learnt a lot from this group of people in both the academic and the non-academic spheres and would hope that we remain good friends for a long time to come.

To all my friends in the department, I would also like to give a special word of thanks as my stay in Delft would not have been such a great experience had I not developed a good circle of friends outside of my work.

I would like to thank Shell and NWO for providing the funding that made this research possible and SURFsara for making available the requisite amount of computing time necessary for performing the simulations.

Lastly, I would like to express my gratitude and respect for my mother Sanchayita, father Uttam and brother Uddipta who have supported me every step of the way and have stood by me like a rock in times of difficulty.

List of publications

Journal papers

Sengupta U., Nemati, H., Boersma, B.J. & Pecnik, R. 2012. Fully compressible low-Mach number simulations of carbon dioxide at supercritical pressures and trans-critical temperatures. *Flow, Turbulence and Combustion*, **99**, pp. 909–931.

Conference papers

Sengupta U., Boersma B.J. & Pecnik R. 2017. Fully compressible simulations of supercritical carbon dioxide close to the vapour-liquid critical point. *Proceedings of the 16^{th} European Turbulence Conference*, Stockholm - Sweden.

About the author

Uttiya Sengupta was born on the 23rd of January, 1988 in Calcutta, India. After completing his school education from South Point High School in Calcutta, he appeared for the IITJEE examinations and gained an entry into IIT Kharagpur in 2007. Having secured a GPA of 8.46/10, he graduted with a Bachelor of Technology in Chemical engineering in 2011.

In 2011, he secured an All India Rank of 15 in the Graduate Aptitude Test in Engineering and started his Master studies in the prestigious Indian Institute of Science, Bangalore. After completing his Master degree in Chemical Engineering in 2013, he applied for a job as a researcher in Shell Bangalore. Having cleared the requisite aptitude tests and interviews, he was among the 20 of the more than 3000 applicants selected for pursuing a PhD in "Computational Sciences for Energy Research" in the Netherlands in projects jointly funded by Shell/FOM. This field of research required knowledge in fluid mechanics and thermodynamics along with a good understanding in programming.

In his PhD, he worked under the supervision of Dr. Rene Pecnik and Prof. Bendiks Jan Boersma at the Delft University of Technology. He developed a parallel code which can simulate the fully compressible Navier Stokes equations and performed Direct Numerical Simulations of supercritical carbon dioxide near the vapour-liquid critical point. He presented his work at international conferences, such as, Engineering Turbulence Modelling and Measurements and the European Turbulence Conference. He also published his work in reputed journals, such as, the Journal of Flow, Turbulence and Combustion.

He is currently employed as a Quantitative Risk Analyst at ABN AMRO in Amsterdam. He is applying the quantitative skills gained during his PhD in quantifying risks that impact the financial industry in the Netherlands with the help of statistical modelling techniques.